SIMULATION OF COHESIVE PARTICLE FLOWS IN GRANULAR AND GAS-SOLID SYSTEMS

By

Michael Wallace Weber

B.S., University of Missouri-Rolla, 1998

M.S., University of Colorado, 2000

A dissertation submitted to the

Faculty of the Graduate School of the

University of Colorado in partial fulfillment

of the requirement for the degree of

Doctor of Philosophy

Department of Chemical and Biological Engineering

2004

This dissertation entitled:
Simulation of Cohesive Particle Flows in Granular and Gas-Solid Systems
Written by Michael Weber
Has been approved for the Department of Chemical and Biological Engineering

_____

Christine M. Hrenya, Assistant Professor

_____

Steven M. George, Professor

Date_____

The final copy of this dissertation has been examined by the signatories, and we find that both the content and the form meet acceptable presentation standards of scholarly work in the above mentioned discipline.

Weber, Michael Wallace (Ph. D., Chemical Engineering)

Simulation of Cohesive Particle Flows in Granular and Gas-Solid Systems

Dissertation directed by Professor Christine M. Hrenya

Cohesive interparticle forces may affect granular and fluidized flow applications by influencing minimum fluidization velocities and segregation behavior, and can lead to complete loss of flowability. These forces include van der Waals, liquid-briding, electrostatic, and magnetic forces. Despite the prevalence of cohesive effects in particulate flows, the incorporation of cohesion into continuum models is limited. Most cohesion models are defined as a continuous function of the separation distance between interacting particles. The continuous nature of these models conflicts with the assumption of instantaeous, binary collision inherent in the kinetic theory used to develop continuum models. A model that incorporates cohesive forces as binary, instantaneous impulses is the square-well model. In this work, the square-well model was incorporated into discrete-particle simulations of granular flow and fluidized flow to test the ability of the model to capture the physics of cohesive flows.

For simple shear flows, an investigation of the input parameter space indicates the presence of two distinct flow regimes. For large cohesive forces, a large, single agglomerate is formed. For moderate cohesive forces, the sheared system is composed of evenly distributed 2-particle, dynamic agglomerates. The results for this regime indicate that cohesion attenuates the stress components at higher solids

fractions (in the collisional regime), as compared to the non-cohesive case. At lower solids fractions (kinetic regime), cohesive forces do not impact the observed stress.

Within a fluidized bed simulation, a method to map the parameters of the square-well model to equivalent parameters in the Hamaker model has been developed based on the minimum, relative normal velocity required to escape agglomeration in two-particle simulations. Mapping effectiveness was gauged by measuring the minimum fluidization velocity, mixing index, and average particle movement at varying levels of cohesion.

The cohesive fluidized bed simulation was used to study hysteresis behavior observed during defluidization-fluidization cycles of experimental fluidized beds. In both cohesion models, cohesive particle-particle are the primary cause for the pressure overshoot for the parameters considered. Simulations using the square-well cohesion model indicate that cohesive interactions between particles and the distributor plate (bottom wall) are a secondary mechanism whereas, simulations using the Hamaker model reveal that cohesive interactions between particles and the sidewalls are a secondary mechanism.

This thesis is dedicated to the memory of my father,

Michael L. Weber

Acknowledgments

I would first like to thank those responsible for funding this project. This was provided by the Department of Energy through the National Energy Technology Laboratory. Additional funding was provided through the Department of Education Graduate Assistantships in Areas of National Need Fellowship. Without these contributions, this project would not have been possible.

Collaborative support has been provided from several sources. David Hoffman at the Ames Laboratory at Iowa State provided a great deal of insight to the effects of the square-well cohesion model. Dhanunjay Boyalakuntla at Purdue University provided us with the Eulerian-Lagrangian model used to study fluidized beds. The developers of MFIX including Tom O'Brien and Sreekanth Pannala have also provided a great deal of support in using that simulation package.

The other members of the Hrenya research group have provided a great deal of help in resolving day-to-day problems. I would especially like to thank Steve Dahl and Brent Rice for their help in developing the granular flow simulation. I would also like to thank Casey Carney, Eric Beckel and Brian Hutchison for being my friends over past six years.

Perhaps the most direct support to my work has come from my advisor Christine Hrenya. I thoroughly appreciated her patient guidance throughout this project. Her work ethic provides a great example for all the students in our group. She was also been very understanding as I went through some of the hardest times in my life and for that I am very thankful.

Finally, my acknowledgments would be incomplete if I did not include my family. With the exception of my wife, none them even know exactly what it is I do, but I could never have done it without them. My aunts, uncles, cousins and two grandmothers have encouraged me since the first grade and always given me a reason to do my best. My sister constantly inspires me with the passion she shows for her work and her relationships. My wife has been a constant source of support, especially during the final months of this project. My mother is one of the most selfless, loving people I have ever known and she has an inner strength that I can only begin to understand. All of my accomplishments are enabled by the support of my family.

Chapter 1. Introduction 1

1.1 Solids Processing Applications. 1

1.2 Particle Cohesion. 4

1.3 Types of Particulate Flows. 6

1.3.1 Rapid Granular Flows with Cohesive Particles. 6

1.3.2 Fluid-Solid Flows with Cohesive Particles. 7

1.3.2.1 Geldart Classification System. 8

1.3.2.2 Agglomerate Fluidization of Cohesive Particles. 11

1.4 Experimental and Modeling Approaches. 11

1.5 Overview of Current Effort. 14

1.6 Dissertation Organization. 15

1.7 References 15

Chapter 2. Review of Granular Flow for Cohesive Systems. 18

2.1 Hard-Sphere versus Soft-Sphere Models. 18

2.2 Event-Driven versus Time-Stepped Algorithms. 19

2.3 Previous Models of Rapid Granular Flows of Cohesive Particles. 21

2.4 References 24

Chapter 3. Granular Flow Simulation Description. 26

3.1 Particle-Particle Interactions. 27

3.1.1 Inelastic Collisions. 28

3.1.2 Cohesive Interactions. 29

3.2 Initialization, Steady-State Criteria and Data Collection. 34

3.3 Simulation Inputs. 36

3.4 Simulation Outputs. 37

3.5 Time Advancement. 39

3.6 References 41

Chapter 4. Granular Flow Results. 42

4.1 Two-Particle System. 42

4.2 Many-Particle System. 46

4.2.1 Flow Regimes 46

4.2.2 Mild-Cohesion Regime. 48

4.3 Summary of Granular Flow Results. 60

4.4 References. 61

Chapter 5. Literature Review of Models for Fluidized Flow Systems. 62

5.1 Eulerian-Eulerian Models. 65

5.2 Eulerian-Lagrangian Models. 66

5.3 Gas-Solid Models That Incorporate Cohesion. 68

5.4 References. 70

Chapter 6. Fluidized Bed Simulation Description. 73

6.1 Gas-Phase Model. 74

6.1.1 Governing Equations. 74

6.1.2 Boundary/Initial Conditions. 76

6.2 Solid-Phase Simulation. 78

6.2.1 Particle Advancement. 78

6.2.2 Linear-Spring-and-Dashpot Model. 80

6.2.2.1 Normal Contacts. 81

6.2.2.2 Oblique Contacts. 82

6.2.2.3 Determination of Spring and Dashpot Parameters. 84

6.2.2.3.1 Determination of K_n and η_n via Collision Experiments. 84

6.2.2.3.2 Numerical Stability and Accuracy 85

6.2.2.3.3 Parameters Used in Previous and Current Efforts. . 86

6.2.3 Calculation of Fluid Force on Particles. 89

6.2.4 Cohesive Interactions. 89

6.2.4.1 Hamaker model for van der Waals Forces. 90

6.2.4.2 Square-well Model. 91

6.2.5 Initial Conditions. 92

6.3 Coupling of the Gas and Solid Phases. 93

6.3.1 Calculation of Void Fraction and Average Particle Velocity. 93

6.3.2 Balance of Forces between Fluid and Solid Phase. 96

6.4 Model Verification and Validation. 97

6.4.1 Verification Methods. 97

6.4.2 Model Validation. 98

6.4.2.1 Qualitative Validation. 98

6.4.2.2 Quantitative Validation. 102

6.5 References. 108

Chapter 7. Comparison of Square-Well Potential and Hamaker Model for van der Waals Forces. 111

7.1 Parameter Mapping between Hamaker Model and Square-Well Model. 110

7.1.1 Force Comparison. 111

7.1.2 Potential Energy Comparison. 112

7.1.3 Escape-Velocity Comparison for Head-On Collisions. 114

7.2 Assessment of Mapping Method via Many-Particle Simulations. 117

7.2.1 Qualitative Comparison: Defluidization. 118

7.2.2 Qualitative Comparison: Mixing. 120

7.2.3 Quantitative Comparison: Minimum Fluidization Velocity. 123

7.2.4 Quantitative Comparison: Average Particle Movement. 126

7.3 Effect of Length Scale. 128

7.4 Summary of Efforts to Develop Mapping Between Cohesion Models. 132

7.5 References. 133

Chapter 8. Hysteresis in Fluidized Beds of Geldart Type A Particles. 135

8.1 Relevant Efforts. 135

8.2 Defluidization-Fluidization Cycle via Square-Well Model. 140

8.3 Defluidization-Fluidization Cycle via Hamaker Model. 147

8.4 Square-Well and Hamaker Model: Effects of bed width on pressure overshoot.152

8.5 Summary of Results. 156

8.6 References 157

Chapter 9. Summary. 158

9.1 Cohesion Models. 158

9.1.1 Cohesive Granular Flows. 158

9.1.2 Cohesive Gas-Solid Flows 159

9.2 Limitations of Eulerian-Lagrangian Method 162

9.3 Recommendations for Future Work. 163

9.4 References 165

Bibliography 166

Nomenclature. 177

APPENDIX A Derivation of Effective Coefficient of Restitution. 188

APPENDIX B Equations of Motion for Two-Particle Linear Spring-and-Dashpot Interaction. 191

APPENDIX C Equations of Motion for Two-Particle Spring-and-Dashpot Interaction with Constant Cohesive Forces. 194

APPENDIX D Square Well Model: Derivation of Expression for Head-On Collision. 196

APPENDIX E Sensitivity Analysis of Fluidized Bed Simulation Parameters. 199

List of Tables

3.1 Dimensionless simulation inputs 36

6.1. Linear spring and dashpot parameters used in previous efforts 87

6.2 Soft-sphere parameters used in fluidized bed simulation..... 88

6.3 Non-cohesive critical velocities. 108

7.1 Normal escape velocities obtained using both the square-well and Hamaker van der Waals models 117

7.2 Parameter values used in two-particle investigation of oblique collisions ... 130

List of Figures

1.1 Fluidized Bed Schematic 3

1.2 The Geldart Classification System 9

1.3 Geldart Type C behavior 9

3.1 Granular flow simulation domain 26

3.2 The square-well potential 27

3.3 Square-well interaction sequence 30

4.1 Geometry of two-particle simulations 43

4.2 Calculated (equation 4.2) and simulated values of the effective coefficient of restitution as a function of the vertical particle offset (δ) in two-particle simulations for e=0.8 and (a) r_{outer}/r_{inner} = 1.1 and, (b) r_{outer}/r_{inner} =1.0001. . . . 45

4.3 Snapshots of particle configuration showing transition from mild cohesion to strong cohesion regime. A dimensionless well depth of 25 (top row) shows the transition between solids fractions (ϕ) of 0.3 and 0.4, while a well depth of 30 (bottom row) shows the transition between solids fractions of 0.2 and 0.3. Middle row illustrates abrupt nature of transition over very narrow ranges of solids fraction. 47

4.4 Average agglomerate duration ($\Delta\bar{t}_{agg}$) and average number of particles per agglomerate ($\bar{P}$) at varying cohesive well depths (D^*) with r_{outer}/r_{inner}=1.001 and e=0.9. 51

4.5 Average agglomerate duration ($\Delta\bar{t}_{agg}$) and average number of particle per agglomerate ($\bar{P}$) for varying ratio of the well width to inner radius (r_{outer} / r_{inner})with D^*=10 and e=0.9. 52

4.6 Normal stress (*xx*-component) for varying cohesive well depth (D^*) with r_{outer}/r_{inner}=1.001 and e=0.9. 53

4.7 Normal collisional stress (*xx*-component) coming from(a) approaching-cohesive interactions,(b) escaping-cohesive interactions,(c) inelastic collisions, and (d) capture-cohesive interactions for r_{outer}/r_{inner}=1.001 and e=0.9. 54

4.8 Sum of the portion of normal stress (*xx*-component) coming from inelastic collisions and capture cohesive interactions for $_{outer}/r_{inner}$=1.001 and e=0.9. .. 55

4.9 Normal stress (*xx*-component) with varying values of well width to inner radius ratio (r_{outer} / r_{inner}) for D^* =10 and e = 0.9. 56

4.10 Shear stress (-*xy*-component) at varying cohesive well depths (D*) for r_{outer}/r_{inner}=1.001 and e=0.9. 56

4.11 Shear stress (-*xy*-component) from (a) approaching-cohesive interactions, (b) escaping-cohesive interactions,(c) inelastic collisions, and(d) capture-cohesive interactions for r_{outer}/r_{inner}=1.001 and e=0.9. 57

4.12 Diagram showing dominant (a) collision type in shear flow (b) with possible agglomerated collision. 59

6.1 Fluidized bed simulation domain. 73

6.2 Computational simulation domain 77

6.3 Inlet boundary conditions 78

6.4 Linear spring-and-dashpot model 82

6.5 Forces implemented by cohesion models 91

6.6 Fluidized Bed simulation algorithm. 94

6.7 Snapshots from non-cohesive bubbling fluidized bed simulation (4000 particles, U_s=91.6 cm/s). 99

6.8 Hypothetical fluidization cycle. 100

6.9 Results of fluidized bed simulation showing hysteresis in fluidization curve……..……101

6.10 Methodology in calculating theoretical fluidized bed weight (W_{theo}). 102

6.11 Comparison of calculated pressure drop to weight of particle bed. 103

6.12 Points identified as minimum fluidization velocity in previous studies. 104

6.13 Typical defluidization curve (decreasing U_s) used to identify defluidization velocity. 105

6.14 Typical fluidization (increasing U_s) curve used to identify the pressure overshoot, theoretical minimum fluidization velocity and incipient minimum fluidization velocity 106

6.15 Theoretical minimum fluidization velocities at varying particle diameter. .. 107

7.1 Forces versus separation distance for Hamaker and square-well cohesion models. 112

7.2 Potential energy associated with the Hamaker and square-well cohesion models. … 114

7.3 Layout of two-particle simulations used to determine escape velocity. 116

7.4 Square Well model: Snapshots displaying plugging ($D=1x10^{-3}$ erg)..... 119

7.5 Hamaker model: Snapshots displaying plugging ($A=1.0x10^{-11}$ erg)..... 119

7.6 Hamaker model: Snapshots showing formation of static bed structure at high levels of cohesion ($A=1x10^{-10}$ erg)..... 120

7.7 Square-Well model: Mixing behavior in simulation ($D=5x10^{-4}$)..... 121

7.8 Hamaker model: Mixing behavior in simulation ($A=7.49x10^{-12}$)..... 121

7.9 Method used to divide particles into families for calculation of mixing index……...122

7.10 Evolution of mixing index in time for simulations using the square-well cohesion model..... 123

7.11 Evolution of mixing index in time for simulations using the Hamaker model……..123

7.12 Defluidization velocity as a function of cohesive forces for both the Hamaker and square-well models..... 124

7.13 Theoretical minimum fluidization velocity as a function of cohesive force for both cohesion models 126

7.14 Incipient fluidization velocity as a function of cohesive forces for both cohesion models..... 126

7.15 Average particle movement with both cohesion models compared to escape velocity..... 127

7.16 Layout of two-particle simulations used to determine effect of square-well width on escape velocity. 129

7.17 Square-Well Model: Effect of approach angle on the escape velocity. 130

7.18 Hamaker model: Effect of approach angle on the escape velocity. 130

7.19 Square-Well model: Effect of r_{outer}/r_{inner} on the average particle movement.131

7.20 Square-Well model: Effect of router/rinner on the defluidization velocity for two well widths. 132

7.21 Hamaker model: Effect of H_{cut} on the defluidization velocity. 132

8.1 Sketch of fluidization-defluidization cycle showing pressure overshoot..... 136

8.2 Sketch of bed expansion behavior during defluidization-fluidization cycle. 137

8.3 Effect of bed width on the hysteresis in the fluidization-defluidization cycle observed experimentally. 139

8.4 Square-well model: Normalized fluidization curve (a) without and (b) with cohesion ($D=5x10^{-4}$ erg). 141

8.5 Square-well model: Fluidization cycle with no cohesion (D=0) (a) typical friction (μ = 0.3) and (b) a high level friction (μ = 1.0). 141

8.6 Square-well model: Fluidization curves for cases of (a) no particle-particle cohesion, (b) no particle-sidewall cohesion and (c) no particle-distributor cohesion ($D=5x10^{-4}$ erg). 142

8.7 Possible mechanism for pressure overshot in simulation with no particle-distributor cohesive forces. 143

8.8 Square well model: Net forces imposed on the particle from the fluid and gravity for the case of (a) no particle-particle cohesion, (b) no particle-sidewall cohesion, and (c) no particle-distributor cohesion ($D=5x10^{-4}$ erg). 144

8.9 Square-well model: Net force imposed on the particles by fluid forces and gravity with no excluded cohesive interactions ($D=5x10^{-4}$ erg). 146

8.10 Square-well model: Net force imposed on the particles by cohesive interactions with the distributor and frictional interactions with the sidewalls ($D=5x10^{-4}$) 146

8.11 Sketch of normal stress behavior during fluidization cycle. 147

8.12 Hamaker model: Normalized fluidization curve (a) without and (b) with cohesion ($A = 7.49 \times 10^{-12}$ erg). 148

8.13 Hamaker model: Fluidization curve for cases of (a) no particle-particle cohesion, (b) no particle-sidewall cohesion and (c) no particle-distributor cohesion ($A=7.49x10^{-12}$ erg). 149

8.14 Hamaker model: Net forces imposed on the particle from the fluid and gravity for the case of (a) no particle-particle cohesion, (b) no particle-sidewall cohesion, and (c) no particle-distributor cohesion ($A=7.49x10^{-12}$ erg). 150

8.15 Hamaker model: (a) Net force imposed on the particles from frictional interactions with the sidewalls (b) sum of normal contact force and cohesive force from distributor plate ($A=7.49x10^{-12}$ erg). 151

8.16 Hamaker model: Net force imposed on the particles by fluid forces and gravity with no excluded cohesive interactions ($A=7.49x10^{-12}$ erg). 151

8.17 Square-well model: Pressure overshoot fluidized beds with widths of (a) 4cm and (b) 12cm ($D=5.0x10^{-4}$ erg). 152

8.18 Hamaker model: Pressure overshoot for fluidized beds with widths of (a) 4cm and (b) 12cm ($A=7.49x10^{-12}$ erg). 153

8.19 Net force applied to the particles from frictional sidewall interactions and cohesive interactions with the distributor plate when using the square-well model for fluidized beds with widths of (a) 4cm and(b) 12 cm. 153

8.20 Net force applied to the particles from frictional sidewall interactions when using the Hamaker model for fluidized beds with widths of (a) 4cm and (b) 12 cm. 154

8.21 Effect of increased cohesion levels on the normalized pressure overshoot…156

Chapter 1. Introduction

1.1 Solids Processing Applications

The need to process solid particulates is common to many industries. For instance, in the chemical industry, it is estimated that 60 percent of the products are in the form of solid particulates [1]. Aside from the chemical industry, solids handling operations are also used in the food preparation, pharmaceuticals, power and utilities, and metals industries [2]. Thousands of companies spend millions of dollars every year in an effort to move, mix and react solid materials [3].

Flows occurring in solids handling applications can be divided into two groups: granular flows and fluidized flows. *Granular flows* refer to situations in which the solid particles are massive enough such that the interstitial fluid does not significantly affect particle movement. In *fluid-solid flows*, the interstitial fluid does have a significant effect on the movement of the particles. In the following sections, some examples are presented of both types of solids flow applications.

An understanding of granular flows is important in the pharmaceutical industry. The ability to mix solids in a reproducible manner is essential to ensure that pills and capsules deliver the correct dosage of medication. Although the Food and Drug Administration requires elaborate clinical trials to ensure that experimental drugs are safe for the general public [4], these trials are futile if the drugs cannot be manufactured reproducibly. While an operation as simple as mixing two drug components together may seem like a trivial task, the tendency of particles to segregate can lead to products that are ineffective or unsafe. Such segregation can arise due to differences in particle size and/or density [5, 6]. In some cases,

interparticle cohesion has been found to either mitigate or enhance cohesion, depending on the nature of the cohesive forces [7].

The importance of granular flows is not limited to the pharmaceutical industry. Poor handling of solids can lead to wasted material and energy in the mining industry [8]. Non-uniform pouring of powder material can lead to defective die-pressed products [9]. In the food industry, special attention must be paid to particle segregation as it has been found that if spice particles are too large, then potato chips will have no taste [10]. These examples represent a few applications of granular flows, and some of the relevant problems in each area.

Fluid-solid flows present additional challenges as the influence of the fluid phase can lead to additional flow complexities. A key example of fluidization occurs in the oil industry. Crude oil is separated into its useful components through the distillation process. However, a portion of the crude oil is made up of long-chain hydrocarbons that are not very useful on their own. In order to convert this portion into a useful product, the long chains must be broken apart in a process called catalytic cracking [11]. This process requires that the unusable crude be brought into contact with solid catalyst powder. The first plant to utilize this process went into operation in 1936 and used simple *fixed* bed of catalyst. In 1942, a *fluidized* bed was first used in place of the fixed bed. A typical fluidized bed schematic is shown in Figure 1.1. In this system, the solid is in the form of particles that are free to move about in the reactor. Fluidized beds provide more efficient contacting between the solid and the fluid and are integral in enabling catalytic cracking to be a practical, industrial-scale process.

To illustrate the importance of this process during World War II, catalytic cracking made it possible to produce 100-octane fuel, giving British planes a 50% faster burst of speed over German planes using only 85-octane. This advantage led to a loss of only 915 British planes to 1733 German planes during the Battle of Britain [12]. Today, fluidized beds are an essential component of fluid catalytic cracking systems that have the capacity to process 12.7 millions barrels of oil a day [13], and allow gasoline producers to make more useful product from raw crude oil. In particular, an increase in product selectivity of 1% allows a reduction in oil imports by more than 22 million barrels of crude per year [12]. Despite the advantages of catalytic cracking, these systems still incur problems that waste time, money and resources. For example, the cohesive nature of most catalyst powders makes them unpredictable and difficult to fluidize leading to the loss of catalyst and improper catalyst circulation [11]. Similar problems are encountered in other fluidized flow systems.

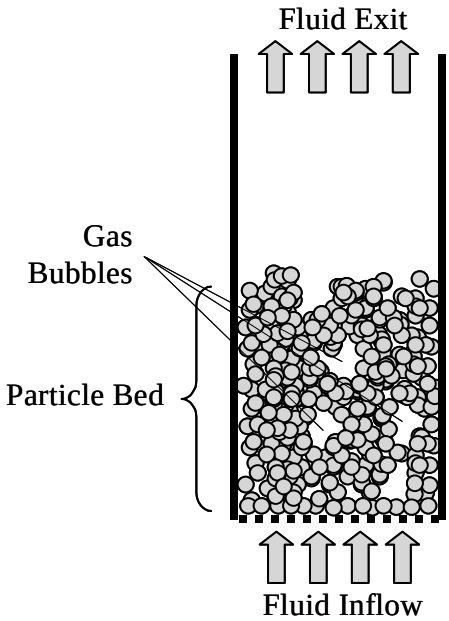

Fig. 1.1 *Fluidized Bed Schematic*

Fluidized beds have been used in the production of other products including polymers [14], nanotubes [15] and liquid hydrocarbons via the Fischer-Tropsch synthesis [12]. Fluidized beds are also used to remove unwanted materials from wastewater streams [14] and to remove pollutants from the atmosphere [16]. Other

fluidized systems of importance include pneumatic conveyers [2] and cyclone separators [17]. In all these systems, the complex nature of the gas-solid interaction can lead to serious operating problems.

It has been estimated that most solids handling systems operate at only 60% of their design capacity [18]. A key reason for the problems encountered in solids handling operations is that many of these systems are poorly understood. A greater understanding of these solids-handling systems will make the processes more efficient, kinder to the environment, and safer to those involved. For example, improved knowledge will allow mixers in pharmaceutical applications to be designed in a way that mitigates unwanted particle segregation. Also, new techniques can be developed to fluidize cohesive catalyst powders that normally resist flow.

The overall goal of this work is to gain a greater understanding of solids handling systems with a focus on the effects of short-range cohesion (e.g. van der Waals forces) between particles. In the following section, an overview of cohesive forces will be presented.

1.2 Particle Cohesion

Cohesive forces may arise from a variety of sources including liquid bridges, van der Waals forces, electrostatic forces and magnetic forces. In systems composed of solid particulates, two of the most prevalent inter-particle forces are the liquid-bridging force and the van der Waals force [19-24]. Liquid-bridging forces arise when the liquid film on a particle comes into contact with another surface. Both capillary (static) forces (surface tension, hydrostatic pressure and buoyancy) and

viscous (dynamic) forces may result. A variety of models to describe the capillary forces are available, a key facet of which is the method used to determine the shape of the liquid bridge. In early models, the contour of the liquid bridge has been approximated using shapes such as circular arcs and hyperbolas (see [22] for review). Models using this approximation for the shape of the liquid bridge work well at low particle separation distances, but tend to underestimate the attractive force at high particle separation distances [25]. More recently, the shape of the liquid bridge has been approximated via numerical solutions of the Laplace-Young equation, which equates the surface tension of the curved bridge to the pressure deficiency across the gas-liquid interface. (see [26] for a review). Despite the variation in treatments, each of these liquid-bridging models provides the magnitude of the particle-particle attractive force as a function of the separation distance (i.e., attractive force varies *continuously* with separation distance).

Van der Waals forces include dipole-dipole, dipole-non-polar and instantaneous dipole (dispersion) forces. London [27] quantified these forces by developing an expression for the attractive force between two molecules as a function of their separation distance. The resulting force depends on the polarizability of the molecule. Hamaker [28] integrated the molecule-molecule attractive force over entire solid bodies in order to obtain expressions for the attractive force between solid bodies of simple geometric shapes. A key assumption of this model is that all forces are two-body and additive. A more recent theory by Lifshitz [29] does not require such assumptions. Instead, by treating the solid bodies as continua, the attractive force is determined using bulk material properties only (dielectric constant and

refractive index). Similar to the liquid-bridging models noted above, all of these models treat van der Waals forces as a *continuous* function of the inter-particle distance.

1.3 Types of Particulate Flows

Experimental efforts to study the effects of cohesion on the overall bulk flow can be organized into those involving granular systems and fluidized systems. As stated previously, fluidized systems refer to situations in which the interstitial gas flow significantly affects the particle movement. Two examples of fluidized flow systems are fluidized beds and pneumatic conveyers. Granular systems, in which the interstitial fluid effects are negligible, can be further divided into rapid flows and slow flows. *Rapid* flows are characterized by instantaneous, binary contacts like those occurring in hoppers or mixing systems. *Slow* flows are characterized by enduring, frictional contacts like those seen in soil mechanics or silos. The focus of this work will be limited to rapid granular flow systems and fluidized systems, namely those that tend to be characterized by fairly short collisions between two particles. The following sections review some of the previous efforts to study cohesion in these systems.

1.3.1 Rapid Granular Flows with Cohesive Particles

A large number of experimental granular flow efforts involve mixers. These flows are primary slow flows, except at the surface of the particle bed. The efforts described herein have involved adding a controlled amount of liquid to the system in

order to increase the level of cohesion via liquid bridging. Tegzes *et al*. performed experiments with a drum roller and controlled liquid-bridging forces [30-32]. A drum roller is a cylinder, filled with particles, capable of rotating around its longitudinal axis at a controlled rate. As the cylinder rotates, a bed of particles inside the cylinder mixes and the angle formed by the surface of the particles as they avalanche back onto themselves is called the dynamic angle of repose. Using this apparatus, Tegzes *et al*. identified three different flow regimes depending on the liquid loading. Each of these regimes exhibited different avalanching behavior, yet the dynamic angle of repose increased as the liquid loading increased in each regime. Nase *et al*. characterized cohesive granular systems by measuring static and dynamic angles of repose as well as hopper discharge rates [33]. They characterized their results in terms of a the granular bond number which relates the cohesive force to the particle weight. They concluded that this simplified force ratio may be used to predict the ability of cohesive particles to flow. Li and Mcarthy [34] have shown that the addition of water to granular materials can lead to enhanced segretation through the action of liquid bridging forces. They were also able to characterize their results with the granular bond number.

1.3.2 Fluid-Solid Flows with Cohesive Particles

Many of the same techniques used to study rapid granular flows of cohesive particles are used to study fluidized flows of cohesive particles. The following sections review the relevant experimental efforts to study the flow of cohesive particles in fluidized systems.

1.3.2.1 Geldart Classification System

The Geldart classification system is used to identify the fluidization behavior of solid particles in a vertical gas-solid fluidized bed at ambient conditions. In this system, gas flows upward through a distribution plate at a velocity great enough to fluidize (but not carry over) the particles as shown in Figure 1.1. The Geldart classification system [35] groups particles that exhibit similar fluidization characteristics according to particle diameter (d_p) and density difference between the two phases ($\rho_s - \rho_g$) (ρ_s is the density of the particles and ρ_g is the density of the interstitial fluid. A rough sketch of this classification is illustrated in Figure 1.2. Type D particles form spouted fluidized beds. Type B particles exhibit bubbling at the point of incipient fluidization. Type A (aeratable) powders are known to exhibit both uniform fluidization without bubbles as well as bubbling fluidization (at higher gas velocities). Type C (cohesive) particles, which are relatively small particles, are known to be difficult to fluidize due to the increasing importance of cohesive forces. Particles of this type often form cracks, channels, and sometimes rise in the bed as a solid plug as illustrated in Figure 1.3.

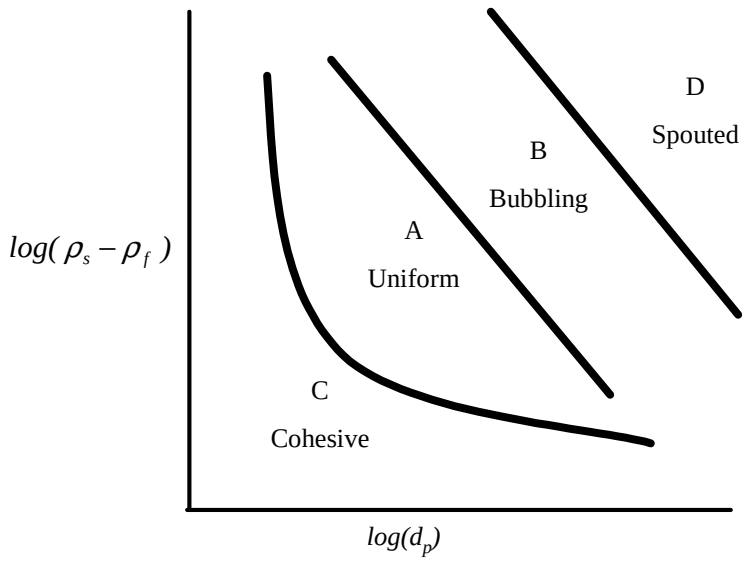

Fig. 1.2 *Geldart Classification System*

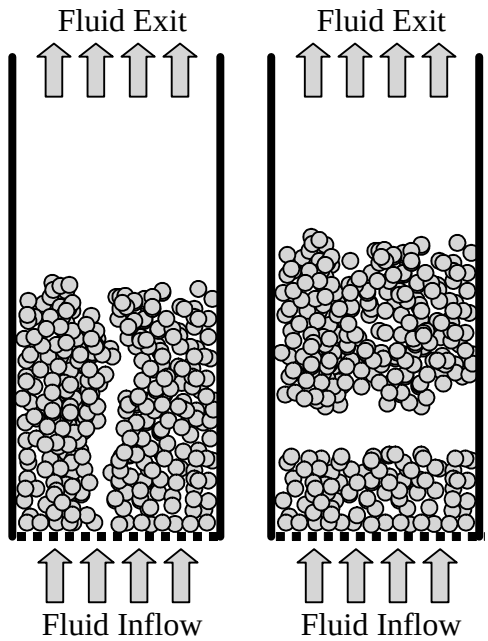

Fig. 1.3 *Geldart Type C behavior*

In addition to classifying particles based on their observed behavior, Geldart [35] derived empirical expressions to predict the boundaries between Type A and

Type B particles, as well as and between Type B and Type D particles. Molerus [36] later developed an expression to define the transition from Type A behavior to Type C behavior by comparing the maximum drag force to the cohesive force based on the Lifshitz [37] model for van der Waals forces. The results of Molerus' work suggest that this boundary occurs when the ratio of cohesive force to particle weight is approximately 1900. This Type A –Type C transition is especially important because it defines which particles can be easily fluidized and which particles cannot. While data for naturally (not induced using an interstitial fluid) cohesive particles agreed with the boundary derived by Molerus, they did not assess the accuracy of this boundary by controlling the level of cohesion in some way and designing systems that would be near the transition.

More recently, several fluidized bed studies have controlled the force ratio using the same method described in the previous section for granular systems. By adding a controlled amount of non-volatile liquid to the fluidized bed system, researchers have induced liquid bridging forces while holding the weight of the particles constant [38-41]. The magnitude of the liquid bridging force in the experiment can be estimated using existing liquid-bridging models, allowing researchers to effectively set the ratio of cohesive force to particle weight in their system. McLaughlin and Rhodes [38] focused on the force ratio at the point of the Type A-Type C transition. Their results showed that the critical ratio value is approximately unity, much smaller than the value (~1900) predicted by Molerus [36]. This discrepancy may be due to the different cohesion models used in the two studies.

McLaughlin and Rhodes used a liquid-bridging model while Molerus used a van der Waals model. This issue has yet to be resolved and will be revisited in Chapter 7.

Aside from the transition from flowable to non-flowable particles, some of the studies mentioned here also contained observations of more subtle effects of cohesion. For mild levels of cohesion (no plugging), several researchers observed an increase in the minimum fluidization velocity as the level of cohesion was increased [39-42]. The mechanisms behind this phenomenon are still not fully understood.

1.3.2.2 Agglomerate Fluidization of Cohesive Particles

Agglomerate fluidization is an effect of cohesion that is not accounted for in the traditional Geldart classification system. Several researchers [43-46] have observed that low-density Type C particles can be fluidized at gas velocities much higher than the expected minimum fluidization velocity for the individual particle diameters. These particles initially form channels, but as the gas velocity is raised, the channels break apart and the particles form stable agglomerates that fluidize uniformly. Vibrational [47-50] and acoustic [51-57] flow assistance are often used with these types of particles. The subject of agglomerate fluidization will be discussed in more detail in Chapter 9.

1.4. Experimental and Modeling Approaches

To further the understanding of cohesive effects in particulate systems, both experimental and modeling techniques offer complementary advantages… Experiments provide data for realistic systems, whereas models are often limited to idealized systems. In particular, certain assumptions may be necessary in the

development of mathematical models, such as perfectly spherical particles, perfectly smooth particles, or a monodisperse medium. Such physical assumptions limit the range over which the results are valid. Other simplifications are often necessary to make the models computationally tractable, such as simplified geometries and a limited number of particles (in the case of discrete-particle simulations).

Despite these limitations, mathematical models have some advantages over laboratory experiments. The use of simulations allows investigators to obtain values for parameters that may be difficult to measure experimentally. For example, although noninvasive measurements of the position and velocity of individual particles in a fluidized system exist [58], these methods are fairly restrictive in the types of systems they can be applied to (e.g., dilute flows). In addition, the effort and expense associated with these techniques are nontrivial. Alternatively, discrete-particle models of a fluidized bed allow for a straightforward calculation of the position and velocity of each particle as a function time.

Another advantage of mathematical models is that each parameter of the system can be controlled independently. In laboratory experiments, many of the finer aspects of the system cannot be varied independently. For example, particle cohesion has been controlled experimentally by adding a liquid to the system such as water, oil or surfactant to control the volume of the liquid bridges formed between particles [33, 38, 39, 59]. However, the addition of liquid can also change the density and viscosity of the fluidizing gas, as well as the density of the particles [60]. Such complications make it difficult to pinpoint the primary cause for a change in system behavior.

Models offer an alternative approach in this situation because the cohesive forces alone can be applied without impacting other system parameters.

This level of control is an even more powerful tool when models are used to selectively add and remove physical mechanisms in order to explore systems that cannot be achieved experimentally. For example, particle-particle cohesion can be turned on or off, or applied only to certain particles in the simulation, such as those in contact with a wall. The ability to simulate these physically unrealistic situations allows for the isolation of individual mechanisms. For example, when considering the effect of cohesion on behavior of a fluidized bed, the importance of particle-wall cohesion relative to particle-particle cohesion is not well understood(as will be discussed in Chapter 8). Using a fluidized-bed simulation, particle-wall cohesion (or particle-particle cohesion) can be removed in a straightforward manner. The results of such a simulation can then be compared to the results of a base simulation to determine the effect of the isolated mechanism.

In the current effort, a mathematical model is developed to gain insight into the behavior of cohesive-particle flows. Generally speaking, particle flows can be modeled using either a continuum or discrete-particle (molecular dynamics) approach. Continuum (Eulerian) models treat the particles as a continuous phase, while discrete-particle (Lagrangian) models determine the movement of each individual particle. Advantages and disadvantages exist in both approaches. The next section will discuss how the strengths of both approaches can be used together to further the fundamental understanding of solids handling applications.

1.5 Overview of Current Effort

Continuum models treat the particles as a continuous phase via a mass and momentum balance for that phase, along with appropriate constitutive equations. For rapid flows, a kinetic-theory analogy [61, 62] is typically used to develop constitutive relations needed for continuum models. Inherent in the kinetic-theory approach is the assumption that particle-particle interactions are both binary and instantaneous. As mentioned previously, cohesive forces are not inherently instantaneous, and thus the incorporation of cohesive forces into the kinetic theory framework is not straightforward. Unlike continuum models, discrete-particle simulations track particles in the system via the solution of a separate momentum balance for *each* particle. Most existing descriptions for particle cohesion can be applied to discrete-particle models while not conflicting with any assumptions inherent in the simulation.

Discrete-particle simulations provide a straightforward means of incorporating interparticle attraction because cohesive forces can be applied directly to each particle-particle interaction. However, discrete-particle simulations are limited by the computational requirements arising from the solution of a separate momentum balance for each particle. In contrast, continuum models based on the kinetic theory provide a less computationally demanding means of investigating particulate flows, but they are restricted by the assumptions implicit in their constitutive relations (e.g. instantaneous, binary contacts).

With these ideas in mind, a primary goal of this project is to investigate an alternative description of cohesive forces (i.e., short-range, attractive forces), namely the square-well potential. The square-well description treats cohesion as arising from

impulsive events, and thus represents a possible means of incorporating cohesive effects into continuum models. The performance of the square-well approximation for cohesive forces is investigated via discrete-particle simulations.

1.6 Thesis organization

This thesis is comprised of two main efforts. The first part deals with discrete-particle simulations of granular flow shear flow, while the second portion deals with discrete-particle simulations of a fluidized flow bed. Chapters 2-4 cover the effort to incorporate the square-well cohesion model into the granular flow simulation. The effectiveness of this model is assessed through an exploration of the parameter space. Chapters 5-7 contain a description of the effort to incorporate the square-well model into a fluidized flow simulation. A more elaborate Hamaker model for van der Waals forces is also applied to the fluidized flow simulation in order to provide a benchmark with which to compare the square-well model. In Chapter 8, the cohesive fluidized flow simulation is used to study the hysteresis effects observed in fluidized bed experiments. Specific particle-particle and particle-wall interactions are selectively excluded from the simulation in order to gain more insight in the pressure overshoot. In Chapter 9, a summary of the results and suggestions for future work are given.

1.7 References

1. J. Bridgwater, Particle Technology, *Chemical Engineering Science* 50 (24) (1995) 4081.
2. T. M. Knowlton, J. W. Carson, G. E. Klinzing, and W.-C. Yang, The importance of storage, transfer and collection, *Chemical Engineering Progress* 90 (April) (1994) 44.
3. J. W. Carson, Equipment, modeling and testing - Bulk solids handling, *Chemical Engineering* 109 (8) (2002) 98.
4. F. J. Muzzio, T. Shinbrot, and B. J. Glasser, Powder technology in the pharmaceutical industry: the need to catch up fast, *Powder Technology* 124 (1-2) (2002) 1.

5. J. Bridgwater, Mixing and segregation mechanisms in particle flow, in Granular Matter: An interdisciplinary approach, A Mehta, Editor, 1994, Springer-Verlag: New York. 160.
6. J. M. Ottino and D. V. Khakhar, Mixing and segregation of granular materials, *Annual Review of Fluid Mechanics* 32 (2000) 55.
7. J. J. McCarthy, Micro-modeling of cohesive mixing process, *Powder Technology* 138 (2003) 63.
8. A. W. Roberts, Particle technology -- Reflections and horizons: An engineering perspective, *Transactions of the Institution of Chemical Engineers* 76 (October) (1998) 775.
9. C.-Y. Wu, L. Dihoru, and A. C. F. Cocks, The flow of powder into simple and stepped dies, *Powder Technology* 134 (24) (2003) 24.
10. P. Mort,Tutorial on processing, handling and characterization of powder agglomerates,Indianapolis,2002.
11. R. Sadeghbeigi, Fluid catalytic cracking handbook, Gulf Publishing, Houston, Texas, 2000.
12. R. J. Farruato and C. H. Bartholomew, Fundamentals of industrial catalytic processes, Blackie Academic and Professional, London, 1997.
13. M. L. Rader, Worldwide refining, *Oil and Gas Journal* (December 23) (1996) 52.
14. L.-S. Fan, Gas-liquid-solid fluidization engineering, Butterworths, Boston, 1989.
15. A. Margolin, R. Rosentsveig, A. Albu-Yaron, R. Popovitz-Biro, and R. Tenne, Study of growth mechanism of WS2 nanotubes produced by a fluidized bed reactor, *Journal of Materials Chemistry* 14 (4) (2004) 617.
16. S. Matsuda, H. Hatano, and A. Tsutsumi, Ultrafine particle fluidization and its application to photocatalytic NOx treatment, *Chemical engineering Journal* 82 (2001) 183.
17. A. K. Gupta, D. G. Lilley, and N. Syred, Swirl Flows, Abacus Press, Tunbridge Wells, 1984.
18. B. J. Ennis, J. Green, and R. Davies, The legacy of neglect in the U.S., *Chemical Engineering Progress* April (1994) 32.
19. J. Israelachvili, Intermolecular and Surface Forces, Academic Press London, London, 1991.
20. J. P. K. Seville, Processing of Particulate Solids, Blackie Academic and Professional, London, 1997.
21. J. Visser, On Hamaker constants: A comparison between Hamaker constants and Lifshitz-van der Waals constants, *Advances in Colloid Interface Science* 3 (1972) 331.
22. V. P. Mehrotra and V. S. Sastry, Pendular bond strength between unequal-sized spherical particles, *Powder Technology* 25 (1980) 203.
23. J. Visser, An invited review: van der waals and other cohesive forces affecting powder fluidization, *Powder Technology* 58 (1989) 1-10.
24. J. P. K. Seville, C. D. Willet, and P. C. Knight, Interparticle forces in fluidisation: a review, *Powder Technology* 113 (2000) 261-268.
25. D. N. Mazzone, G. I. Tardos, and R. Pfeffer, The effect of gravity on the shape and strength of a liquid bridge between two spheres, *Journal of Colloid and Interface Science* 113 (2) (1986) 544.
26. G. Lian, C. Thornton, and M. J. Adams, A theoretical study of the liquid bridge forces between two rigid spherical bodies, *Journal of Colloid and Interface Science* 161 (1993) 131.
27. F. London, *Z. Phys.* 63 (1930) 245.
28. H. C. Hamaker, The London-Van der Waals attraction between spherical particles, *Physica* 4 (10) (1937) 1058-1072.
29. E. M. Lifshitz, The theory of molecular attractive forces between solids, *Journal of Experimental and Theoretical Physics* 2 (1) (1956) 73.
30. P. Tegzes, R. Albert, M. Paskan, A.-L. Barabasi, T. Vicsek, and P. Schiffer, Liquid-induced transitions in granular media, *Physical Review E* 50 (5) (1999) 5823-5826.
31. P. Tegzes, T. Vicsek, and P. Schiffer, Development of correlations in the dynamics of wet granular avalanches, *Physical Review E* 67 (5) (2003) 051303.
32. P. Tegzes, T. Vicsek, and P. Schiffer, Avalanche dynamics in wet granular materials, *Physical Review Letters* 89 (9) (2002) 094301.
33. S. T. Nase, W. L. Vargas, A. A. Abatan, and J. J. McCarhy, Discrete characterization tools for cohesive granular material, *Powder Technology* 116 (2001) 214-223.
34. H. Li, McCarthy, J. J., Controlling Cohesive Particle Mixing and Segregation, *Physical Review Letters* 90 (18) (2003) 184301.

35. D. Geldart, Types of Gas Fluidization, *Powder Technology* 7 (1973) 285-292.
36. O. Molerus, Interpretation of Geldart's type A, B, C and D powders by taking into account interparticle cohesion forces, *Powder Technology* 33 (1982) 81.
37. H. Krupp, *Advances in Colloid Interface Science* 1 (2) (1967)
38. L. J. McLaughlin and M. J. Rhodes, Prediction of fluidized bed behaviour in the presence of liquid bridges, *Powder Technology* 114 (2001) 213.
39. P. C. Wright and J. A. Raper, Role of liquid bridge forces in cohesive fluidization, *Transactions of the Institution of Chemical Engineers* 76 (1998) 753.
40. M. L. Passos and A. S. Mujumdar, Effect of cohesive forces on fluidized and spouted beds of wet particles, *Powder Technology* 110 (2000) 222.
41. J. P. K. Seville and R. Clift, The effect of thin liquid layers on fluidization characteristics, *Powder Technology* 37 (1984) 117.
42. P. C. Wright and J. A. Raper, Examination of dispersed liquid-phase three-phase fluidized beds: Part 1 Non-porous, uniform particle systems, *Powder Technology* 97 (1998) 208.
43. T. Zhou and L. Hongzhong, Estimation of agglomerate size for cohesive particles during fluidization, *Powder Technology* 101 (1999) 57-62.
44. Y. Iwadate and M. Horio, Prediction of agglomerate sizes in bubbling fluidized beds of group C powders, *Powder Technology* 100 (1998) 223.
45. J. Chaouki, C. Chavarie, D. Klvana, and G. Pajonk, Effect of interparticle forces on the hydrodynamic behavior of fluidized aerogels, *Powder Technology* 43 (1985) 117.
46. C. Lauga, J. Chaouki, D. Klvana, and C. Chavarie, Improvement of fluidisability of Ni/SiO2 aerogels by reducing interparticle forces, *Powder Technology* 65 (1991) 461.
47. J. R. Wank, S. M. George, and A. W. Weimer, Vibro-fluidization of fine boron nitride powder at low pressure, *Powder Technology* 121 (2001) 195.
48. J. M. Valverde, A. Castellanos, and M. A. S. Quintanilla, Effect of vibration on the stability of a gas-fluidized bed of fine powder, *Physical Review E* 64 (2001) 021302.
49. K. Noda, Y. Mawatari, and S. Uchida, Flow patterns of fine particles in a vibrated bed under atmospheric or reduced pressure, *Powder Technology* 99 (1998) 11.
50. E. Marring, A. C. Hoffman, and L. P. B. M. Janssen, The Effect of Vibration on the Fluidization Behaviour of Some Cohesive Powders, *Powder Technology* 79 (1994) 1-10.
51. R. Chirone, L. Massimilla, and S. Russo, Bubble-free fluidization of a cohesive powder in an acoustic field, *Chemical Engineering Science* 48 (1) (1993) 41.
52. R. Chirone and L. Massimilla, Sound-assisted aeration of beds of cohesive solids, *Chemical Engineering Science* 49 (8) (1994) 1185.
53. C. A. Herrera and E. K. Levy, Bubbling characteristics of sound-assisted fluidized beds, *Powder Technology* 119 (2001) 229.
54. C. A. Herrera, E. K. Levy, and J. Ochs, Characteristics of acoustic standing waves in fluidized beds, *AIChE Journal* 48 (2) (2002) 503.
55. E. K. Levy, I. Shnitzer, T. Masaki, and J. Salmento, Effect of an acoustic field on bubbling in a gas fluidized bed, *Powder Technology* 90 (1997) 53.
56. M. G. Rasul, V. Rudolph, and M. Carsky, Segregation potential in binary gas fluidized bed, *Powder Technology* 103 (1999) 175.
57. P. Russo, R. Chirone, L. Massimilla, and S. Russo, The influence of the frequency of acoustic waves on sound-assisted fluidization of beds of fine particles, *Powder Technology* 82 (1995) 219-230.
58. J. Chaouki, F. Larachi, and M. P. Dudukovic, Noninvasive Tomographic and Velocimetric Monitoring of Multiphase Flows, *Industrial and Chemistry Research* 36 (11) (1997) 4476.
59. A. J. Forsyth, S. Hutton, and M. J. Rhodes, Effect of cohesive interparticle force on the flow characteristics of granular material, *Powder Technology* 126 (2002) 150.
60. S. C. Tsinontides and R. Jackson, The mechanics of gas fluidized beds with an interval of stable fluidization, *Journal of Fluid Mechanics* 255 (1993) 237.
61. I. Goldhirsch, Rapid granular flows, *Annual Review of Fluid Mechanics* 35 (2003) 267.
62. C. Campbell, Rapid Granular Flows, *Annual Review of Fluid Mechanics* 22 (1990) 57.

Chapter 2. Review of Granular Flow Models for Cohesive Systems

As stated in the previous chapter, granular flows can be modeled using either a continuum (Eulerian) or a discrete-particle (Lagrangian) approach. As the focus of this project is on discrete-particle simulations, the background information given below is targeted at this type of model. Following that discussion, a review of previous Eulerian and Lagrangian models for cohesive-particle systems is given. The roots of discrete-particle simulations can be found in molecular dynamics simulations. Cundall and Strack extended the molecular dynamics approach to flows of macroscopic, solid particles by incorporating inelastic particle interactions [1, 2]. The application of molecular dynamics to macroscopic particles has been further reviewed by Walton [3]. The first discrete-particle models developed by Cundall and Strack were applied to slow flows (flows with enduring contacts), but later they were applied to rapid granular flows (collision-dominated flows) by Campbell [4]. Discrete-particle models have subsequently been applied to studies of applications such as mixing [5-10], packing [11], and hopper discharge [12-14]. Discrete-particle models have also found great utility as a testbed to help develop constitutive relations based on kinetic theory [15-18]. Before proceeding into a review of cohesion in discrete-particle models, some important distinctions between various discrete-particle models are covered below.

2.1 Hard-Sphere versus Soft-Sphere Approach

A hard-sphere approach [19] to discrete-particle simulations differs from a soft-sphere approach in the manner in which particle-particle contacts are resolved.

For hard-sphere systems, these contacts are instantaneous and characterized by impulsive transfers of momentum. Furthermore, collisions occur only between two particles at a time. The magnitude of the normal component of the post-collisional relative velocity is determined via the coefficient of restitution (i.e., a measure of inelasticity), whereas the magnitude of the tangential component of the post-collisional velocity is based on parameters characterizing the frictional interaction (e.g., friction coefficient). Soft-sphere simulations [1, 20] treat particle-particle interactions as enduring contacts that generate forces which change over the duration of the contact. Furthermore, multi-particle contacts are possible. For soft-sphere systems, a force law is used to determine the magnitude of the force experienced by each particle based on the level of particle deformation (i.e., overlap). The critical difference between these two contact algorithms lies in the instantaneous, binary nature of collisions in the hard-sphere approach versus the enduring, multi-particle contacts utilized in the soft-sphere approach. These differences make the hard-sphere model more computationally efficient, though less robust than its soft-sphere counterpart. Soft-sphere simulations can be used to simulate both rapid and slow flow, whereas hard-sphere simulations are only applicable to rapid granular flows.

2.2 Event-Driven versus Time-Stepped Algorithms

Another key aspect of discrete-particle simulations is the type of algorithm used to advance the particles in time. Event-driven (predictive) algorithms [19] operate via a determination of the trajectories of every particle and a compilation of

an upcoming-collisions list. In these simulations, every particle is moved along its trajectory for the time needed to reach the next collision. Once that collision is resolved, the time to the next collision is determined, and the process is repeated. In this way, the simulation will proceed at varying time steps from one collision to the next. Because no particle overlap exists in such a simulation, event-driven algorithms are applied exclusively to hard-sphere systems.

For time-stepped algorithms [1, 20], all particles are advanced over a set amount of time. After this particle advancement, a check is performed to determine if any particle overlaps exist. Particle overlaps are indicative a collision. For all identified collisions, a contact model (e.g., soft sphere) is applied and the simulation is then advanced again in time. The time step is set small enough so that numerical inaccuracies are minimized. Because time-stepped models involve a slight particle overlap, this algorithm is always applied in conjunction with soft-sphere systems. Nonetheless, for some hard-sphere systems, a time-stepped algorithm has been used for purposes of improved computational efficiency [16].

The computational time necessary to simulate a given period of real time depends on the time step employed in the simulation. For event-driven algorithms, the time step is determined by the time to the next collision, and this value changes for each subsequent collision. In general, dilute systems will result in larger time steps, while dense systems will have smaller time steps. For time-stepped algorithms, the user specifies the time step. Smaller time steps will result in more accurate results; however, smaller time steps also result in longer simulation times. While most time-stepped algorithms use a constant time step, some efforts use variable time steps (for

example, via adjustment of the time step based on parameters such as average collision overlap) to ensure that an efficient time step is used throughout the entire simulation [16]. In either case, the choice of time step for time-stepped algorithms is always a tradeoff between accuracy and computational time.

2.3 Previous Models of Rapid Granular Flows of Cohesive Particles

The implementation of cohesion into continuum models of granular flow has been very limited due to the assumptions inherent in such models. Namely, continuum models for particulate flows are typically based on a kinetic-theory analogy, which requires that particle interactions are both binary and instantaneous. As described earlier, however, cohesive forces (e.g., van der Waals forces) vary continuously with separation distance. Kim and Arastoopour [21] developed a kinetic-theory model for granular flows that incorporates cohesion via a *contact bonding energy*. The contact bonding energy, which is a function of the surface properties of the material, is only activated at particle-particle contact. The resulting cohesive force is thus treated as instantaneous in nature. Moreover, agglomeration occurs when particles do not have a large enough kinetic energy (based on the relative particle velocity) to overcome the contact bonding energy. After agglomeration, the two particles are treated as a single spherical particle with the same total volume, thereby resulting in a decrease in the total number of particles in the system. This continuum model does not allow for particles (or agglomerates) of different sizes to co-exist, nor does it allow for de-agglomerations. The resulting model was used to

predict particle growth, shear stress and normal stress, which were found to agree qualitatively with expected behaviors.

The nature of discrete-particle models makes them more amenable to the incorporation of cohesive effects. In particular, cohesive forces are not restricted to being treated as instantaneous events, and thus many such contributions have been documented in the literature.

McCarthy and Ottino [6] developed a soft-sphere simulation that incorporates liquid-bridging forces. The liquid-bridge description formulated by Lian *et al*. [22], which involves a numerical solution of the Laplace-Young equation, was utilized. These simulations were used to predict the results from static and dynamic angle-of-repose experiments, and the comparisons showed good agreement.

Baxter *et al*. [14] utilized a discrete-particle simulation that incorporates cohesive forces. Their interparticle force model is similar to a Lennard-Jones model, which varies continuously with separation distance and contains both attractive and repulsive components. A unique component of their model, however, is that it contains an additional, attractive force at small amounts of particle overlap. Results of the simulation provide insight into the most efficient procedures to use in the discharge of hoppers.

Mei *et al*. [23] incorporated the Johnson-Kendall-Roberts (JKR) force-displacement model [24] into a simple shear flow simulation. The JKR model incorporates attractive surface forces into a model for the deformation of contacting, elastic solids. This study revealed that concentration non-uniformity in shear flows changes significantly once the shear rate drops below a critical value.

Muguruma *et al.* [25] developed a model of a rotating tumbler with liquid bridging forces between the particles and compared the results with those of experimental tumblers. Velocity profiles in the simulated tumbler agreed quantitatively with velocity profiles observed on high-speed video analysis in the experimental tumbler. The variation in the velocity with the volume of liquid added also agreed well between experiment and simulation.

Matuttis and Schinner [26] performed static angle-of-repose simulations using a discrete-particle approach with a cohesive force that is assumed proportional to the contact area. They found that no systematic differences exist between the results of their two-dimensional simulation and three-dimensional experiments.

Yang and Hsiau incorporated liquid-bridging forces into a discrete-particle model of a vibrated bed [27]. Their results showed that the dissipation of energy increases monotonically with liquid-bridge volume.

In each of the discrete-particle simulations of cohesive flow presented above, the cohesive force models utilized vary *continuously* with inter-particle distance (i.e. the forces are not impulsive). As described in Chapter 1, the continuous nature of these models makes them difficult to incorporate into continuum models derived from kinetic theory. A square-well description of cohesion, however, overcomes these obstacles by offering a simplified picture of the cohesive interaction (i.e., one which is instantaneous and binary in nature). Hence, an assessment of its ability to predict the flow behavior of cohesive particles is warranted.

2.4 References

1. P. A. Cundall, A computer model for rock-mass behavior using interactive graphics for input and output of geometrical data, *US Army Corps of Engineers (Missouri River Div) Tech. Rep. MRD-2074* (1974)
2. P. A. Cundall and O. D. Strack, A discrete numerical model for granular assemblies, *Geotechnique* 29 (1) (1979) 47-65.
3. O. R. Walton, Application of molecular dynamics to macroscopic particles, *International Journal of Engineering Science* 22 (8-10) (1984) 1097-1107.
4. C. S. Campbell, "Shear flows of granular materials", PhD dissertation, Calfornia Institute of Technology, 1982.
5. J. J. McCarthy and J. M. Ottino, A computational study of granular mixing: the effect of particle cohesion, *AIChE meeting proceedings* (1988)
6. J. J. McCarthy and J. M. Ottino, Particle dynamics: a hybrid technique applied to granular mixing, *Powder Technology* 97 (1998) 91.
7. J. J. McCarthy, D. V. Khakhar, and J. M. Ottino, Computational studies of granular mixing, *Powder Technology* 109 (2000) 72.
8. J. J. McCarthy, Micro-modeling of cohesive mixing processes, *Powder Technology* 138 (2003) 63.
9. J. M. Ottino and D. V. Khakhar, Mixing and segregation of granular materials, *Annual Review of Fluid Mechanics* 32 (2000) 55.
10. T. Shinbrot, D. Khakhar, J. J. McCarthy, and J. Ottino, A simple model for granular convection, *Physical Review Letters* 79 (5) (1997) 829.
11. K. Z. Y. Yen and T. K. Chaki, A dynamic simulation of particle rearrangement in powder packings with realistic interactions, *Journal of Applied Physics* 71 (7) (1992) 3164-3173.
12. P. A. Langston, U. Tuzun, and D. M. Heyes, Discrete element simulation of granular flow in 2D and 3D hoppers: dependence of discharge rate and wall stress on particle interactions, *Chemical Engineering Science* 50 (6) (1995) 967.
13. P. W. Cleary and M. L. Sawley, DEM simulation of industrial granular flows: 3D case studies and the effect of particle shape on hopper discharge, *Applied Mathematical Modeling* 26 (2002) 89.
14. J. Baxter, H. Abou-Chakra, U. Tuzun, and B. Lamptey, A DEM simulation and experimental strategy for solving fine powder flow problems, *Chemical Engineering Research and Design* 78 (2000) 1019.
15. C. S. Campbell and C. E. Brennen, Computer simulation of granular shear-flows, *Journal of Fluid Mechanics* 151 (1985) 167.
16. M. A. Hopkins and M. Y. Louge, Inelastic microstructure in rapid granular flows of smooth disks, *Phys. Fluids A* 3 (1) (1991) 47-57.
17. O. R. Walton and R. L. Braun, Viscosity, granular-temperature, and stress calculations for shearing assemblies of inelastic, frictional disks, *Journal of Rheology* 30 (5) (1986) 949-980.
18. R. Clelland and C. M. Hrenya, Simulation of a binary-sized mixture of inelastic grains in rapid shear flow, *Physical Review E* 65 (2002)
19. M. P. Allen and D. J. Tildesley, Computer Simulation of Liquids, Oxford University Press, Oxford, 1987.
20. O. R. Walton, Particle-dynamics calculations of shear flow, in Mechanics of Granular Materials: New Models and Constitutive Relations, J T Jenkins and M Satake, Editors, 1983, Elsevier Science Publications B.V.: Amsterdam.
21. H. Kim and H. Arastoopour, Extension of kinetic theory to cohesive particle flow, *Powder Technology* 122 (2002) 83-94.
22. G. Lian, C. Thornton, and M. J. Adams, A theoretical study of the liquid bridge forces between two rigid spherical bodies, *Journal of Colloid and Interface Science* 161 (1993) 131.
23. R. Mei, H. Shang, O. Walton, and J. Klausner, Concentration non-uniformity in simple shear flow of cohesive powders, *Powder Technology* 112 (2000) 102.
24. K. L. Johnson, K. Kendall, and A. D. Roberts, Surface Energy and the contact of elastic solids, *Proceedings of the Royal Society of London A* 324 (1971) 301.

25. Y. Muguruma, T. Tanaka, and Y. Tsuji, Numerical simulation of particulate flow with liquid bridge between particles (simulation of centrifugal tumbling granulator), *Powder Technology* 109 (2000) 49.
26. H. G. Matuttis and A. Schinner, Particle simulation of cohesive granular material, *International Journal of Modern Physics* 12 (7) (2001) 1011.
27. S. C. Yang and S. S. Hsiau, The simulation of powders with liquid bridges in a 2D vibrated bed, *Chemical Engineering Science* 56 (2001) 6837.

Chapter 3. Granular Flow Simulation Description

Rapid, granular shear flow is simulated using identical, two-dimensional frictionless, circular discs in a *LxL* periodic simulation domain. In this simulation, Lees-Edwards [1] boundary conditions are used to achieve a simple shear flow in the *x*-direction, as illustrated in Figure 3.1. Since no external forces (e.g., gravity) are applied to the particles, all particles move with linear trajectories between impulsive interactions with other particles.

Key aspects of this simulation include the initialization procedure, the criterion used to identify a steady state, as well as the inputs and outputs of the system. Also important are the methods used to resolve particle-particle interactions and the procedure used to advance the particles in time between interactions. Each of these issues is discussed in the sections that follow.

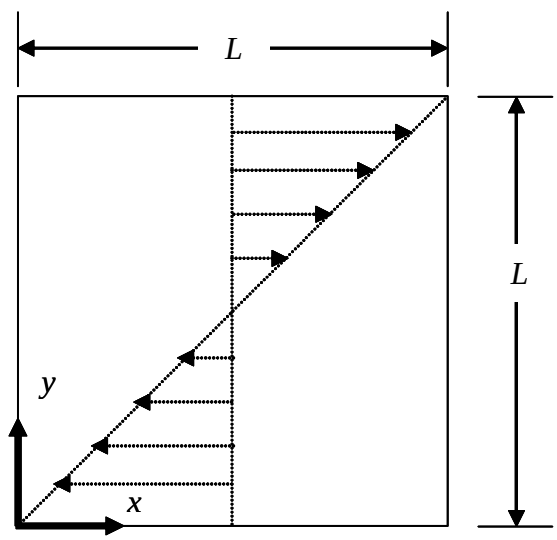

Fig. 3.1 *Granular flow simulation domain*

3.1 Particle-Particle Interactions

Particles in this simulation are hard-sphere (instantaneous contacts) in nature and may interact in two different ways: inelastic collisions and cohesive interactions. Inelastic collisions occur when the particles are in physical contact (i.e., when the distance between the particle centers is the sum of two particle radii). As illustrated in Figure 3.2, cohesive interactions are modeled using a square-well potential. Two parameters are needed to define the square well: the well width, r_{outer}, and the well depth, D. Cohesive interactions result from the impulsive forces which arise when the center-to-center distance of the two particles is equal to twice the width of the square well ($2r_{outer}$), which is always larger than twice the particle radius ($2r_{outer}>2r_{inner}$). Only r_{inner} is a *physical* particle radius. The magnitude of the cohesive impulse is controlled by the depth of the square-well potential.

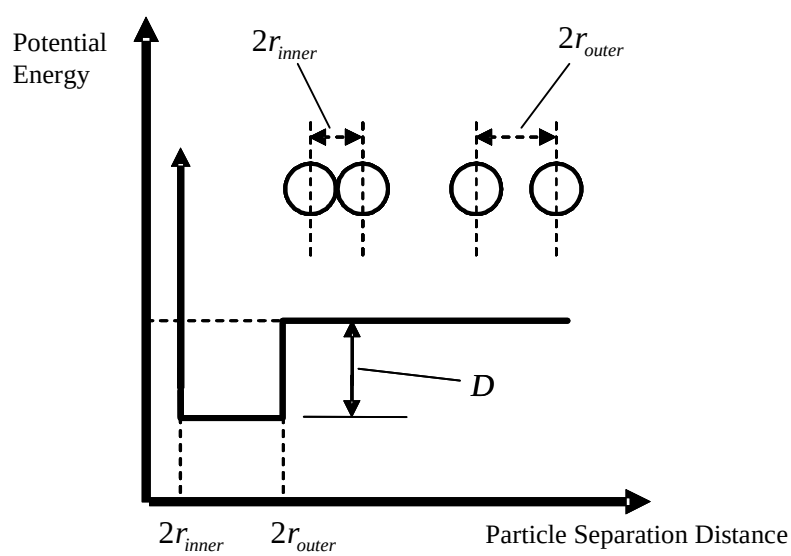

Fig. 3.2 *The square-well potential*

For both inelastic collisions and cohesive interactions, an instantaneous transfer of momentum takes place between the particles that results in the following change in momentum for particles *i* and *j*:

$$m\vec{v}_{i,post} = m\vec{v}_{i,pre} - J_* \vec{k}_{ij,*} \tag{3.1}$$

$$m\vec{v}_{j,post} = m\vec{v}_{j.pre} + J_* \vec{k}_{ij,*} \tag{3.2}$$

where m is the mass of an individual particle, $\vec{v}_{i,pre}$ and $\vec{v}_{i,post}$ are the pre- and post-interaction velocities, respectively, of the ith particle, $\vec{k}_{ij,*}$ is the unit vector pointing from the center of the ith particle to the center of the jth particle, and J_* is the magnitude of the impulse of momentum transferred during the particle-particle interaction (either inelastic collision or cohesive interaction).

3.1.1 Inelastic Collisions

For all inelastic collisions, the net momentum is conserved and a portion of the granular energy (kinetic energy associated with the translational velocity relative to the mean flow velocity) is lost. The fraction of granular energy lost is determined by the coefficient of restitution (e) which is a measure of the inelasticity that varies between zero and unity (where e = 1 represents a perfectly elastic collision):

$$\vec{k}_{ij,2} \cdot \vec{v}_{ij,c} = -e\left(\vec{k}_{ij,2} \cdot \vec{v}_{ij,b}\right) \tag{3.3}$$

where

$$\vec{v}_{ij} = \vec{v}_i - \vec{v}_j \tag{3.4}$$

and $\vec{k}_{ij,2}$ is the unit vector pointing from the center of the ith particle to the center of the jth particle at the point of physical contact (at separation distance of $2r_{inner}$), $\vec{v}_{ij,b}$ is the relative velocity between the two particles *before collision*, and $\vec{v}_{ij,c}$ is the relative velocity *after collision*. The relative velocity is defined in terms of the velocities of the ith particle, $\vec{v}_i$, and the jth particle, $\vec{v}_j$, as shown in equation 3.4. Performing a momentum balance in conjunction with the definition of the coefficient of restitution, along with the simplification that the velocity only changes in the normal direction (frictionless particles), leads to the following equation for the impulse during an inelastic collision:

$$J_{in} = \frac{m}{2}(1+e)\left(\vec{k}_{ij,2} \cdot \vec{v}_{ij,b}\right) \tag{3.5}$$

Substitution of this expression into equations 3.1 and 3.2 yields the post-collisional velocity of both particles in terms of e and the pre-collisional velocities. (Although the effects of friction are not included in the current effort, such effects could be incorporated via the simultaneous solution of the angular momentum balance in conjunction with a suitable friction model.)

3.1.2 Cohesive Interactions

Based on the square-well potential, cohesive forces are incorporated into the simulation as instantaneous forces whenever the separation distance is equal to $2r_{outer}$. These forces occur when two particles are approaching one another or when they are moving away from each other. A typical interaction sequence is shown in Figure 3.3.

The *approaching-cohesive* interaction occurs when distant particles become separated by

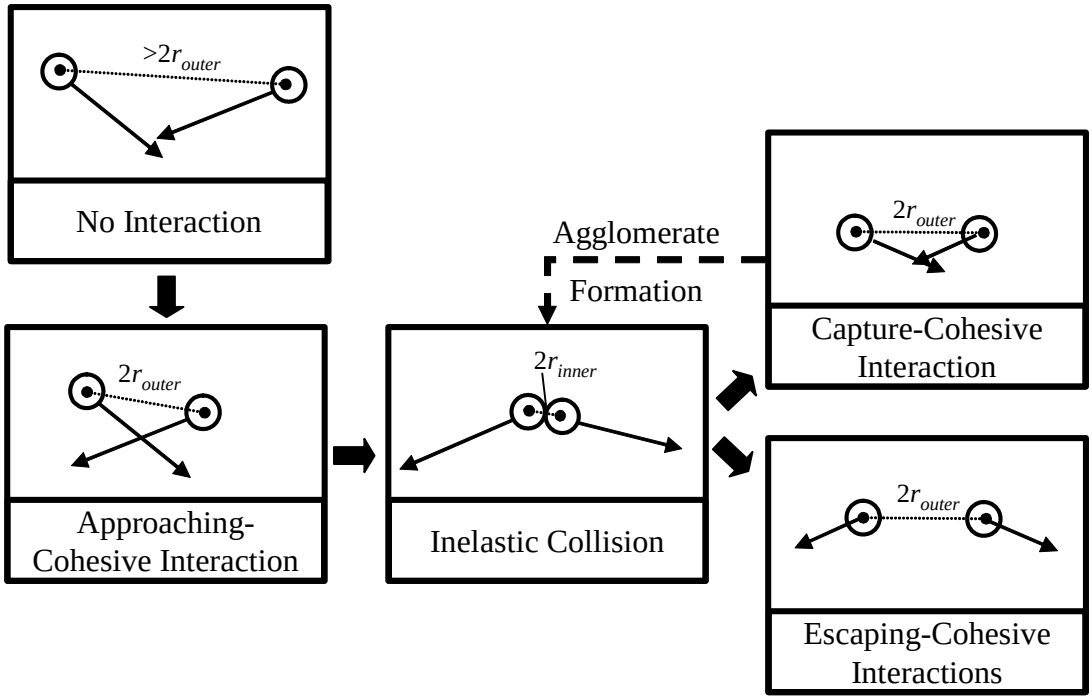

Fig. 3.3 *Square-well interaction sequence*

$2r_{outer}$. At this point, particles experience an instantaneous, attractive force (which corresponds to an increase in the normal component of the relative velocity between particles). Particles then move in a straight-line trajectory which leads to an inelastic collision if the particle separation distance reduces to $2r_{inner}$. Following the collision, particles travel in a straight path until the *departing-cohesive* interaction, which occurs at a separation distance of $2r_{outer}$. If the magnitude of the relative, normal velocity is not large enough, an internal reflection of the particles from the well occurs, which is referred to as a *capture-cohesive* interaction. In this case, the trajectory is symmetric about the outer wall of the square well, which may lead to another inelastic collision (thereby resulting in a further loss of granular energy).

Presuming no collisions with a third particle, this process will repeat and the particle agglomerate is forever bound. In this limit, repeated, inelastic collisions become successively more grazing (due to the continual reduction of normal relative velocity associated with inelastic collisions), and hence a state is approached where there is no further loss in granular energy. Alternatively, if a departing interaction between particles is characterized by a normal, relative velocity which is great enough to overcome the cohesive well, then an *escaping-cohesive* interaction occurs at a separation distance of $2r_{outer}$. At this instant, the particles experience a reduction in their normal, relative velocity and continue to separate.

Although the physical picture of the interaction sequence shown in Figure 3.3 is limited to two particles (for purposes of simplicity), the square-well description also allows for agglomerates of more than two particles. Furthermore, the agglomerates formed via the square-well approach are dynamic in nature. Animations of the simulated system indicate that agglomerates continuously form, rearrange and break apart.

It is worthwhile to note that the dynamics of agglomerates formed using the square-well potential (i.e., a "bouncing" between physical contact and the cohesive well) are different than that of more elaborate models (like a Hamaker model for van der Waals forces), which have cohesive interactions that are non-conservative (in which particles "stick" for extended periods of time). However, the maximum separation distance between particles in a square-well agglomerate is small (~0.1% of particle radius). Furthermore, the normal component of relative velocity is reduced after each inelastic collision, and hence the motion between the agglomerated

particles becomes more tangential in nature. As a result, the dynamic appearance of the square-well agglomerates closely mimics that of more elaborate models. Namely, the particles remain extremely close and appear to rotate around a common axis. A mathematical description of these cohesive interactions is given below.

Similar to inelastic collisions, overall momentum is conserved during a cohesive interaction. To solve for the post-collisional velocities, a second relation is necessary. For both inelastic collisions and cohesive interactions, this relation is derived from an appropriate kinetic energy balance. For inelastic collisions, kinetic energy is dissipated in accordance with equation 3.3. For cohesive interactions, however, kinetic energy can be gained, lost or stay the same depending on the type of cohesive interaction experienced. In particular, (i) potential energy is converted to kinetic energy (resulting in kinetic energy gain) for approaching-cohesive interactions, (ii) kinetic energy is converted to potential energy (resulting in kinetic energy loss) for escaping-cohesive interactions and (iii) kinetic energy remains the same for capture-cohesive interactions.

For the case of an approaching-cohesive interaction, energy conservation leads to the relation

$$\vec{k}_{ij,1} \cdot \vec{v}_{ij,b} = \sqrt{\frac{4D}{m} + \left(\vec{k}_{ij,1} \cdot \vec{v}_{ij,a}\right)^2} \tag{3.6}$$

where $\vec{v}_{ij,a}$ is the relative velocity of the particles before the cohesive interaction and $\vec{k}_{ij,1}$ is the unit vector pointing from the center of the ith particle to the center of the jth particle when the approaching particles are separated by $2r_{outer}$. When this relation is

combined with the momentum balance, the momentum impulse during an approaching-cohesive interaction is found as

$$J_{coh,app} = \frac{m}{2}\left(\vec{k}_{ij,1} \cdot \vec{v}_{ij,a} - \sqrt{\frac{4D}{m} + \left(\vec{k}_{ij,1} \cdot \vec{v}_{ij,a}\right)^2}\right) \tag{3.7}$$

For the departing interaction, two possibilities exist. First, the particles can continue to separate. In this case, using energy conservation, the following relationship is derived:

$$\vec{k}_{ij,3} \cdot \vec{v}_{ij,d} = -\sqrt{\left(\vec{k}_{ij,3} \cdot \vec{v}_{ij,c}\right)^2 - \frac{4D}{m}} \tag{3.8}$$

where $\vec{k}_{ij,3}$ is the unit vector pointing from the center of the ith particle to the center of the jth particle when the departing particles are separated by $2r_{inner}$ and $\vec{v}_{ij,d}$ is the relative velocity of the particles after escaping the square well. Similar to the procedure used with approaching-cohesive interactions, equation 3.8 is combined with the momentum balance to derive the following relation for the impulse during an escaping-cohesive interaction:

$$J_{coh,esc} = \frac{m}{2}\left(\vec{k}_{ij,3} \cdot \vec{v}_{ij,c} + \sqrt{\left(\vec{k}_{ij,3} \cdot \vec{v}_{ij,c}\right)^2 - \frac{4D}{m}}\right) \tag{3.9}$$

However, if the value inside the square root in equation 3.8 is negative, particle escape from the attractive well is not possible. Instead, internal reflection from the wall of the square well occurs and the particles form a dynamic agglomerate. In this case, the normal, relative velocity between the two particles does not change in magnitude, but simply changes its direction:

$$\vec{k}_{ij,3} \cdot \vec{v}_{ij,b} = -\vec{k}_{ij,3} \cdot \vec{v}_{ij,c} \tag{3.10}$$

When equation 3.10 is combined with the conservation of momentum, the following relation is found for the momentum impulse during a capture-cohesive interaction:

$$J_{coh,cap} = m\left(\vec{k}_{ij,3} \cdot \vec{v}_{ij,c}\right) \tag{3.11}$$

It is worth noting that the relative velocity resulting from a capture-cohesive interaction ($\vec{v}_{ij,b}$, equation 3.10) is referred to using the same symbol that is used to refer to the relative velocity before an inelastic collision (equation 3.3). This repetition was intended to keep the nomenclature consistent, since a capture-cohesive interaction will generally be followed by an inelastic collision. Moreover, the relative velocity between the two particles does not change until an interaction is actually resolved, even though the *normal* component of the relative velocity (between particle contacts) is constantly changing as the particles move.

In summary, equations 3.7, 3.9 and 3.11 are used in conjunction with equations 3.1 and 3.2 to determine the outcome of the various types of cohesive interactions.

3.2 Initialization, Steady-State Criteria and Data Collection

Initial particle positions are obtained by placing the particles on a square grid and giving each particle a random displacement from the lattice node. The distance between nodes is made as large as possible while still creating enough nodes so that there is at least one free node for each particle. This size of the random displacement

is made small enough such that particles on adjacent nodes will not overlap even after the displacement is made. Initial, random components of velocity in the *x*- and *y*-direction for each particle ($v_{x,i}, v_{y,i}$) are obtained using a random number generator. These velocities are bounded such that their maximum magnitude is less than or equal to the shear velocity. A mean velocity component is added to the *x*-velocity of each particle to achieve the desired shear profile in the system. Finally, the net momentum in the system is set to zero in each direction by first summing the net momentum in both directions. The net momentum in both directions is then divided by the total mass in the system and this resulting quantity is subtracted from the appropriate velocity component of each particle.

Data collection does not start until each particle has experienced 2500 collisions. After this period, all components of the collisional and kinetic stress (as defined in Equations 3.14-3.16 below) are collected at regular intervals, namely every 500 collisions per particle. The average number of particles per agglomerate and the average agglomerate duration (as defined in Equations 4.3-4.5, Chapter 4) are also collected at each interval. Once each of these calculated values does not vary by more than two percent over two consecutive intervals, the simulation is assumed to have reached a statistical steady state. Typically, simulations run for three intervals before a steady state is achieved.

3.3 Simulation Inputs

The parameters needed as inputs to the simulation are the cohesive well depth (D), the particle radius (r_{inner}), the width of the square well (r_{outer}), the restitution coefficient (e), the solids area fraction (ϕ), the domain length (L), the shear rate (γ) and the material density of the particles (ρ_s). The five dimensionless quantities that characterize the system are summarized in Table 3.1. Correspondingly, L, γ, and ρ_s are set equal to 1.0 for simplicity, while the remaining input parameters (D, r_{inner}, r_{outer}, e, and ϕ) are used as independent control parameters. These five dimensionless parameters are varied to determine their effect on the system. All other system parameters can be calculated from the specified parameters, including the number of particles (N):

$$N = \frac{L^2 \phi}{\pi \cdot r_{inner}^2} \tag{3.12}$$

as well as the particle mass:

$$m = \pi \cdot r_{inner}^2 \rho_s \tag{3.13}$$

Table 3.1 *Dimensionless simulation inputs*

Input	Description
L / r_{inner}	ratio of domain length to particle radius
e	coefficient of restitution
ϕ	solids area fraction
$D^* = \dfrac{D}{\gamma^2 (2r_{inner})^5 \rho_s}$	dimensionless cohesive well depth
r_{outer} / r_{inner}	ratio of well width to particle radius

3.4 Simulation Outputs

Among the outputs calculated in the simulation are the granular temperature (T) and each component of the stress tensor (τ_{xx}, τ_{yy}, and τ_{xy}). The stress tensor in this system has two contributing sources: kinetic (streaming) generation and collisional generation. The total stress is calculated by summing the contributions from these two sources.

Kinetic stress is generated by the transfer of momentum as particles move through the shear velocity field. The kinetic contribution to the total stress is calculated according to the random velocity components of each particle [2]:

$$\tau_{xx(kin)} = \frac{\rho_s \phi}{N} \sum_{i=1}^{N} v'_{x,i} v'_{x,i} \tag{3.14}$$

$$\tau_{yy(kin)} = \frac{\rho_s \phi}{N} \sum_{i=1}^{N} v'_{y,i} v'_{y,i} \tag{3.15}$$

$$\tau_{xy(kin)} = \frac{\rho_s \phi}{N} \sum_{i=1}^{N} v'_{y,i} v'_{x,i} \tag{3.16}$$

where

$$v_{x,i} = v'_{x,i} + \bar{v}_{x,i} \tag{3.17}$$

$$v_{y,i} = v'_{y,i} + \bar{v}_{y,i} \tag{3.18}$$

and $v_{x,i}$ represents the x-component of the velocity, $v_{y,i}$ represents the y-component of the velocity and the prime ($v'_{x,i}$) indicates the fluctuating component of the velocity and the overbar ($\bar{v}_{x,i}$) indicates the average component of the velocity (all for the ith particle). This average velocity in the x-direction as a function of the y-position is obtained by performing a least squares fit. The final reported value of the kinetic stress is averaged over several snapshots. Snapshots for averaging are taken after every collision once the initial 2500 collisions per particle have passed. Simulations proceed until all components of the stress vary by less than 1 percent over a 500 collision interval.

The collisional contribution to the total stress arises from the exchange of momentum between particles during inelastic collisions and cohesive interactions. This quantity is calculated by summing the impulses from each interaction type (inelastic and cohesive) over a given time interval and then dividing by that time and the area of the simulation domain [2]:

$$\tau_{xx(col)} = \frac{1}{A_{LE}\Delta t_{dc}} \sum_{i=1}^{n_{int}} J_* \frac{x_i - x_j}{R}\left(x_i - x_j\right) \tag{3.19}$$

$$\tau_{yy(col)} = \frac{1}{A_{LE}\Delta t_{dc}} \sum_{i=1}^{n_{int}} J_* \frac{y_i - y_j}{R}\left(y_i - y_j\right) \tag{3.20}$$

$$\tau_{xy(col)} = \frac{1}{A_{LE}\Delta t_{dc}} \sum_{i=1}^{n_{int}} J_* \frac{x_i - x_j}{R}\left(y_i - y_j\right) \tag{3.21}$$

where n_{int} is the total number of interactions that occurs during the data collection period, R is the center-to-center distance between particles, x_i and y_i represent the

position of the ith particle, A_{LE} is the area of the simulation domain (Lees-Edwards periodic domain), and Δt_{dc} is the time over which n_{int} interactions occur (i.e., the data collection period). J_* represents the magnitude of the momentum impulse transferred during the given inelastic collision (Equation 3.5) or cohesive interaction (Equations 3.7, 3.9 and 3.11).

The granular temperature is calculated according to the equation:

$$T = \frac{\frac{1}{2}\sum_{i=1}^{N}\left(v'_{xi}v'_{xi} + v'_{yi}v'_{yi}\right)}{N} \tag{3.22}$$

Finally, prior to reporting, both the stress and the granular temperature are non-dimensionalized as follows:

$$\tau_{ij}^{*} = \frac{\tau_{ij}}{\rho_s\left(2r_{inner}\gamma\right)^2} \tag{3.23}$$

$$T^{*} = \frac{T}{\left(2r_{inner}\gamma\right)^2} \tag{3.24}$$

Also, several parameters that characterize the agglomerates (e.g. average number of agglomerates, average agglomerate duration, average number of particle per agglomerate) in the system are also collected. These parameters will be explained in more detail in Section 4.2.2.

3.5 Time Advancement

As described in Section 2.2, the computational time needed for a simulation is greatly affected by the collision search algorithm that is employed – event-driven or time-stepped. Furthermore, the introduction of the square-well potential increases the required computational time by increasing the number of particle-particle interactions relative to the non-cohesive system. Also, the time step must be made small enough to capture interactions on the length scale associated with the distance between the particle radius and the width of the square well. An estimate of this length scale must be made in order to assess which collision search algorithm will require the least computational time in a cohesive simulation.

In order to obtain a practical estimate of this length scale, the van der Waals force between two spherical particles is considered based on the Hamaker theory:

$$F_{vdW} = \frac{A r_{inner}}{12 H^2} \tag{3.25}$$

where F_{vdW} is the van der Waals force between two particles, H is the surface-to-surface particle separation distance, and A is the Hamaker constant which is specific to the material in question. The Hamaker theory predicts that the attractive force between two particles will be negligible at very large separation distances, and will then gradually increase as the particles become closer. To determine the separation distance at which this force will first have a significant effect on particle motion, the magnitude of the force is compared to the weight of a 20-micron particle. Typical particle properties are assumed, namely a density equal to 1000 kg/m^3 and Hamaker constant equal to 10^{-20} J. This analysis indicates that the van der Waals force is equal

to the weight of one particle when a distance of 0.056 μm separates the two approaching particles. Correspondingly, the ratio of the square-well width to particle radius (r_{outer}/r_{inner}) must be approximately 1.001 for this case.

Using this ratio of the square-well width to particle radius, both event-driven and time-stepped algorithms were implemented in order to assess the most efficient method of implementing the cohesive simulation. While the time-stepped algorithm generally runs faster for systems with a relatively high radius ratio ($r_{outer}/r_{inner} = 1.1$), the event-driven algorithm is much more efficient as the radius ratio approaches one. At a typical radius ratio associated with the van der Waals forces ($r_{outer}/r_{inner} = 1.001$), simulations using the event-driven algorithm finish approximately ten times faster than simulations using the time-stepped algorithm. For these reasons, the event-driven search algorithm is used to collect all the results shown in Chapter 4.

3.6 References

1. A. W. Lees and S. F. Edwards, The computer study of transport processes under extreme conditions, *Journal of Physics C: Solid State Physics* 5 (1972) 1921.
2. C. S. Campbell, The Stress Tensor for Simple Shear Flows of Granular Material, *Journal of Fluid Mechanics* 203 (1989) 449.

Chapter 4. Granular Flow Results

The parameter space investigated includes solids fractions (ϕ) ranging from 0.1 to 0.5, coefficients of restitution (e) from 0.8 to 0.9, well width to particle radius ratios (r_{outer}/r_{inner}) from 1.1 to 1.0001 and dimensionless well depths (D^*) ranging from 0 to 15. The ratio of the domain length to the particle radius (L/r_{inner}) is kept constant at 120 for all simulations, as this was found to be large enough to ensure that the results are domain-size independent.

Before simulations are run with a large number of particles, a series of two-particle simulations are performed. The results of these simulations are verified with hand calculations to make sure that the inelastic collisions and cohesive interactions were being resolved correctly. These simulations are also used to evaluate a simplified, analytical description of cohesive interactions (as detailed in the following section). After considering the two-particle case, *many-particle* simulations are run with particles ranging in number from 458 to 2292. The results are characterized using snapshots of particle positions as well as simulation data for stress components, granular temperature, and agglomerate properties. The effectiveness of the square-well is then assessed by qualitatively comparing these results with experimental observations.

4.1 Two-Particle System

As a first step, simulations are performed for a two-particle system. After cohesive and collisional interactions occurred, particle positions and velocities were

checked against analytical solutions to ensure that all interactions are being resolved correctly. As depicted in Figure 4.1, the particles are initially given horizontal, approaching trajectories. The particle centers are offset in the vertical direction by an amount δ, which is less than the particle diameter ($2\,r_{inner}$) to ensure that a particle-particle interaction will occur. The coefficient of restitution is set at 0.8 and the dimensionless well depth is 5.0 for all simulations. The interactions were checked by hand for the cases of agglomeration and escape involving two particles, and breakup of a 2-particle agglomerate by a third particle.

For the 2-particle simulations in which an agglomerate does not result (i.e., escaping-cohesive interaction), an *effective* coefficient of restitution (e_{eff}) is calculated based on the approaching and departing normal, relative velocities:

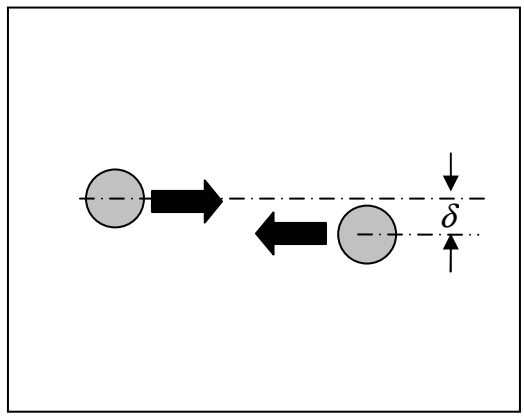

Fig. 4.1 *Geometry of two-particle simulations*

$$e_{eff} = -\frac{\vec{k}_{ij,3} \cdot \vec{v}_{ij,d}}{\vec{k}_{ij,1} \cdot \vec{v}_{ij,a}} \tag{4.1}$$

Note that the approaching normal, relative velocity ($\vec{k}_{ij,1} \cdot v_{ij,a}$) and departing normal, relative velocity ($\vec{k}_{ij,3} \cdot \vec{v}_{ij,d}$) are evaluated when the center-to-center distance of the two particles is equal to $2r_{outer,}$ unlike the actual restitution coefficient which is based on a separation distance of $2r_{inner}$. This difference arises since e_{eff} incorporates both

cohesive interactions and inelastic collisions, whereas e only characterizes the inelastic collision.

At the limit of $r_{outer} \rightarrow r_{inner}$, an analytical estimate of e_{eff} can be made for interaction sequences between two particles that escape the square well. This derivation is detailed in Appendix A. For this limiting case, the positions of two particles essentially remain unchanged throughout the entire interaction sequence (approaching cohesive interaction→inelastic collision→escaping cohesive interaction). Hence, the effective restitution coefficient as r_{outer}/r_{inner} approaches one is:

$$e_{eff,r_{outer}=r_{inner}} = \sqrt{e^2 + \frac{4\left(e^2-1\right)D}{m\left(\vec{k}_{ij,1}\cdot\vec{v}_{ij,a}\right)^2}} \tag{4.2}$$

An examination of this equation reveals that the *effective* restitution coefficient at the limit of $r_{outer}=r_{inner}$ is lower than the *actual* restitution coefficient (e). In other words, the attractive square well serves to increase the energy dissipation relative to that of a non-cohesive system.

Figure 4.2 shows the results of several 2-particle simulations for the case of non-agglomerated particles. The results indicate that $e_{eff,r_{outer}=r_{inner}}$ is very close to the simulation value (e_{eff}) for a r_{outer}/r_{inner} of 1.0001 (Figure 4.2b). However, as r_{outer}/r_{inner} increases to 1.1 (Figure 4.2a), the assumption of r_{outer}/r_{inner} ~ 1 worsens and $e_{eff,r_{outer}=r_{nneri}}$ does not show good agreement with the simulated value.

Based on the results of the 2-particle simulations, the use of the effective restitution coefficient in place of the more complete square-well approach is not valid

outside of the limits in which it was developed. Because these limits are fairly restrictive, namely 2-particle, non-agglomerating interactions with $r_{outer}/r_{inner} \sim 1$, an approximation to the square-well model based on the use of an effective restitution coefficient does not appear to be a promising approach for more general, cohesive systems (systems with particle agglomeration, multi-particle interactions, etc.).

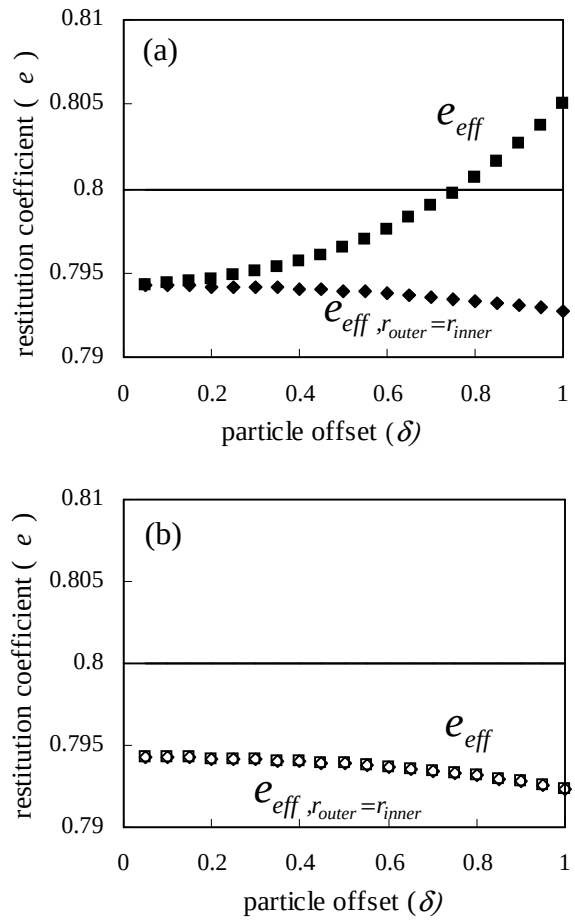

Fig. 4.2 *Calculated (equation 4.2) and simulated values of the effective coefficient of restitution as a function of the vertical particle offset (δ) in two-particle simulations for e=0.8 and (a) r_{outer}/r_{inner} = 1.1 and, (b) r_{outer}/r_{inner} =1.0001.*

4.2 Many-Particle System

4.2.1 Flow Regimes

An important observation from the many-particle simulation results is that cohesive forces lead to the development of two markedly different flow regimes. Systems characterized by relatively large cohesive forces ($D^* \geq 15$) tend to form a single, large agglomerate that includes most of the particles in the domain. For systems with relatively small cohesive forces ($D^* < 15$), the particles remain fairly evenly distributed throughout the domain, forming mostly 2-particle agglomerates (though agglomerates of more than two particles also exist). The difference between these two flow regimes is shown in the simulation snapshots of particle configurations in Figure 4.3. Systems in the top and bottom row are characterized by D^*=25 and 30, respectively. As expected, the transition *between mild cohesion* ($\phi \leq 0.3$) and *strong-cohesion* ($\phi \geq 0.4$) regimes for D^* = 25 occurs at a higher solids fraction than for the system with D^* = 30 ($\phi \geq 0.3$). Furthermore, the transition between the mild-cohesion and strong-cohesion regimes is observed to be fairly abrupt. Specifically, the middle row of Figure 5 also contains snapshots for D^* = 25, but in a much smaller range of ϕ. Even within this narrow range, no smooth transition is observed. Reproducible stress values cannot be obtained for simulations operating in the strong cohesion regime because the non-uniform particle distribution leads to very poor results when trying to fit the profile of the average velocity. This

erratic average velocity leads to values of the kinetic stress that are inconsistent from run to run for the same set of operating parameters.

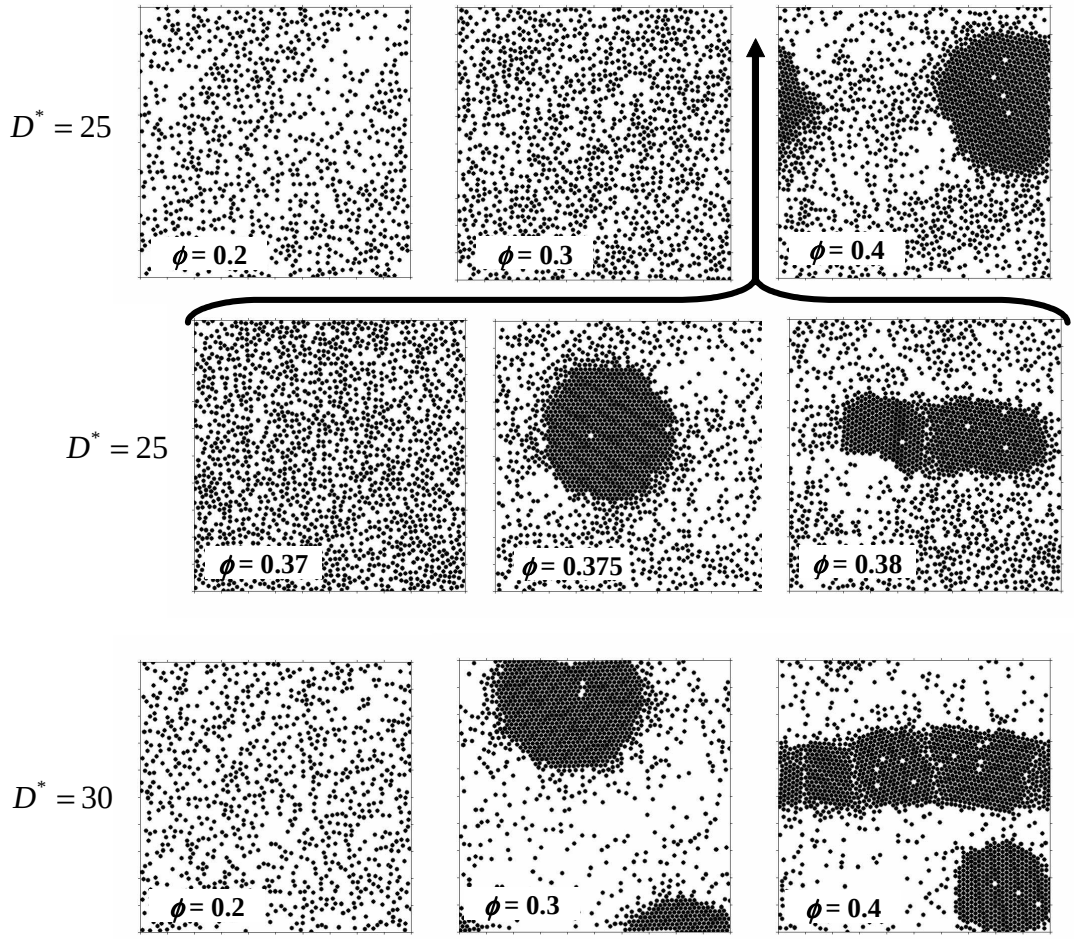

Fig. 4.3 *Snapshots of particle configuration showing transition from mild cohesion to strong cohesion regime. A dimensionless well depth of 25 (top row) shows the transition between solids fractions (ϕ) of 0.3 and 0.4, while a well depth of 30 (bottom row) shows the transition between solids fractions of 0.2 and 0.3. Middle row illustrates abrupt nature of transition over very narrow ranges of solids fraction.*

The abrupt transition observed between the mild-cohesion and strong-cohesion regimes is reminiscent of the transition observed between Geldart Type C and Type A powders (as described in Section 1.3.2.1). Although the focus of the current work is on a *granular* system and the Geldart classification system is for a *gas-solid* system, similarities do exist between the systems. Both systems involve

relatively massive particles, which engage in particle-particle collisions that are dissipative in nature. Whether or not such similarities are responsible for the abrupt regime transition observed in both types of cohesive systems, however, remains uncertain and is beyond the scope of the current effort. The ability of the square-well model to predict Geldart transitions in a simulation of a fluidized system will be described in Chapter 7.

4.2.2 Mild-Cohesion Regime

Within the mild-cohesion regime, the simulations achieve a statistical steady-state with computational times ranging from 4 minutes to 48 hours on a Pentium 4 processor. All simulations are characterized by a domain length to particle radius ratio (L/r_{inner}) equal to 120. The constraints on input parameters needed to stay in the mild cohesion regime are somewhat limiting. Specifically, the mild-cohesion parameter space is more restrictive at lower restitution coefficients (e ~ 0.8) and radius ratios closer to one (r_{outer}/r_{inner} ~ 1.00001). With e = 0.9 and a r_{outer}/r_{inner} = 1.001, however, many noticeable trends were observed while varying ϕ from 0.1 to 0.5 and D^* from 0 to 15. Additional features were observed by maintaining D^* = 10 and varying r_{outer}/r_{inner} in the range of 1.1-1.0001 and ϕ in the range of 0.1 to 0.5.

As mentioned previously, the agglomerates formed in the mild-cohesion regime are typically composed of only a few particles (Figure 4.3) and are very dynamic in nature (i.e., agglomerates continually form, rearrange and break up). In order to characterize these agglomerates in a quantitative manner, several quantities

were monitored throughout the simulation, including the agglomerate duration and size. The agglomerate duration (Δt_{agg}) is a measure of the average amount of time that a given particle retains at least one agglomerate partner after first being captured, namely:

$$\Delta t_{agg} = t_{esc} - t_{agg} \tag{4.3}$$

where t_{agg} is the system time at which a given particle first enters into an agglomerate (this agglomerate may include more than two particles) and t_{esc} is the system time at which that particle is no longer agglomerated with any other particles. This quantity is averaged over all occurrences of particles that become agglomerated and later escape all agglomerated partners:

$$\Delta \bar{t}_{agg} = \frac{1}{n_{esc}} \sum_{i=1}^{n_{esc}} \Delta t_{agg,i} \tag{4.4}$$

where n_{esc} is the number of occurrences of a particle becoming agglomerated and then later escaping from all agglomerate partners. The average number of particles per agglomerate is calculated by counting the number of particles in each agglomerate at a given instant, averaging that number over all agglomerates in that snapshot, and then averaging that value over several snapshots:

$$\bar{P} = \frac{\sum_{k=1}^{n_{s,agg}} \Delta t_k \left(\frac{\sum_{i=1}^{n_{agg,k}} P_{i,k}}{n_{agg,k}} \right)}{\sum_{k=1}^{n_{s,agg}} \Delta t_k} \tag{4.5}$$

where $P_{i,k}$ is the number of particles in a given agglomerate at the kth snapshot, $n_{agg,k}$ is the total number of agglomerates at the kth snapshot, Δt_k is the time step associated with the kth snapshot (because the event-driven simulation proceeds from collision to collision, the time step continually changes) and $n_{s,agg}$ is the number of snapshots for averaging of agglomerate properties. According to this equation, snapshots associated with longer times between interactions are weighted more heavily than those with smaller times between interactions. If each snapshot was not weighted by its associated time step, then the averaging process would tend to exaggerate the level of agglomeration in the system since agglomeration leads to shorter times between particle interactions and thus a higher frequency of snapshots. Approximately two thousand snapshots are used in the averaging process for all agglomerate properties.

Figure 4.4 shows the variation of agglomerate duration and number of particle per agglomerate at e = 0.9, r_{outer} / r_{inner} =1.001 and D^* = 0-15. As illustrated in Figure 4.4a, as the strength of the cohesive force (D^*) is increased, a given particle has a reduced chance of escaping from any particles with which it is agglomerated, thereby leading to a longer average agglomerate duration. As expected, Figure 4.4b shows that the average number of particles per agglomerate increases as the strength of cohesive forces (D^*) is increased. Also evident from these plots is that the average agglomerated time decreases as the solids fraction is increased, but the average number of particles per agglomerate increases as the solids fraction is increased. An explanation for this observation is linked to the increasing number of particles per area as the solids fraction is increased. This increase leads to more particles in each agglomerate. However, the increased number of particles will also lead to more

interaction between agglomerates and therefore a higher frequency of breakup. Thus, while higher solids fractions will lead to the average agglomerate containing more particles, the involved particles will get reshuffled between the agglomerated and unagglomerated state at a higher frequency.

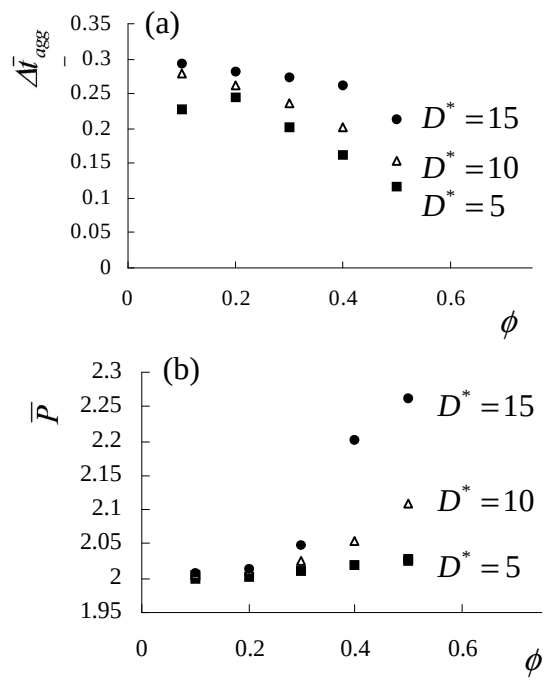

Fig. 4.4 *Average agglomerate duration ($\Delta\bar{t}_{agg}$) and average number of particles per agglomerate ($\bar{P}$) at varying cohesive well depths (D^*) with r_{outer}/r_{inner}=1.001 and e=0.9.*

Figure 4.5 displays the effect of r_{outer}/r_{inner} on agglomerate characteristics. All data in Figure 4.5 was obtained using a dimensionless well depth of 10 and a restitution coefficient of 0.9. Increasing r_{outer}/r_{inner} essentially makes every particle a larger target. Correspondingly, additional cohesive interactions will occur. Such glancing collisions will increase the rate of agglomeration and have a negligible effect on deagglomeration. Hence, the average number of particles per agglomerate will increase with r_{outer}/r_{inner} (Figure 4.5b). In addition, any agglomerated particle will

retain at least one agglomerate partner for a longer period of time (on average) as r_{outer}/r_{inner} increases (Figure 4.5a).

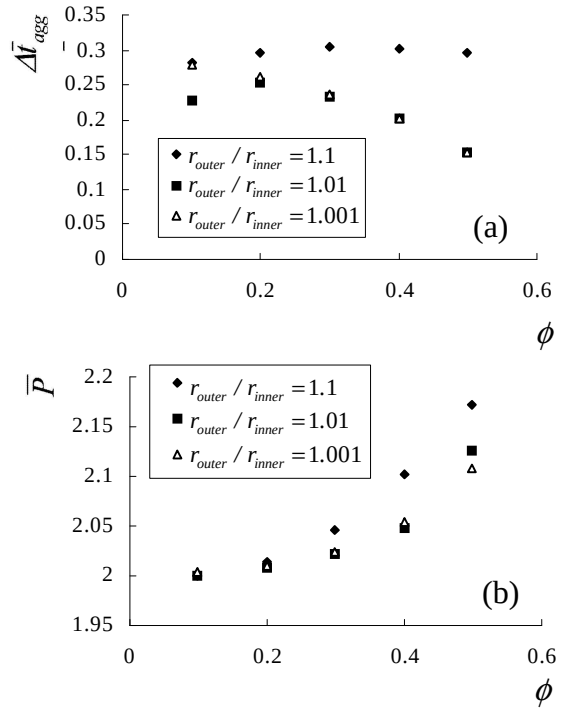

Fig. 4.5 *The average agglomerate duration ($\Delta\bar{t}_{agg}$) and average number of particle per agglomerate ($\bar{P}$) for varying ratio of the well width to inner radius (r_{outer} / r_{inner}) with $D^*=10$ and e=0.9.*

Figure 4.6 displays the effect of cohesive forces on the *xx*-component of the normal stress tensor (τ^*_{xx}) as a function of the solids fraction for r_{outer}/r_{inner} = 1.001 and e = 0.9. As seen in Figure 4.6, the stress generally decreases as the magnitude of the cohesive forces (D^*) increases. Similar results are obtained for the *yy*-component of normal stress. As seen in the graph, the largest deviations from the zero-cohesion ($D^* = 0$) case are found for ϕ > 0.3 (collisional-flow regime), in which particle-particle interactions are the dominant mechanism for momentum transfer. Because the cohesive forces are only significant when particles are in close proximity to one

another, no significant changes to stress occur at ϕ < 0.3, in which the streaming (kinetic) mechanism is responsible for the majority of momentum transfer.

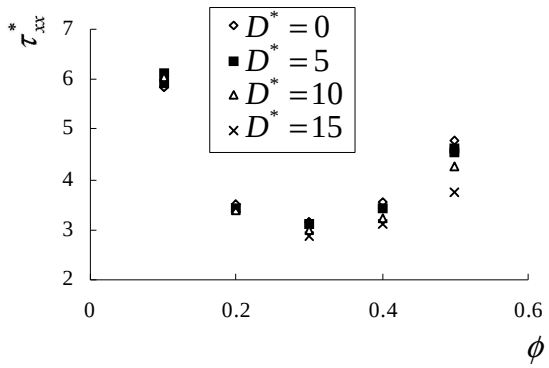

Fig. 4.6 *Normal stress (xx-component) for varying cohesive well depth (D^*) with r_{outer}/r_{inner}=1.001 and e=0.9.*

In order to further investigate the observed trend of decreasing normal stress with increasing cohesive forces, the four contributions to τ^*_{xx} are examined on an individual basis. In particular, Figure 4.7 shows the portion of τ^*_{xx} that is due to approaching-cohesive interactions (Figure 4.7a), escaping-cohesive interactions (Figure 4.7b), inelastic collisions (Figure 4.7c) and capture-cohesive interactions (Figure 4.7d) for the same set of conditions portrayed in Figure 4.6. By definition (equations 3.7, 3.9 and 3.11), the momentum impulse during cohesive interactions is always negative. Thus, the normal component of the stress coming from these interactions will always be negative as is consistent with subplots (a), (b), and (d). Furthermore, these plots indicate that as D^* increases, the stress contributions from cohesive interactions become more negative. The contribution to τ^*_{xx} arising from inelastic collisions, however, increases as D^* increases (Figure 4.7d), which is opposite to the behavior of the total stress tensor (Figure 4.6). A comparison of the magnitudes of the four contributions to the total stress tensor (Figure 4.7) indicates

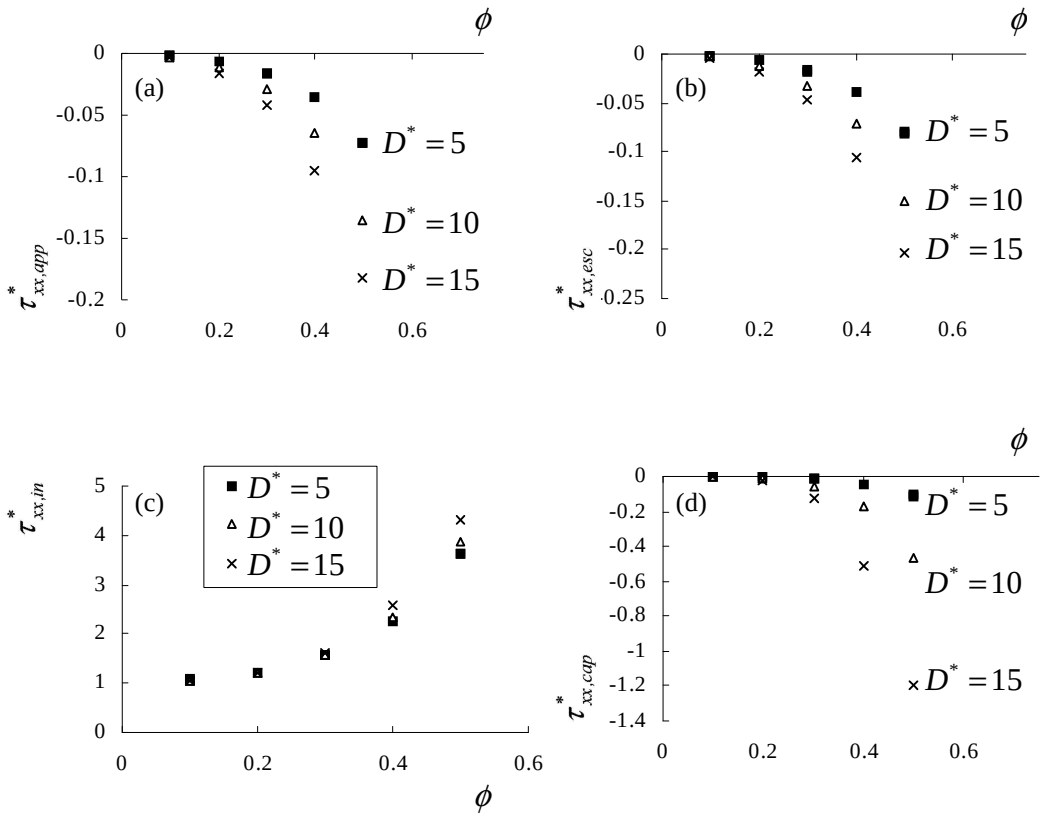

Fig. 4.7 *Normal collisional stress (xx-component) coming from(a) approaching-cohesive interactions,(b) escaping-cohesive interactions,(c) inelastic collisions, and (d) capture-cohesive interactions for* r_{outer}/r_{inner}*=1.001 and e=0.9.*

that inelastic collisions and capture-cohesive interactions have the largest influence on the behavior on the total stress. This observation can be traced to the frequency of these two interactions (not plotted here). Namely, both inelastic collisions and capture-cohesive interactions occur much more often due to agglomeration. Hence, the stress from inelastic collisions *increases* as cohesive forces are added to the system, the stress from capture cohesive interactions *decreases* to a larger degree and the net effect is a decrease in the total stress, as is displayed in Figure 4.8. The additional decrease in total stress arises from the additional approaching- and escaping-cohesive interactions which account for roughly 20% of the net decrease (Figures 4.7a and 4.7b).

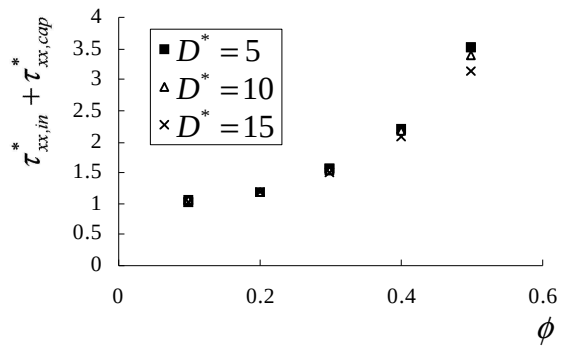

Fig. 4.8 *Sum of the portion of normal stress (xx-component) coming from inelastic collisions and capture cohesive interactions for* $_{outer}/r_{inner}$*=1.001 and e=0.9 .*

Similar effects are seen when r_{outer}/r_{inner} is decreased as shown in Figure 4.9 for a $D^* = 10$ and $e = 0.9$. In particular, the *xx*- and *yy*- components (not shown) of the normal stress decrease as the radius ratio approaches unity. Further investigation shows that this decrease can again be traced to the increased frequency of inelastic collisions and capture-cohesive interactions, which is analogous to the behavior observed when D^* is increased. However, in this case the increased number of inelastic collisions and capture-cohesive interactions is not due to the formation of more agglomerates, but rather due to the decreased distance between r_{inner} and r_{outer}. This shortened distance allows more inelastic collisions and capture-cohesive interactions to occur in a shorter time per agglomerate, despite the observation that the agglomerates have a shorter average lifetime (Figure 4.5a).

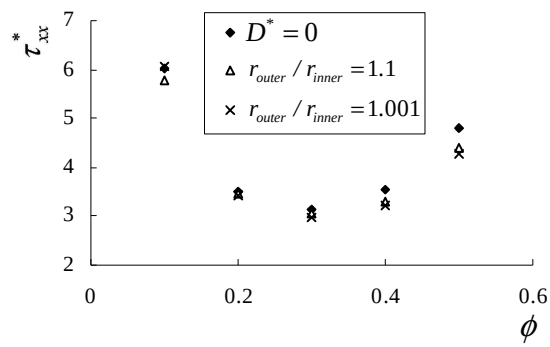

Fig. 4.9 *Normal stress (xx-component) with varying values of well width to inner radius ratio (r_{outer} / r_{inner}) for D^* =10 and e = 0.9.*

Similar to the normal stress, the shear stress component ($-\tau^*_{xy}$) exhibits a slight decrease in the collisional regime (high ϕ) as cohesive forces become stronger, as shown in Figure 4.10. These results were obtained at the same values of r_{outer}/r_{inner} and *e* as the data in Figures 4.6 - 4.8. To investigate the source of these changes, the collisional component of shear stress is again divided into the contributions from each type of interaction, as depicted in Figure 4.11. As with the normal stress, the approaching- and escaping-cohesive interactions lead to a decrease in $-\tau^*_{xy}$ with any

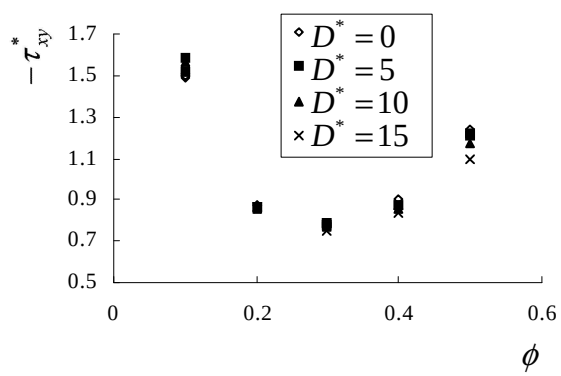

Fig. 4.10 *Shear stress (-xy-component) at varying cohesive well depths (D*) for r_{outer}/r_{inner}=1.001 and e=0.9.*

increase in D^*, though this is only a small part of the overall change in the total shear stress. Figure 4.11d reveals that the shear stress coming from capture-cohesive interactions is also relatively insignificant. The largest contribution to the change in

the total shear stress comes from inelastic collisions. This portion of the stress becomes smaller in magnitude as D^* increases as is illustrated in Figure 4.10c. This effect is the opposite of that seen with the inelastic contribution to the *normal* stress (Figure 4.7c).

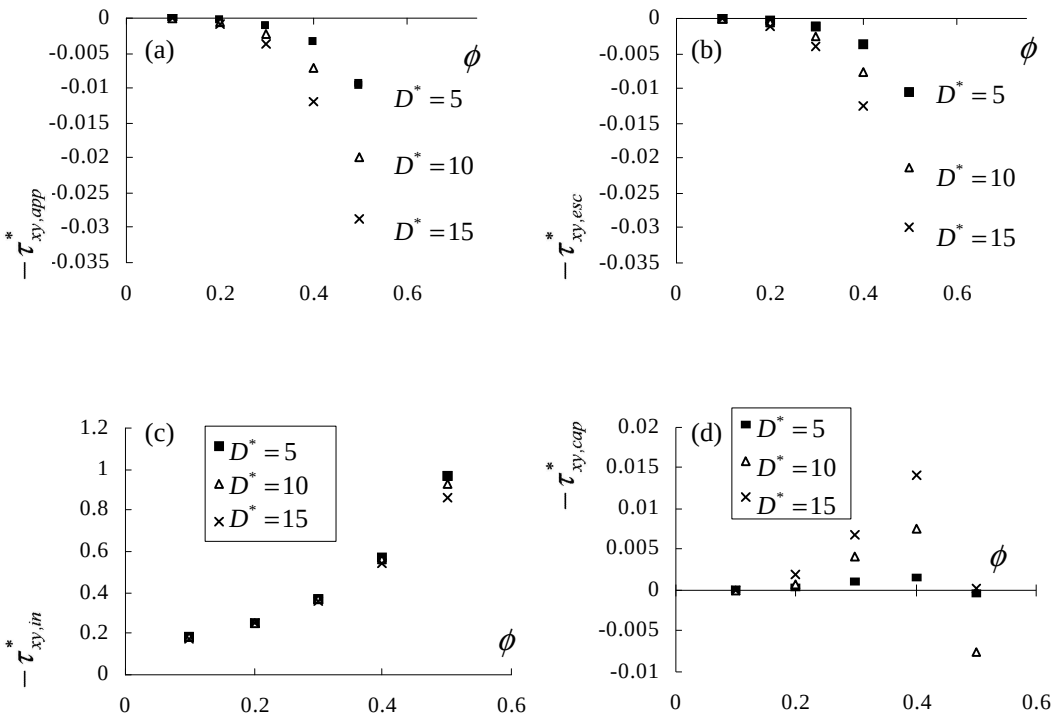

Fig. 4.11 *Shear stress (-xy-component) from (a) approaching-cohesive interactions, (b) escaping-cohesive interactions,(c) inelastic collisions, and(d) capture-cohesive interactions for* r_{outer}/r_{inner}*=1.001 and e=0.9.*

A possible physical explanation for this phenomenon is related to the direction of the imposed shear in the system, as shown in Figure 4.12. First, consider a cohesion-free system. If the particles do not have any random velocity and only move with the average velocity imposed by the shear, collisions will involve a particle in a part of the domain with a higher average velocity (particle 1 in Figure 4.12a) colliding with a particle in an adjacent part of the domain with a slower average velocity (particle 2 in Figure 4.12a). Particles that collide in this manner serve to

increase the magnitude of $-\tau_{xy}^{*}$ (transfer of positive momentum in a negative direction or negative momentum in a positive direction, see equation 3.21). Although the particles under consideration have both a random and a mean component of velocity, the collision orientation associated with the imposed shear (Figure 4.12a) will still be favored. Now consider a system with cohesive forces. Simulation data has shown that the introduction of cohesive forces leads to a decrease in the percentage of collisions associated with *shear orientation* (Figure 4.12a). Figure 4.12b illustrates how agglomeration can lead to a faster moving particle continuing to contact a particle in an adjacent, slower-moving part of the domain after initial contact. Simulation data indicates that more than half of the initial, inelastic collisions between two *non-agglomerated* particles are characterized by the shear orientation (Figure 4.12a). However, when considering *agglomerated* particles, a majority of the collisions are characterized by the orientation represented in Figure 4.12b. Collisions in the latter orientation result in a transfer of positive x-momentum in the positive y-direction, therefore decreasing the magnitude of $-\tau_{xy}^{*}$. When averaged over several thousand collisions, these additional collisions associated with agglomeration lead to a slight decrease in $-\tau_{xy}^{*}$.

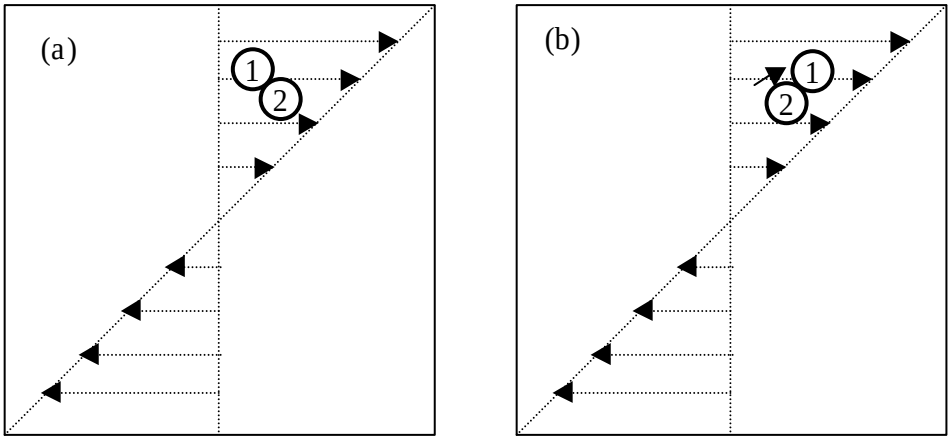

Fig. 4.12 *Diagram showing dominant (a) collision type in shear flow (b) with possible agglomerated collision.*

The trend of decreasing normal stress with increasing cohesive forces in the granular system studied here can be compared to trends observed in molecular gases (where molecular gases undergo *elastic* collisions). One method used to describe such systems is via a collection of hard spheres (which gives rise to repulsion between molecules) with a square-well potential (which gives rise to attraction between molecules). When the square-well potential is added to the hard-sphere description, the resulting attractive forces contribute negatively to the second virial coefficient [1]. The corresponding decrease in the second virial coefficient leads to a pressure that is lower than that associated with hard spheres only. The decrease in pressure is consistent with the simulation results shown here (Figure 4.5) in which the addition of a square well leads to a reduction in the normal components of the stress tensor (i.e. pressure).

From an experimental standpoint, Gidaspow and Huilin [2] have made related observations with electrostatically-charged FCC particles in a gas-fluidized bed. They found that at low volume fractions, the granular temperature, normal stress and

solids volume fraction obeyed a simple kinetic theory equation of state. However at higher solids volume fractions (when inter-particle cohesion is more significant), the kinetic-theory relation overpredicted the normal stress in the system. After making a correction to account for the attractive electrostatic forces, the relation agreed with the experimental data. This experimentally-observed tendency of cohesive forces to decrease the normal stress component is in qualitative agreement with the results shown in this work.

4.3 Summary of Granular Flow Results

Cohesive forces were introduced into a discrete-element simulation for rapid, granular shear flows using a square-well potential. An effective coefficient of restitution was derived for a 2-particle system in the limit of $r_{outer}/r_{inner} \rightarrow 1$. Comparisons with simulations indicate that the range of validity of the effective restitution coefficient is narrow. Hence, this approach does not appear to be a practical simplification of the more complete square-well potential.

For simulations involving a large number of particles, two different flow regimes are present. In the strong-cohesion regime, particles form a single, large agglomerate. In the mild-cohesion regime, particles form agglomerates that continuously form, rearrange, and disperse. Cohesive forces are found to have little effect on the stress at low solids fractions (kinetic regime), but decrease the total stress at higher solids fractions (collisional regime). This decrease in stress becomes more significant as the strength of the cohesive forces (D^*) is increased. These results are in qualitative agreement with the results of fluidized systems and molecular

systems (though clear differences do exist between these two pairs of systems, namely the presence of a fluid phase and perfectly elastic collisions, respectively).

The simulation results indicate that the square-well potential appears to be a viable method for incorporating cohesive forces into a description of rapid granular flow. In particular, the impulsive, instantaneous nature of the corresponding cohesive forces makes it a candidate for incorporation into kinetic-theory descriptions (since current theories are based on the assumption of binary, instantaneous particle collisions). To apply this model to practical systems, however, a mapping between square-well parameters and physical (measurable) quantities is needed. Although this analysis is not performed in relation to the granular flow simulation, such an effort is made in the context of the fluidized bed simulation, as is described in Chapter 7.

4.4 References

1. J. M. Prausnitz, R. N. Lichtenthaler, and E. G. de Azevedo, Molecular Thermodynamics of Fluid-Phase Equilibria, 3rd ed., Prentic Hall, Upper Saddle River, New Jersey, 1999.
2. D. Gidaspow and L. Huilin, Equation of state and radial distribution functions of FCC particles in a CFB, *AIChE Journal* 44 (2) (1998) 279.

Chapter 5. Literature Review of Models for Fluidized Flow Systems

Relative to granular systems, the development of a model for fluidized flow systems is more complex due to the two-way coupling between the two phases. In particular, the fluid phase is highly dependent on the state of the solid phase, and vice versa. For example, the portion of the system occupied by each phase is constantly changing as the particles move within the fluid. Likewise, the solid phase will be affected by pressure gradients in the fluid phase, and both phases will experience an equal and opposite drag force. Hence, a model of the system must take into account not only the mechanisms within in each phase, but also the mechanisms that couple these two phases.

One approach to coupling this two-phase system is to allow the fluid phase to move through a domain with boundaries defined by the changing positions of the particles (i.e., the domain occupied by the fluid has moving boundaries). The fluid phase equations would then be solved at every point occupied by the fluid and individual force balances would determine the motion of the particles. This direct numerical simulation of both phases has extremely high computational requirements, and is thus limited to systems containing only a few particles. At the other end of the spectrum, another possibility is to consider the effect of the particles on the fluid (and the fluid on the particles) uniform throughout the domain. However, spatial variations in both phases are present (e.g., bubbles in a fluidized bed), so this approach is not appropriate. A common ground between these two approaches is to use a technique based on local averaging (see, for example, [1]).

To describe the fluid phase via local averaging, an assumption is made that the macroscopic variation of the system parameters is on a length scale that is much larger than the particle spacing yet much smaller than the system dimensions. A weighting function is used to transform point values into volume-averaged values that are defined in terms of volume occupied by both phases. For an isothermal, non-reacting, incompressible system, this approach leads to the following expressions for the fluid-phase mass balance and momentum balance:

$$\frac{\partial \varepsilon_s}{\partial t} + \nabla \cdot \left(\varepsilon_g \vec{v}_g\right) = 0 \tag{5.1}$$

$$\rho_g \left[\frac{\partial}{\partial t}\left(\varepsilon_g \vec{v}_g\right) + \nabla \cdot \left(\varepsilon_g \vec{v}_g \vec{v}_g\right) \right] = \nabla \cdot \bar{S}_g + \varepsilon_g \rho_g \vec{g} - \vec{I}_{gs} \tag{5.2}$$

where ε_g is the volume fraction of the fluid phase, ρ_g is the fluid density, $\vec{v}_g$ is the fluid velocity, $\bar{S}_g$ is the fluid-phase stress tensor, $\vec{g}$ is the acceleration due to gravity and $\vec{I}_{gs}$ is the rate of momentum transfer between the fluid and solid phase per unit volume.

In addition to the locally-averaged fluid phase equations, a second set of equations is required to describe the solid phase. These equations can be developed using either a discrete-particle (Lagrangian) or continuum (Eulerian) approach. Both of these approaches start with the equation of motion for a single particle:

$$\forall \rho_s \frac{d\vec{v}_i}{dt} = \vec{F}_i \tag{5.3}$$

where $\forall$ is the single particle volume, $\vec{v}_i$ is the single particle velocity and $\vec{F}_i$ is the sum of all forces acting on the particle (e.g., gravity, fluid-solid drag force, particle-particle contact force). For a discrete-particle approach, equation 5.3 is integrated

numerically for each particle. Local average quantities (e.g. average solid velocity and solids volume fraction) are based on a computational grid. The properties of all particles within a given grid cell are averaged in order to obtain locally-averaged properties that can be interfaced with the fluid-phase continuum equations. The combination of a locally-averaged fluid-phase equations with a numerical solution of the equations of motion for each individual particle is referred to as and Eulerian-Lagrangian technique (since the fluid is treated in a continuum manner and the particles are treated in a discrete manner).

The solid phase can also be described using a continuum approach. Application of local volume-averaging to the equation of motion for a single particle leads to the following expression for the solid-phase momentum balance:

$$\rho_s\left[\frac{\partial}{\partial t}\left(\varepsilon_s\vec{v}_s\right)+\nabla\cdot\left(\varepsilon_s\vec{v}_s\vec{v}_s\right)\right]=\nabla\cdot\overline{S}_s+\varepsilon_s\rho_s\vec{g}+\vec{I}_{gs} \qquad (5.4)$$

where ε_s is the solids volume fraction, $\vec{v}_s$ is the locally-averaged solid velocity, $\overline{S}_s$ is the solid-phase stress tensor and ρ_s is the solid density. This expression can be solved with equation 5.2 along with the following continuity relation:

$$\varepsilon_s+\varepsilon_g=1 \qquad (5.5)$$

to obtain a complete description of the two-phase system. The combination of a locally averaged equation for the solid phase with a locally-averaged equation for the fluid phase is referred to as an Eulerian-Eulerian approach (since both phases are treated as a continuum).

In general, the Eulerian-Eulerian approach is computationally more efficient and therefore can be applied to systems with a larger number of particles than the

Eulerian-Lagrangian approach, which is limited to approximately 100,000 particles. However, incorporation of complex particle physics (e.g., cohesion) is a more difficult task with Eulerian-Eulerian models. In particular, volume-averaging of the particle momentum balance gives rise to the solid-phase stress tensor (Equation 5.5), which requires a constitutive relation. The impact of cohesion on such a continuum quantity is more difficult to model than its incorporation on a particle-particle level (as is necessary for the Eulerian-Lagrangian approach). The next few sections will discuss some of the details of these two simulation techniques and review some previous efforts in each area.

5.1 Eulerian-Eulerian Models

As mentioned above, a fully specified set of equations for the solid phase require a constitutive model for the solid phase stress tensor ($\overline{S}_s$). Such closures have been pursued at various levels of complexity for roughly the last four decades. Early efforts employed semi-empirical methods to determine the solids viscosity (see, for example, [2]). The application of the kinetic theory of gases to solids allows for a more fundamental description of the solid-phase stress terms (see, for example, [3]). Sinclair and Jackson [4] were the first to apply this kinetic-theory approach to an Eulerian-Eulerian model of a gas-solid system.

The focus of many subsequent Eulerian-Eulerian efforts has been to incorporate improved constitutive relations for the solid phase. A detailed review of these advances for kinetic-theory relations is given in reviews by Campbell [5] and

Gold Hirsch [6]. For a thorough review of the associated Eulerian-Eulerian models, the reader is referred to Sinclair [7], Enwald [8], and van Wachem [9].

5.2 Eulerian-Lagrangian Models

In order to model the particle phase in Eulerian-Lagrangian simulations, previous efforts have used both soft-sphere and hard-sphere techniques. As described in Section 2.1, soft-sphere models allow for the inclusion of more elaborate contact models, while hard-sphere models are generally more computationally efficient.

One of the first efforts to develop an Eulerian-Lagrangian fluidized bed simulation was made by Tsuji, *et al*. [10]. This effort used a soft-sphere, discrete-particle treatment similar to what had been developed by Cundall and Strack [11], and combined it with an Eulerian model for the gas flow. This simulation was used to study bubble flow and the results were shown to compare reasonably well with laboratory experiments. Subsequently the soft-sphere method has been used to study a wide variety of systems. Some examples of topics that have been studied using the soft-sphere method include bubble formation [12], binary systems [13], mixing [14], and cohesive systems [15-18], although this list is not comprehensive.

A noted drawback of the soft-sphere approach is that the particles are often made artificially soft in order to keep the simulation stable [19]. Nonetheless, many efforts have shown that the artificially soft nature of particles in soft-sphere models does not affect the overall particle flow [12, 18, 20, 21]. More detail on this issue is presented in Chapter 6.

Xu and Yu [19, 22] developed a model that utilized a time-stepped algorithm, however for each particle overlap the simulation is reversed so that the particles "back-up" to point of incipient contact. The repulsive force was still calculated using a soft-sphere model, but the maximum overlap was limited. This "predictor-corrector" method was used to produce realistic fluidized bed snapshots and pressure drop data.

An alternative to the soft-sphere approach is the application of a hard-sphere technique for the simulation of gas-solid systems. This combination was first utilized by Hoomans *et al*. [23]. In this system, gas-particle interactions are implemented followed by several collisions which are processed one (instantaneous) collision at a time. Some examples of systems that have been studied using this approach include binary systems [24], bubbling [25, 26], clustering [27, 28] and high pressure fluidization [29], as well as specific applications such as coal combustion [30] and spray granulation [31] although this list is not comprehensive.

The enduring nature of particle contacts incorporated into the soft-sphere approach is an important consideration for systems with cohesive interactions. While impulsive cohesion models such as the square-well model can be incorporated into a hard-sphere approach, most cohesion models are defined as a continuous function of the particle separation distance. Hence, an event-driven algorithm would not be appropriate. As will be described in the next section, all previous attempts to incorporate cohesion into an Eulerian-Lagrangian fluidized bed simulation have used the soft-sphere approach.

5.3 Gas-Solid Models That Incorporate Cohesion

Despite the prevalence of cohesive forces in fluidized beds, efforts to implement cohesion into models of fluidized beds have been fairly limited. With regard to Eulerian-Eulerian models, no efforts have been documented to incorporate a model for cohesive effects into the governing equations. Mckeen and Pugsley [32] developed a two-fluid model for the fluidization of cohesive fluid catalytic cracking particles, however cohesion was accounted for by increasing the effective particle diameter in the drag relation. This effort did not implement a true cohesion model defined on a particle-to-particle basis. Efforts to incorporate cohesion into Eulerian-Lagrangian models are more numerous. Mikami *et al*. [18] incorporated a liquid-bridging model into a fluidized bed simulation. This effort produced pressure data illustrating an increase in the minimum fluidization velocity for wet particles relative to a dry system. The soft-sphere model developed by Mikami *et al.* has subsequently been extended by several investigators. Kuwagi *et al*. [33] applied a sintering model and studied its effects on the formation of dead zones in the fluidized bed. They also characterized the formation of agglomerates due to sintering. Rhodes and Wang [15] used the same fluidized bed model developed by Mikami *et al*., but incorporated a simpler cohesion model. Instead of the liquid-bridging model, they devised a cohesion model in which cohesive forces were only implemented when the particles are in physical contact. The magnitude of the cohesive force is set to a constant and equal to an integer multiple of the particle weight. In subsequent efforts, they observed that the transition from Geldart type B to type A behavior occurs at a cohesive force to weight ratio of approximately 1[16]. They have also found that the

transition form Geldart Type A behavior to Geldart Type C behavior occurred at a force ratio of approximately 47 [17]. More recently, Wang and Rhodes [34] developed new parameters to quantify the flowability of the fluidized bed. Using parameters such as the particle mobility and the average particle speed, they defined quantitative criteria for the transition from Geldart type A to type C particles.

Unlike the previous efforts which focus on liquid-bridging and general cohesion models, Xu *et al*. [35] implemented a model for van der Waals forces into a fluidized bed simulation. The results of this effort show the formation of static force chains within the fluidized bed. Kobayashi *et al*. [36] incorporated an adhesive force model into their simulation. The results from this effort indicate that the adhesion only affects the minimum fluidization curve for decreasing gas velocities, while the adhesive force has no effect for increasing gas velocities. Most recently, Ye *et al*. [37] incorporated van der Waals forces into a soft-sphere discrete particle fluidized bed model using the Hamaker theory. They observed the formation of channels reminiscent of Geldart type C behavior for high levels of cohesion. They also show that the minimum fluidization velocity was insensitive to changes in the level of cohesion. This finding is counter to findings of efforts that used liquid binders to apply cohesion in an experimental fluidized bed [38-41]. However, this discrepancy could be due the differences in liquid bridging forces and van der Waals forces. Ye *et al.* do not specify if their measurements were made using increasing or decreasing gas velocity (the relevance of which will be addressed in Section 7.2.3).

These previous efforts use various models for cohesion in fluidized-bed systems, and have produced results that agree with many experimental observations.

However, none of the cohesion models used in the aforementioned efforts involves impulsive interactions, as is needed for incorporation of cohesion into continuum (kinetic-theory) models. In the current effort, cohesion is incorporated using the square-well potential, which treats cohesion as an instantaneous event. For purposes of comparison, cohesive forces are also implemented using the more complex Hamaker model for van der Waals forces. A comparison of the results obtained with these two cohesion models will indicate the effectiveness of the simpler, square-well model relative to the more elaborate Hamaker model.

5.4 References

1. T. B. Anderson and R. Jackson, A fluid mechanical description of fluidized beds, *Industrial and Engineering Fundamentals* 6 (1967) 527.
2. D. Gidaspow, Y. P. Tsuo, and K. M. Luo, Computed and experimental cluster formation and velocity profiles in circulating fluidized beds, in Fluidization IV, J C Grace, L W Schemilt, and N A Bergougnou, Editors, 1989, Engineering Foundation: New York.
3. C. K. K. Lun, S. B. Savage, D. J. Jeffrey, and N. Chepurnity, Kinetic theories for granular flow: Inelastic particles in Couette flow and slightly inelastic particles in a general flow field, *Journal of Fluid Mechanics* 140 (223) (1984)
4. J. L. Sinclair and R. Jackson, Gas-particle flow in a vertical pipe with particle-particle interactions, *AIChE Journal* 35 (9) (1989) 1473.
5. C. Campbell, Rapid Granular Flows, *Annual Review of Fluid Mechanics* 22 (1990) 57.
6. I. Goldhirsch, Rapid granular flows, *Annual Review of Fluid Mechanics* 35 (2003) 267.
7. J. L. Sinclair, Hydrodynamic modeling, in Circulating Fluidized Beds, J R Grace, A A Auidan, and T M Knowlton, Editors, 1997, Chapman and Hall: Great Britain.
8. H. Enwald, E. Peirano, and A.-E. Almstedt, Eulerian two-phase flow theory applied to fluidization, *International Journal of Multiphase Flow* 22 (Suppl.) (1996) 21.
9. B. G. M. van Wachem and A. E. Almstedt, Methods for multiphase computational fluid dynamics, *Chemical Engineering Journal* 96 (2003) 81.
10. Y. Tsuji, T. Kawaguchi, and T. Tanaka, Discrete particle simulation of two-dimensional fluidized bed, *Powder Technology* 77 (1993) 79.
11. P. A. Cundall and O. D. Strack, A discrete numerical model for granular assemblies, *Geotechnique* 29 (1) (1979) 47-65.
12. D. Gera, M. Gautam, Y. Tsuji, T. Kawaguchi, and Y. Tanaka, Computer simulation of bubbles in large-particle fluidized beds, *Powder Technology* 98 (1998) 38.
13. S. Limtrakul, A. Chalermwattanatai, K. Unggerawirote, Y. Tsuji, T. Kawaguchi, and W. Tanthapanichakoon, Discrete particle simulations of solids motion in a gas-solid fluidized bed, *Chemical Engineering Science* 58 (2003) 915.
14. M. J. Rhodes, X. S. Wang, M. Nguyen, P. Stewart, and K. Liffman, Study of mixing in gas-fluidized bed using a DEM model, *Chemical Engineering Science* 56 (2001) 2859.
15. M. J. Rhodes and X. S. Wang, The role of interparticle force in determining geldart group behavior: a DEM study, *2000 AIChE Annual Meeting* (2000)

16. M. J. Rhodes, X. S. Wang, M. Nguyen, P. Stewart, and K. Liffman, Use of discrete element method simulation in studying fluidization characteristics: influence of interparticle force, *Chemical Engineering Science* 56 (2001) 69-76.
17. M. J. Rhodes, X. S. Wang, M. Nguyen, P. Stewart, and K Liffman, Onset of cohesive behavior in gas fluidized beds: a numerical study using DEM simulation, *Chemical Engineering Science* 56 (2001) 4433-4438.
18. T. Mikami, H. Kamiya, and M. Horio, Numerical simulation of cohesive powder behavior in a fluidized bed, *Chemical Engineering Science* 53 (10) (1998) 1927.
19. B. H. Xu and A. B. Yu, Numerical simulation of the gas-solid flow in a fluidized bed by combining discrete particle method with computational fluid dynamics, *Chemical Engineering Science* 52 (16) (1997) 2785-2809.
20. T. Kawaguchi, T. Tanaka, and Y. Tsuji, Numerical simulation of two-dimensional fluidized beds using the discrete element method (comparison between two- and three-dimensional models), *Powder Technology* 96 (1998) 129.
21. A. D. Renzo and F. P. D. Maio, Comparison of contact-force models for simulation of collisions in DEM-based granular flow codes, *Chemical Engineering Science* 59 (2004) 525.
22. B. H. Xu, A. B. Yu, S. J. Chew, and P. Zulli, Numerical simulation of gas-solid flow in a bed with lateral gas blasting, *Powder Technology* 109 (2000) 13.
23. B. P. B. Hoomans, J. A. M. Kuipers, W. J. Briels, and W. P. M. V. Swaaij, Discrete particle simulation of bubble and slug formation in a two-dimensional gas-fluidised bed: a hard-sphere approach, *Chemical Engineering Science* 51 (1) (1996) 99.
24. B. P. B. Hoomans, J. A. M. Kuipers, and W. P. M. v. Swaaij, Granular dynamics simulation of segregation phenomena in bubbling gas-fluidized beds, *Powder Technology* 109 (2000) 41.
25. J. Ouyang and J. Li, Particle-motion-resolved discrete model for simulating gas-solid fluidization, *Chemical Engineering Science* 54 (1999) 2077.
26. S. Yuu, T. Umekage, and Y. Johno, Numerical simulation of air and particle motions in bubbling fluidized bed of small particles, *Powder Technology* 110 (2000) 158.
27. B. G. M. van Wachem, J. van der Schaaf, J. C. Schouten, R. Krishna, C. M. van den Bleek, Experimental validation of Lagrangian-Eulerian simulations of fluidized beds, *Powder Technology* 116 (2001) 155-165.
28. E. Helland, R. Occelli, and L. Tadrist, Numerical study of cluster formation in a gas-particle circulating fluidized bed, *Powder Technology* 110 (2000) 210.
29. J. Li, Kuipers, J.A.M., Effect of pressure on gas-solid flow behavior in dense gas-fluidized beds: a discrete particle simlation study, *Powder Technology* 127 (2002) 173.
30. H. Zhou, G. Flamant, D. Gauthier, and Y. Flitiris, Simulation of coal combustion in a bubbling fluidized bed by distinct element method, *Chemical Engineering Research and Design* 81 (A9) (2003) 1144.
31. M. J. V. Goldschmidt, G. G. C. Weijers, R. Boerefijn, and J. A. M. Kuipers, Discrete element modelling of fluidised bed spray granulation, *Powder Technology* 138 (2003) 39.
32. T. McKeen and T. Pugsley, Simulation and experimental validation of a freely bubbling bed of FCC catalyst, *Powder Technology* 129 (2003) 139.
33. K. Kuwagi, T. Mikami, and M. Horio, Numerical simulation of metallic solid bridging particles in a fluidized bed at high temperature, *Powder Technology* 109 (2000) 27.
34. X. S. Wang and M. J. Rhodes, Mechanistic study of defluidization by numerical simulation, *Chemical Engineering Science* 59 (2004) 215.
35. B. H. Xu, Y. C. Zhou, A. B. Yu, and P. Zulli, Force structures in gas fluidized beds of fine powders, *World Congress on Particle Technology 4, Sydney, Australia* (2002)
36. T. Kobayashi, T. Mukai, T. Kawaguchi, T. Tanaka, and Y. Tsuji, DEM analysis of flow patterns of Geldart's group A particles in fluidized bed, *World Congress on Particle Technology 4, Sydney, Australia* (2003)
37. M. Ye, M. A. v. d. Hoef, and J. A. M. Kuipers, A numerical study of fluidization behavior of Geldart A particles using a discrete particle model, *Powder Technology* 139 (2004) 129.
38. P. C. Wright and J. A. Raper, Role of liquid bridge forces in cohesive fluidization, *Transactions of the Institution of Chemical Engineers* 76 (1998) 753.
39. P. C. Wright and J. A. Raper, Examination of dispersed liquid-phase three-phase fluidized beds: Part 1 Non-porous, uniform particle systems, *Powder Technology* 97 (1998) 208.

40. M. L. Passos and A. S. Mujumdar, Effect of cohesive forces on fluidized and spouted beds of wet particles, *Powder Technology* 110 (2000) 222.
41. J. P. K. Seville and R. Clift, The effect of thin liquid layers on fluidization characteristics, *Powder Technology* 37 (1984) 117.

Chapter 6. Fluidized Bed Simulation Description

The MFIX (Multiphase Flow with Interphase eXchanges) program developed at the Department of Energy National Energy Technology Laboratory (DOE NETL) was used as a framework to model the gas-fluid system in this work (www.mfix.org). The MFIX software was originally designed to model multiphase systems in an Eulerian-Eulerian framework, in which the fluid phase and solid phase(s) are treated as interpenetrating continua and solved via a finite-volume technique.

Recently, the capabilities of MFIX have been extended such that Eulerian-Lagrangian models are also included, in which the solid phase(s) is described using a discrete-particle model [1]. As part of this project, the discrete-particle simulation has been modified to include cohesive interactions.

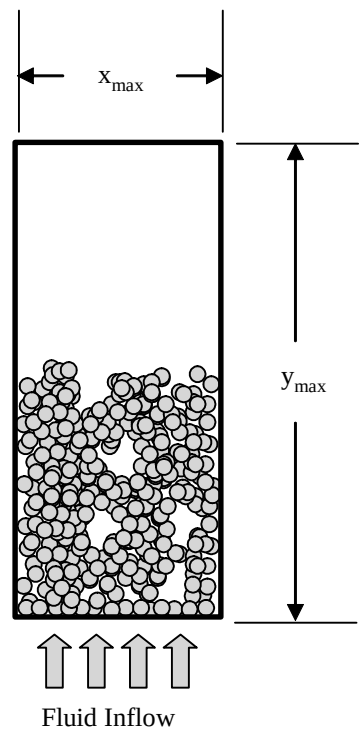

Fig. 6.1 *Fluidized bed simulation domain.*

The next few sections include a description of the details of the fluid-phase simulation, solid-phase simulation, cohesive models, and the methods used to verify and validate the resulting cohesive fluidized bed simulation. The system being simulated is a two-dimensional fluidized bed of monodisperse particles as shown in Figure 6.1.

6.1 Gas-Phase Model

6.1.1 Governing Equations

The fluid phase is modeled by solving a locally-averaged mass and momentum balance. The continuity equation is given by:

$$\frac{\partial}{\partial t}\left(\varepsilon_g \rho_g\right) + \nabla \cdot \left(\varepsilon_g \rho_g \vec{v}_g\right) = 0 \tag{6.1}$$

where ε_g is the void fraction ρ_g is the gas density and $\vec{v}_g$ is the gas velocity [2]. The first term in equation 6.1 represents the accumulation of mass per unit volume and the second term represents the convective flux of mass per unit volume. The momentum balance is given by

$$\frac{\partial}{\partial t}\left(\varepsilon_g \rho_g \vec{v}_g\right) + \nabla \cdot \left(\varepsilon_g \rho_g \vec{v}_g \vec{v}_g\right) = \nabla \cdot \overline{\overline{S}}_g + \varepsilon_g \rho_g \vec{g} - \vec{I}_{gs} \tag{6.2}$$

where $\overline{\overline{S}}_g$ is the gas-phase stress tensor, $\vec{g}$ is the acceleration due to gravity, and $\vec{I}_{gs}$ is the rate of momentum transfer between the gas and solid phase per unit volume. On the left-hand side of equation 6.2, the first term refers to the rate of increase of momentum per unit volume and the second term refers to the rate of momentum gain by convection per unit volume. On the right-hand side, the first term describes the rate of momentum transfer by shear and normal stress components per unit volume. The second term incorporates the net gravitational force on the fluid per unit volume. The last term on the right side represents the interaction force between the fluid and solid phases per unit volume [2, 3].

The gas-solid momentum transfer is described by:

$$\vec{I}_{gs} = -\varepsilon_s \nabla P_g - F_{gs}\left(\vec{v}_s - \vec{v}_g\right) \tag{6.3}$$

where P_g is the gas-phase pressure, ε_s is the solids volume fraction and $\vec{v}_s$ is the average solids velocity. The calculation of the average solids velocity will be discussed in more detail in Section 6.2. The drag coefficient, F_{gs}, is determined using the expression developed by Syamlal and O'Brien [4]:

$$F_{gs} = \frac{3\varepsilon_s \varepsilon_g \rho_g}{4V_t^2 d_p} C_{Ds} \left| \vec{v}_s - \vec{v}_g \right| \tag{6.4}$$

where ε_s is the solids volume fraction and d_p is the particle diameter. The other undefined quantity in equation 6.3 is the single-sphere drag coefficient, C_{Ds}. For this quantity, MFIX uses the formula given by Dalla Valle [5]:

$$C_{Ds} = \left(0.63 + 4.8\sqrt{\frac{V_t}{Re}} \right)^2 \tag{6.5}$$

The terminal velocity, V_t, is given by the following correlation developed by Garside and Al-Dibouni [6]:

$$V_t = 0.5\left(A - 0.06\,Re + \sqrt{(0.06\,Re)^2 + 0.12\,Re(2B - A) + A^2} \right) \tag{6.6}$$

where

$$A = \varepsilon_g^{4.14} \tag{6.7}$$

$$B = \begin{cases} 0.8\varepsilon_g^{1.28} & \varepsilon_g \le 0.85 \\ \varepsilon_g^{2.65} & \varepsilon_g > 0.85 \end{cases} \tag{6.8}$$

The Reynolds number, *Re*, is defined as

$$Re = \frac{d_p \left| \vec{v}_s - \vec{v}_g \right| \rho_g}{\mu_g} \tag{6.9}$$

where μ_g is the gas viscosity.

These equations are solved numerically for the fluidized bed system using a modified version of the SIMPLE method developed by Patankar [7]. For more details on the solution of the gas-phase equations, the reader is referred to the MFIX Numerical Theory Guide [8].

6.1.2 Boundary/Initial Conditions

The fluid simulation domain consists of a two-dimensional rectangular system with the origin of the *x*- and *y*- axis in the bottom left corner, as shown in Figure 6.2. The bed typically used is 8 cm wide by 20 cm tall. For this length and width, 27 computational cells in the *x*-direction and 30 computational cells in the *y*-direction are used. In the following text, any changes from this bed size are noted.

For purposes of specifying the initial conditions, the bed is divided into a "bed" section and a "freeboard" section with the former taking up the bottom half of the bed and the latter comprising the top half. In the bed section, the void fraction is initially set to 0.42, which is a typical value at minimum fluidization. The gas velocity is initially set to 80 cm/s in the *y*-direction. In the freeboard section the void fraction is initially set to unity and the *y*-component of the gas velocity is initially set to 100 cm/s. In order to produce fluidization curves, most simulations are run with inlet conditions that vary with time and the initial conditions have essentially no effect on these results.

The boundary conditions for the gas phase consist of no-slip, impermeable walls on the vertical sides of the bed. For the outflow boundary condition at the top

of the bed, zero gauge pressure is specified across the entire width. Thirteen separate inlet jets are used to specify the inlet boundary conditions. The boundaries of each inlet jet are required to coincide with the boundary of a computational cell, limiting the range of sizes that can be used for the inlet jets. In most cases, each jet consists of one computational cell (2.96 x 10^{-4} m in width). At each inlet jet, the void fraction is set to unity and the gas velocity is set to achieve the desired superficial velocity in the bed. This inlet jet configuration provides the most uniform fluidization with the least amount of dead space (unfluidized particles) in the bed. Between each jet, the distributor plate is represented by impermeable, no-slip walls.

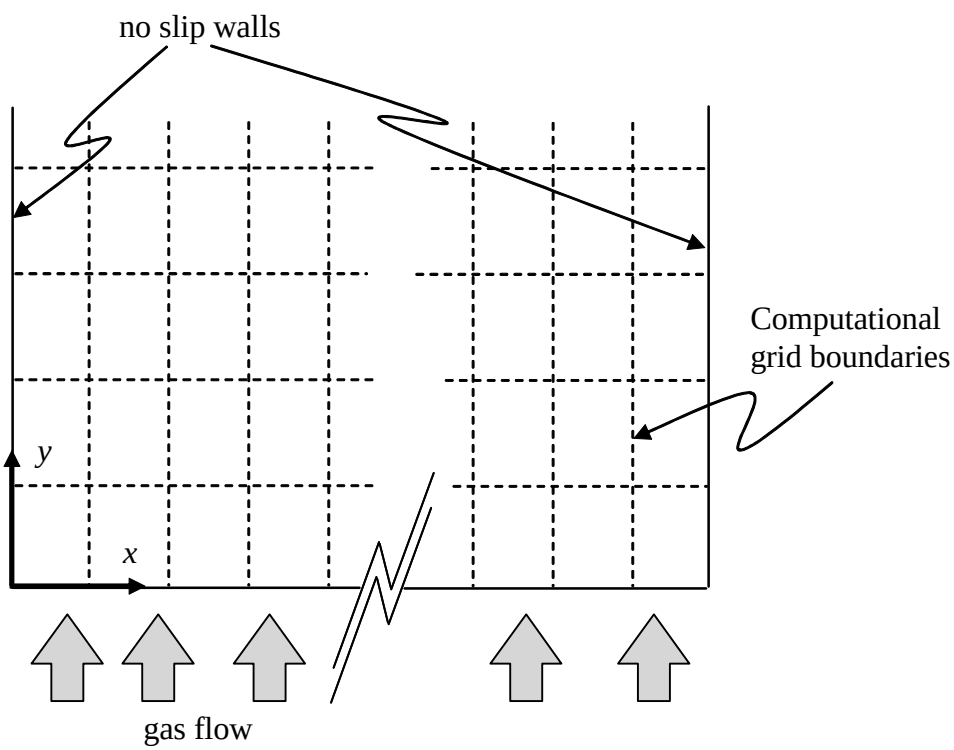

Fig. 6.2 *Computational simulation domain.*

MFIX uses a staggered grid system in which scalars (e.g. pressure, void fraction, solids fraction) are calculated at the center of each computational cell and

the components of the velocity vectors are calculated at the faces of each computational cell. Therefore, the pressure drop across the entire bed pressure is actually based on the difference between the specified zero pressure at the outlet and the pressure just above the inlet as illustrated in Figure 6.3. The pressure drop associated with half of a computational cell is excluded from the overall pressure drop prediction. The ramifications of this numerical treatment will be discussed in Section 6.4.2.2.

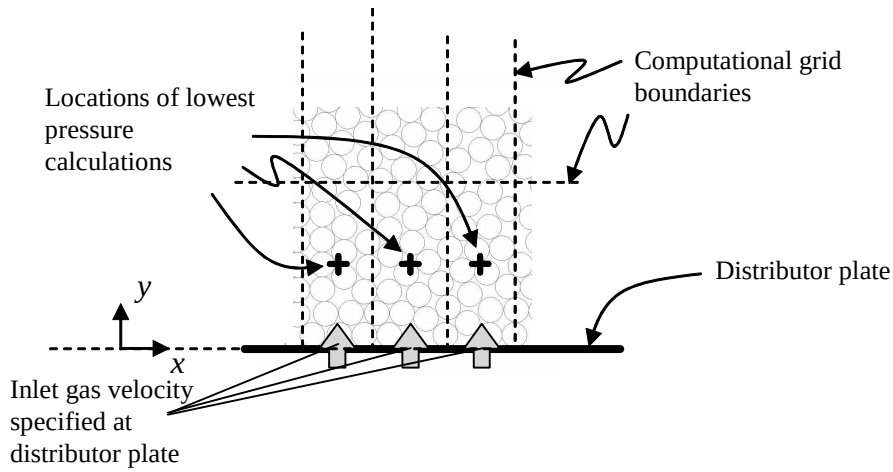

Fig 6.3 *Inlet boundary conditions.*

6.2 Solid-Phase Simulation

Unlike the gas phase, the solid phase is treated as discrete entities. Specifically, momentum (force) balances are applied to individual particles. The following sections describe the details of the discrete-particle treatment.

6.2.1 Particle Advancement

The discrete-particle simulation operates using a time-stepped algorithm [9]. The particles are modeled as spheres confined to movement in the *x*- and *y*- directions

only (i.e., two-dimensional motion). Equations of linear motion are used to determine the distance that each particle moves within a given time step:

$$\Delta x_i = v_{x,i} \Delta t_s \tag{6.10a}$$

$$\Delta y_i = v_{y,i} \Delta t_s \tag{6.10b}$$

where Δx_i and Δy_i are the distances moved by the ith particle in the *x*- and *y*-directions, respectively, within the time step, Δt_s, and the speeds of the ith particle in the *x*- and *y*- directions are $v_{x,i}$ and $v_{y,i}$, respectively.

The velocity change of each particle within a given time step is determined from the acceleration ($\vec{a}_i$) as follows:

$$\Delta \vec{v}_i = \vec{a}_i \Delta t_s \tag{6.11}$$

The acceleration is determined using the Newtonian equation of motion

$$\vec{a}_i = \frac{\vec{F}_i}{m_i} \tag{6.12}$$

where the net force on every particle ($\vec{F}_i$) is a sum of the forces from repulsive collisional contacts with other particles and the walls ($\vec{F}_{coll,i}$); cohesive contacts with other particles and the walls ($\vec{F}_{coh,i}$); gravitational forces ($\vec{F}_{g,i}$) and forces induced by the fluid ($\vec{F}_{f,i}$):

$$\vec{F}_i = \vec{F}_{coll,i} + \vec{F}_{coh,i} + \vec{F}_{g,i} + \vec{F}_{f,i} \tag{6.13}$$

Section 6.2.2 contains a discussion of the spring-and-dashpot model, which is used to determine the forces arising from particle contacts ($\vec{F}_{coll,i}$). The fluid forces ($\vec{F}_{f,i}$) will be detailed in Section 6.2.3, while the calculation of cohesive forces will be

discussed in Section 6.2.4 ($\vec{F}_{coh,i}$). Gravitational forces ($\vec{F}_{g,i}$) are simply the product of the mass the gravitational constant.

6.2.2 Linear-Spring-and-Dashpot Model

At each time step, the total collisional force on a given particle is equal to the sum of all the collisional forces imposed on it at that time step:

$$\vec{F}_{coll,i} = \sum_{i=1}^{n_{col,i}} \vec{F}_{coll,ij} \tag{6.14}$$

where $n_{col,i}$ is the total number of contacts between the ith particle and other particles and/or walls at the given time step, and $\vec{F}_{coll,ij}$ is the collisional force on the ith particle due to contact with the jth particle (or wall). For particle-particle contacts, the collisional force imposed on the ith particle from the jth particle is equal in magnitude but opposite in direction from the collisional force imposed on the jth particle by the ith particle ($\vec{F}_{coll,ij} = -\vec{F}_{coll,ji}$).

The discrete-particle model used here is a soft-sphere model. Particle overlap is used to identify the occurrence of collisions and to calculate the magnitude of the repulsive force generated by the collision. During each collision, a normal and a tangential component of the contact force is experienced by each particle:

$$\vec{F}_{coll,ij} = F_{n,ij}\vec{k}_{n,ij} + F_{t,ij}\vec{k}_{t,ij} \tag{6.15}$$

where $F_{n,ij}$ is the normal component, and $F_{t,ij}$ is the tangential component of the contact force on particle i due to contact with particle j. The normal vector pointing

from the center of the ith particle to the center of the jth particle is given by $\vec{k}_{n,ij}$. The unit vector tangent to the plane of contact is given by $\vec{k}_{t,ij}$.

6.2.2.1 Normal contacts

The normal component of the repulsive force between colliding particles *i* and *j* is based on the linear-spring-and-dashpot model:

$$F_{n,ij} = -\delta_{n,ij} K_n + \eta_n \frac{\partial \delta_{n,ij}}{\partial t} \tag{6.16}$$

where $\delta_{n,ij}$ is the normal component of the overlap between particles *i* and *j*, $v_{n,ij}$ is the normal component of the relative velocity, K_n is the normal spring constant which characterizes the stiffness of the particles, and η_n is the normal damping coefficient which controls the amount of kinetic energy dissipated during the collision. This model is illustrated in Figure 6.4. The normal overlap can be calculated as the difference between the sum of the particle radii ($2r_{inner}$) and the distance between particle centers:

$$\delta_{n,ij} = 2r_{inner} - \sqrt{(x_i - x_j)^2 + (y_i - y_j)^2} \tag{6.17}$$

where x_i and y_i are the *x*- and *y*- components of the position of the ith particle, and x_j and y_j are the *x*- and *y*- components of the position of the jth particle. The normal component of the relative velocity is the dot product of the relative velocity ($\vec{v}_{ij}$) and the normal unit vector ($\vec{k}_{n,ij}$) as follows:

$$v_{n,ij} = \vec{v}_{ij} \cdot \vec{k}_{n,ij} \tag{6.18}$$

where

$$\vec{v}_{ij} = \vec{v}_i - \vec{v}_j \tag{6.19}$$

Particle-wall collisions are also resolved using the same equations (6.16-6.19), with minor modifications. Specifically, the wall velocity is always zero and the wall position used to calculate the overlap (equation 6.17) is adjusted to place the wall position one radius within the actual wall position. Furthermore, the normal unit vector ($\vec{k}_{n,ij}$) is always perpendicular to the wall and the tangential unit vector ($k_{t,ij}$) is parallel to the wall

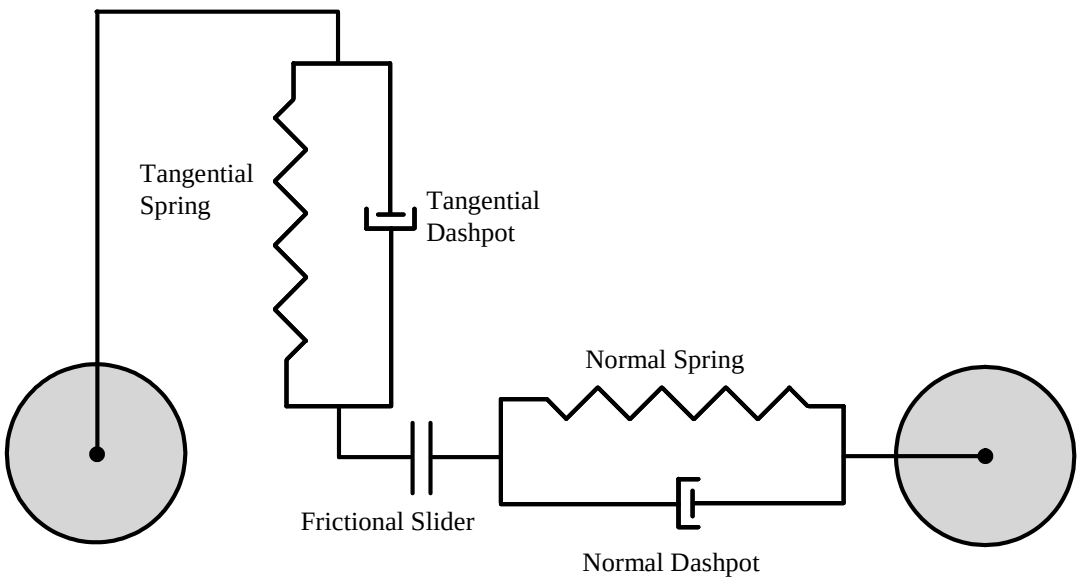

Fig. 6.4 *Linear-spring and dashpot model.*

6.2.2.2 Oblique Contacts

Tangential interactions are calculated as either *sticking* or *sliding* contacts based on the following inequality:

$$\left|F_{t,ij}\right| \le \mu \left|F_{n,ij}\right| \tag{6.20}$$

where μ is the coefficient of friction. If this inequality is not satisfied, then the particles undergo a sliding contact and the tangential component of the collision force is calculated as:

$$F_{t,ij} = \mu F_{n,ij} \tag{6.21}$$

If the inequality is satisfied, then the tangential component of the sticking contact force is calculated as follows:

$$F_{t,ij} = -\delta_{t,ij} K_t - \eta_t v_{t,ij} \tag{6.22}$$

where K_t is the tangential spring constant and η_t is the tangential damping coefficient. In this expression, $\vec{v}_{t,ij}$ is the tangential slip velocity between the two particles:

$$v_{t,ij} = \vec{v}_{ij} \cdot \vec{k}_{t,ij} + r_{inner}\left(\omega_i + \omega_j\right) \tag{6.23}$$

where ω_i and ω_j are the rotation rates of the ith and j^{th} particles, respectively, and r_{inner} is the particle radius. Also, $\vec{\delta}_{t,ij}$ is the tangential overlap, defined as follows:

$$\delta_{t,ij} = \Delta t_s \cdot v_{t,ij} \tag{6.24}$$

As with the calculation of the normal component of the collision force, the tangential component of the collision force for particle-wall contact uses the same equations presented here for particle-particle collisions with minor modifications. In particular, the wall velocity is zero in both directions and the rotation rate of the wall is also set to zero.

6.2.2.3 Determination of Spring and Dashpot Parameters

The linear-spring-and-dashpot model is a simplified description of the contact mechanics that occur during a particle collision. The following sections contain a description of the important issues involved with the selection of values for the spring constant and dashpot coefficient.

6.2.2.3.1 Determination of K_n and η_n via Collision Experiments

The normal spring constant (K_n) and dashpot coefficient (η_n) are model inputs that cannot be directly measured directly. However, these values can be chosen such that they produce collision outcomes similar to those measured experimentally. More specifically, the coefficient of restitution and collision duration can be used to set the linear-spring and dashpot parameters. A mapping between the experimentally-measured quantities and the spring and dashpot parameters is possible by analyzing the equation of motion for two colliding spheres (see Appendix B). This treatment results in the following expression for the coefficient of restitution (e) and the collision duration (t_c):

$$e = exp\left[\frac{-\alpha\omega_o\pi}{q}\right] \tag{6.25}$$

$$t_c = \frac{\pi}{q} \tag{6.26}$$

where the intermediate variables are defined as follows:

$$\omega_o = \sqrt{2K_n / m} \tag{6.27}$$

$$\alpha = \frac{\eta_n}{\sqrt{2mK_n}} \tag{6.28}$$

$$q = \omega_o \sqrt{1-\alpha^2} \tag{6.29}$$

By targeting a specific coefficient of restitution and collision duration, the spring and dashpot parameters can be chosen to obtain the desired values. The coefficient of restitution has been measured experimentally in many studies [10-14], and thus provides a good benchmark for the determination of a realistic spring and dashpot parameters. However, data for the collision time is extremely limited. These considerations have led many researchers to choose the spring and dashpot parameters based on the matching of the restitution coefficient and on numerical considerations rather than the matching of the restitution coefficient *and* collision duration [15]. These numerical considerations are covered in the following section.

6.2.2.3.2 Numerical Stability and Accuracy

As the spring constant gets larger (i.e., the spring gets stiffer), the duration of a given collision decreases, and hence the time step must be smaller in order to avoid numerical inaccuracies and instability. Several previous works have given the following expression for the critical time step:

$$\Delta t_{cr} = C_1 \left(m / K_n \right)^{1/2} \tag{6.30}$$

where C_1 is a constant that is on the order of 10 (though slightly different values have been reported) [15-17]. In general, these considerations put an upper limit on the magnitude of the time step for a given spring constant. Note that a smaller time step leads to longer computational times for a given simulation.

To reduce computational times, the spring constant is often made artificially soft [15, 17-19], thereby resulting in a collision duration that is unrealistically long.

(The damping coefficient is still set, though, to achieve a realistic coefficient of restitution.) Several researchers [15, 18, 20] have indicated that the use of an artificially small spring constant does not have a significant effect on the nature of the flow in fluidized bed simulations. The parameters used in previous simulations of fluidized beds, and specifically those that utilize a linear-spring-and-dashpot model, are reviewed in the next section.

6.2.2.3.3 Parameters Used in Previous and Current Efforts

Table 6.1 contains the input values used by previous researchers for the contact model: spring constant, dashpot coefficient, friction coefficient (μ), and particle phase time step (Δt_s). All of the efforts listed in Table 6.1 used a linear-spring-and-dashpot model to simulate a fluidized-bed system. Also given are the corresponding values for the restitution coefficient and collision duration (see equations 6.25 and 6.26). (Italicized values for the damping coefficient and collision duration were not provided by the authors, but instead calculated using given values along with equations 6.25 or 6.26, or equations provided by the authors.) Many efforts have based their system on the seminal work by Tsuji *et al*. As mentioned in Section 5.2, Xu and Yu [21] have noted that the spring constant used by Tsuji *et al.* was made artificially small to reduce computational time leading to particles that are unrealistically soft.

Up to this point, only the spring and dashpot parameters associated with the normal direction have been considered. The determination of the tangential spring and dashpot parameters has been given very little attention in the literature. In the

work of Yuu *et al*. [22] a Hertzian contact model was used and they assumed that the tangential spring constant was 2-5 times smaller than the normal counterpart based on the argument that normal elastic modulus is about 2-5 times larger than the shear modulus for most materials. However, the majority of efforts have simply assumed that the normal and tangential values are the same for the spring constant and coefficient of dissipation [15, 17, 19, 20].

Table 6.1. *Linear spring and dashpot parameters used in previous efforts*

effort	year	K_n (kg/s^2)	η_n (kg/s)	Δt_s	e	t_c (sec)	μ
Tsuji, et al.	1993	800	0.0180	2.0×10^{-4}	0.9	1.06×10^{-3}	0.3
Xu and Yu	1997	50000	0.15	1.5×10^{-5}	0.9	1.34×10^{-5}	0.3
Gera, et al.	1998	800	0.012	2.0×10^{-4}	0.9	7.47×10^{-4}	0.3
Kawaguchi, et al.	1998	800	0.012	2.0×10^{-4}	0.9	7.47×10^{-4}	0.1-0.3
Mikami, et al.	1998	800	0.0016	2.58×10^{-5}	0.9	9.26×10^{-5}	0.3
Xu, et al.	2000	40000	0.12	2.0×10^{-5}	0.9	1.42×10^{-4}	n.s.
Kuwagi, et al.	2000	800	8.26×10^{-6}	1.0×10^{-6}	0.9	1.42×10^{-5}	inf.
Rhodes, et al.	2001	800	0.0016	not. spec.	0.9	9.26×10^{-5}	0.3
Xu., et al.	2002	50	1.65×10^{-5}	not. spec.	0.9	8.64×10^{-6}	0.3
Limtrakul, et al.	2003	800	0.022	not. spec.	0.9	1.32×10^{-3}	0.3
Ye, et al.	2004	7	2.7×10^{-6}	4.2×10^{-6}	0.9	1.82×10^{-5}	0.3

The coefficient of friction is one parameter that can be measured directly in experiments [23]. Most efforts have used a value near 0.3 (Table 6.1), and this value is also used in the current effort. With regard to particle-wall contacts, all the efforts listed in Table 6.1 use the same spring and dashpot parameters for both particle-particle and particle-wall contacts. The same approach is taken for most simulations in this effort, unless otherwise noted. Table 6.2 presents the parameters employed in all of the simulations for this study, unless otherwise noted. Limited experimental results [10, 24, 25] indicate the realistic particle collision times are on the order of 100 microseconds. In order to achieve collision times of this order of magnitude, a spring constant of approximately 8000 N/m^2 would be necessary. The particles used

in this study were made softer in the interest of computational time. Nonetheless, the results of the softened particles were also spot-checked against simulations using spring constants that led to more realistic collision times to ensure that physical accuracy was not compromised. The spring constant does have a slight effect on the calculated minimum fluidization velocity, but the pressure drop at fluidization is not affected. These results are presented in Appendix E.

Table 6.2 *Soft-sphere parameters used in fluidized bed simulation.*

Parameter	Value
number of particles *(n)*	4000
fluidized bed width (x_{max}) (m)	0.08
fluidized bed height (y_{max}) (m)	0.2
computational cells in x-direction (m_{max})	27
computational cells in y-direction (n_{max})	30
Solid phase time step (Δt_s) (s)	2.25×10^{-5}
Particle diameter (D_P) (m)	0.001
Particle density (ρ_s) (kg/m^3)	2650
Normal spring constant (K_n) (kg/s^2)	800
Tangential spring constant (K_t) (kg/s^2)	800
Normal damping coefficient (η_n) (kg/s)	0.79×10^{-3}
Tangential damping coefficient (η_t) (kg/s)	0.79×10^{-3}
Friction coefficient (μ)	0.3
Coefficient of restitution *(e)*	*0.94*
Collision duration (t_c) (s)	9.25×10^{-5}
Normal wall spring constant $(K_{n\text{-}wall})$ (kg/s^2)	800
Tangential wall spring constant $(K_{t\text{-}wall})$ (kg/s^2)	800
Normal wall damping coefficient $(\eta_{n\text{-}wall})$ (kg/s)	0.79×10^{-3}
Tangential wall damping coefficient $(\eta_{t\text{-}wall})$ (kg/s)	0.79×10^{-3}
Wall friction coefficient (μ_{wall})	0.3

An initial goal of this work was to reproduce the results of Rhodes *et al*., so the default parameters in Table 6.2 closely mimic the conditions in that effort. The conditions listed in Table 6.2 can be considered the default for all the results presented. For those cases in which the values of input parameters were changed, a special note is made in the text. The values for e and t_c were not specified explicitly,

but calculated based on the explicitly-set parameters using equations 6.25 and 6.26 respectively.

6.2.3 Calculation of Fluid Force on Particles

The force exerted by the gas on the particles consists of a drag force ($\vec{F}_{d,i}$) and a pressure contribution ($\vec{F}_{p,i}$) as follows:

$$\vec{F}_{f,i} = \vec{F}_{p,i} + \vec{F}_{d,i} \tag{6.31}$$

The pressure force is given by:

$$\vec{F}_{p,i} = (\vec{\nabla} P)\forall_i \tag{6.32}$$

where $\forall_i$ is the volume of the ith particle. The drag force on each particle is calculated using the drag coefficient (F_{gs}) defined in equation 6.4. For each particle, the drag force is given by

$$\vec{F}_{d,i} = \frac{F_{gs}(\vec{v}_{s,mn} - \vec{v}_{g,mn})}{\varepsilon_{s,mn}}\forall_i \tag{6.33}$$

where $\vec{v}_{s,mn}$ is the average solid velocity, $\vec{v}_{g,mn}$ is the average gas velocity and $\varepsilon_{s,mn}$ is the solid volume fraction. Here, *m* and *n* represent the indices of the computational cell in the *x*- and *y*- direction respectively. The methods used to calculate these quantities will be described in Section 6.3.1.

6.2.4 Cohesive Interactions

Two different cohesion models are applied to the fluidized-bed simulation in this work, namely a square-well model and a Hamaker model for van der Waals

forces. Just as with contact forces, particles are allowed to have multiple cohesive interactions in a single (particle-phase) time step. A qualitative description of these models has already been presented in Chapter 1; the following sections will outline the mathematical implementation of these models in this fluidized bed simulation.

6.2.4.1 Hamaker Model for van der Waals Forces

The Hamaker theory is used to estimate the van der Waals force between two equal-sized, spherical particles according to the following equation [26]:

$$F_{vdW} = \frac{A r_{inner}}{12 H^2} \tag{6.34}$$

where r_{inner} is the particle radius; A is the Hamaker constant, which is specific to a given material and has typical values on the order of 10^{-20} J; and H is the minimum surface-to-surface separation distance between two particles *i* and *j*:

$$H = \sqrt{(x_i - x_j)^2 + (y_i - y_j)^2} - 2r_{inner} \tag{6.35}$$

The corresponding cohesive force between a spherical particle and a flat wall is [26]:

$$F_{vdW,wall} = \frac{A r_{inner}}{6 H^2} \tag{6.36}$$

For both of these expressions, the cohesive force approaches infinity as the separation distance approaches zero. This singularity incurred at particle contact is avoided by introducing a "cutoff" distance, H_{cut}. For separation distances below this cutoff distance, the interparticle cohesive force is given by a surface adhesion force (F_{ad}) model [27].

$$F_{ad} = 2\pi r_{inner} \gamma \tag{6.37}$$

where γ is a constant surface energy per unit area which is calculated based on the specified Hamaker constant to make the Hamaker force continuous at the cutoff distance. Thus, the cohesive force is maintained at a constant value for any separation distances (based on equation 6.38) below the minimum cutoff distance, which includes any "negative" separation distances that occur during actual particle contact. For this work, a minimum cutoff distance of 4×10^{-10} m was used. This value is based on the average interatomic distance for many common solids [27]. This treatment is depicted graphically in Figure 6.5 along with the square-well model, as described below.

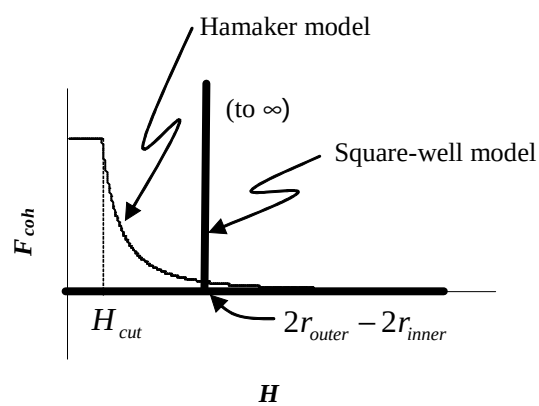

Fig. 6.5 *Forces implemented by cohesion models.*

6.2.4.2 Square-well Model

The implementation of the square-well potential in the fluidized bed system is similar to that of the granular flow system described in Chapter 3. The main modification incorporated into the fluidized-bed system is the addition of particle-wall contacts. These interactions are modeled like particle-particle contacts except that the wall is assigned an infinite mass. Furthermore, to account for the additional

attractive force resulting from the interaction of a plane with a sphere rather than between two spheres, the well depth is doubled in all particle-wall interactions. The doubled cohesive-well depth at the wall is consistent with the Hamaker model of van der Waals forces in which the cohesive force between a sphere and a plane is twice that of the force between two spheres (see equations 6.34 and 6.36).

To identify cohesive interactions in the context of the soft-sphere algorithm, particles are checked for square well width overlap (r_{outer}) at each time step. Once a square-well overlap is detected, an approaching cohesive interaction is implemented at that time step (equation 3.7). For each particle, a list of overlapped particles is kept so that once a particle leaves the square-well, an escaping-cohesive or capture-cohesive interaction can be implemented in the form of a cohesive force (equations 3.9 and 3.11, respectively) at that time step. This method differs from the predictive (event-driven) method used in the granular flow simulation since the square-well cohesive interactions are not implemented at the exact outer edge of square well. The exact separation distance at which interactions are implemented is determined by the end of the time step. However, the time step is set small enough that the extra distance traveled by the particles is typically an order of magnitude smaller than the distance between the particle surface and the outer edge of the square well.

6.2.5 Initial Conditions

To start the simulation, particles are given random initial positions and velocities. Replicates were obtained by using a different random number seed which

resulted in slightly altered initial positions and velocities. These replicates were used to quantify the error associated with the simulated results.

6.3 Coupling of the Gas and Solid Phases

Advancement in time of both phases is accomplished via a time-stepped algorithm. Because the inherent time scales of each phase are different, the solution proceeds with two different time steps, namely Δt_f for the fluid phase and Δt_s for the solid phase. In most simulations, the time step for the gas phase is 20 times larger than the time step for the particle phase. Because the gas phase uses a larger time step, the discrete-particle simulation goes through several iterations for each single time the gas-phase equations are solved. A flowchart of this computational algorithm is shown in Figure 6.6. The gas-phase quantities (i.e., gas velocity and pressure) required for the solution of the particle force balance remain constant over these iterations. Once the discrete-particle simulation has completed enough iterations to equal the elapsed time for the fluid-phase calculation, the fluid phase equations are solved again and the cycle repeats. This process continues until the simulation reaches the specified stop time.

6.3.1 Calculation of Void Fraction and Average Particle Velocity

Although the gas-phase simulation is only two-dimensional, the simulation domain is assumed to have a depth of one particle diameter for the purposes of calculating the void fraction [17, 18, 21, 28, 29]. In each computational cell the

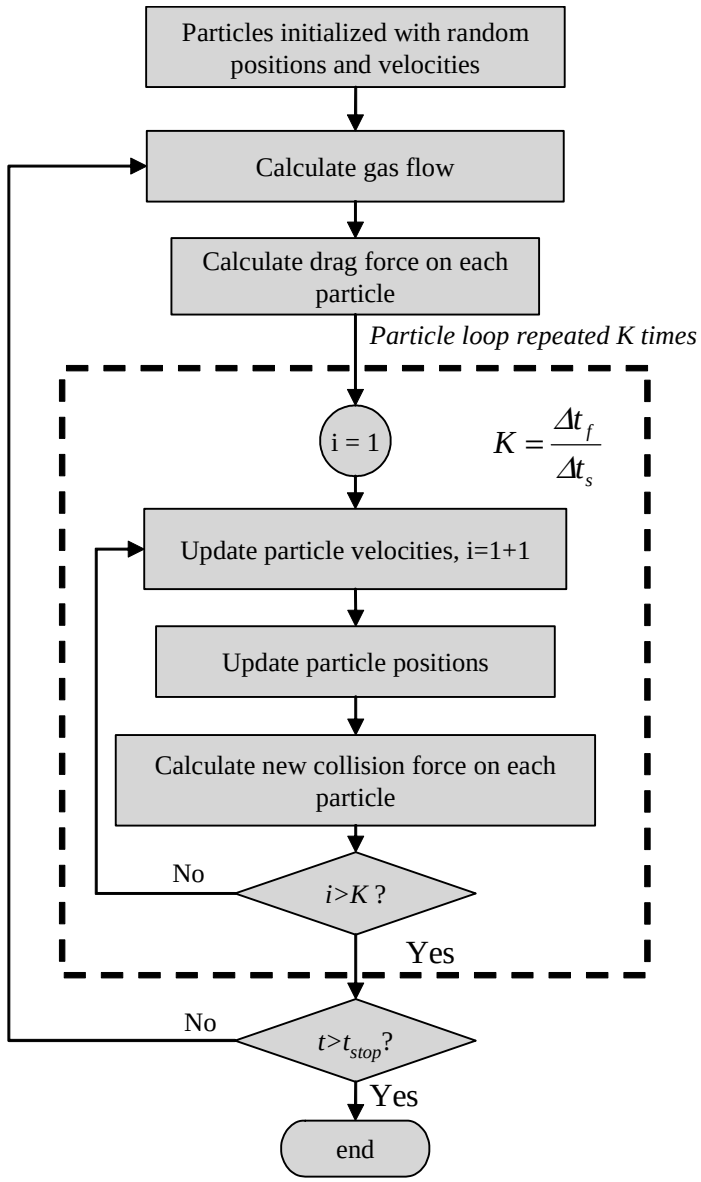

Fig. 6.6 *Fluidized Bed simulation algorithm.*

solids volume fraction ($\varepsilon_{s,mn}$) is calculated as follows:

$$\varepsilon_{s,mn} = \frac{\sum_{i=1}^{n_{mn}} \forall_i}{V_{mn}} \tag{6.38}$$

where $\forall_i$ is the volume of the ith particle, $\varepsilon_{s,mn}$ is the solids volume fraction, V_{mn} is the volume of the grid cell and n_{mn} is the total number of particles in the *m*, *n* grid cell.

The average solids velocity is calculated by averaging over all the particles in a given grid cell:

$$\vec{v}_{s,mn} = \frac{\sum_{i=1}^{n_{mn}} \vec{v}_i}{n_{mn}} \tag{6.39}$$

where $\vec{v}_{s,mn}$ is the average solids velocity in grid cell *m*, *n*, and $\vec{v}_i$ is the velocity of particle *i*.

It should be noted that this method of calculating the void fraction (developed by Xu and Yu [21]) is not completely accurate as the particles confined to a single plane will not pack the same as particles allowed to move in a three-dimensional domain. Because of this discrepancy, a two-dimensional fluidized bed simulation and a three-dimensional fluidized experiment of the same height would not be expected to produce equivalent pressure drops. Other methods have been devised to calculate the void fraction. Hoomans *et al*. [29] calculated the void fraction as an area fraction ($\varepsilon_{g,2D}$), assuming the particles are discs in a plane. They then converted this area fraction to a void fraction using the following relation:

$$\varepsilon_{g,3D} = 1 - \frac{2}{\sqrt{\pi\sqrt{3}}}\left(1 - \varepsilon_{g.2D}\right)^{3/2} \tag{6.40}$$

which assumes equal spacing between the two-dimensional circular disks in a hexagonal lattice and three-dimensional spheres in a face centered cubic (FCC) lattice. This expression was later modified by van Wachem *et al*. [28] by adding an empirical parameter to take into account the non-ideal packing that occurs in three-dimensional systems. van Wachem *et al*. went on to compare the results using several different methods to calculate the void fraction and found that none of the methods result in a

predicted pressure drop that matches experimental pressure drops for a bed of equal height. Nonetheless, as will be shown in Section 6.4.2.2, the inaccuracy imposed by this conversion of the void fraction appears to have little effect on the predicted minimum fluidization velocities, which match closely with those obtained from empirical relations.

6.3.2 Balance of Forces between Fluid and Solid Phase

An important issue in the coupling of the two phases is that the force exerted by the fluid on the particles must balance the force exerted by the particles on the fluid in order to satisfy Newton's third law of motion. Some of the early Eulerian-Lagrangian fluidized bed models did not meet this criterion. Both Tsuji *et al*. [17] and Hoomans *et al*. [29] implemented forces on the particles individually and implemented the force on the fluid based on the bulk properties of each computational cell. This approach does not guarantee that the forces will be balanced. This discrepancy was first noted by Xu and Yu [21], who ensured that the forces would balance by defining the force of the particles on the fluid to be the sum of the fluid forces on each particle for a given computational cell. Hoomans *et al*. corrected the earlier inconsistency in a later work [30].

The coupling method implemented in this work does correctly balance the forces between particles and the fluid. By using the average particle velocity in a given grid cell to calculate the drag force on each individual particle, the drag force is the same on every particle in a give grid cell. A comparison equations 6.34 and 6.39, indicates that the force on each particle is simply the drag force exerted on the fluid

for the given computational cell, divided by the number of particles in that cell. This approach differs from the approach developed by Xu and Yu [21] and the approach developed by Hoomans *et al*. [30], but the approach used here does still satisfy Newton's third law of motion.

6.4 Model Verification and Validation

Various test cases have been examined for the purposes of model verification and validation. Verification refers to the process of ensuring numerical accuracy of the model solution, where as validation refers to the ability of the model to accurately predict system behavior (i.e, verification deals with numerics while validation deals with physics) [31]. Although full verification and validation are not possible from a practical standpoint, an acceptable level of confidence in the model is instead pursued. In this work, verification and validation efforts focused on the discrete-element portion of the simulation, since the fluid-phase portion of MFIX has been thoroughly tested and documented [15, 32-35].

6.4.1 Verification Methods

Although the verification of the fluid-phase equations in the MFIX code is not examined in this effort, particular attention is paid to the numerical settings involved with the solution of the equations. More specifically, to ensure that the fluidized-bed results are relatively insensitive to numerical parameters, the time step associated with the dynamic solution of both phases and the size of the spatial grid were systematically varied. These results are presented in Appendix E. The parameters

varied include the gas-phase time step (Δt_f), the solid-phase time step (Δt_s), the number of computational cells in the x-direction (m_{max}), and the number of computational cells in the y-direction (n_{max}). For all parameters investigated, the simulation results do not vary significantly as the settings were changed from the default values (Table 6.2).

The discrete-particle portion of the fluidized bed model was verified by simulating two-particle collisions and comparing the post-collisional velocities with calculations performed in a spreadsheet. This procedure was carried out for non-cohesive particles, as well as for simulations using the square-well and Hamaker model. For the cohesive cases, three-particle simulations were also compared to spreadsheet calculations to ensure that agglomeration and breakup of two-particle agglomerates by a third particle are mathematically correct.

6.4.2 Model Validation

6.4.2.1 Qualitative Validation

The first effort to validate the results of the fluidized-bed model involved a qualitative examination of animations. Animations were examined for 2-particle systems, 3-particle systems and 10-particle systems to ensure that particle interactions are resolved in a realistic manner (e.g., particles do not pass through each other). This assessment involved both cohesive and non-cohesive systems. Animations were also examined for non-cohesive fluidized beds with 4,000-20,000 particles. As demonstrated in Figure 6.7, these animations exhibit realistic bubbling behavior. Animations were also examined for cohesive simulations. These results, which are

consistent with the known qualitative behavior of cohesive systems, will be discussed in the next chapter.

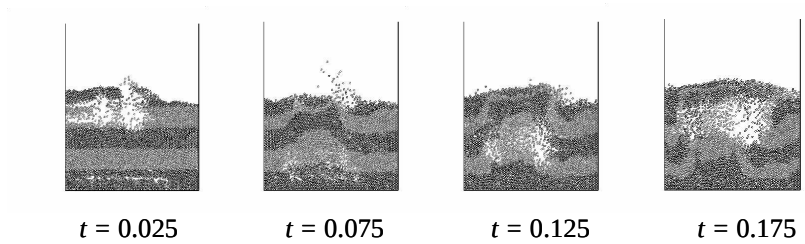

Fig 6.7 *Snapshots from non-cohesive bubbling fluidized bed simulation (4000 particles, U_s=91.6 cm/s).*

The identification of the frequently-observed, pressure-drop hysteresis was used as another qualitative benchmark to gauge the effectiveness of the simulation. In experimental efforts, fluidized beds exhibit a hysteresis in the plot of pressure drop versus superficial velocity [36]. A hypothetical defluidization / fluidization cycle is shown in Figure 6.8. With the particle bed starting in the bubbling state, the gas velocity is gradually decreased to zero in small, stepped increments (defluidization cycle). Once the particles are in the packed state, the superficial velocity (U_s) is increased in a similar manner. An increase in the gas velocity will increase the pressure drop across the particles, due to increased frictional losses. Once the fluidized state is reached, the pressure drop will remain constant at a value equal to the weight of the particles divided by the cross-sectional area of the bed. However, just prior to fluidization, a pressure overshoot [$\Delta P/(W/A_b) > 1$] is observed in experiments. This pressure overshoot does not occur as the gas velocity is decreased (Figure 6.8). This aspect of fluidized beds will be investigated in more detail in Chapter 8.

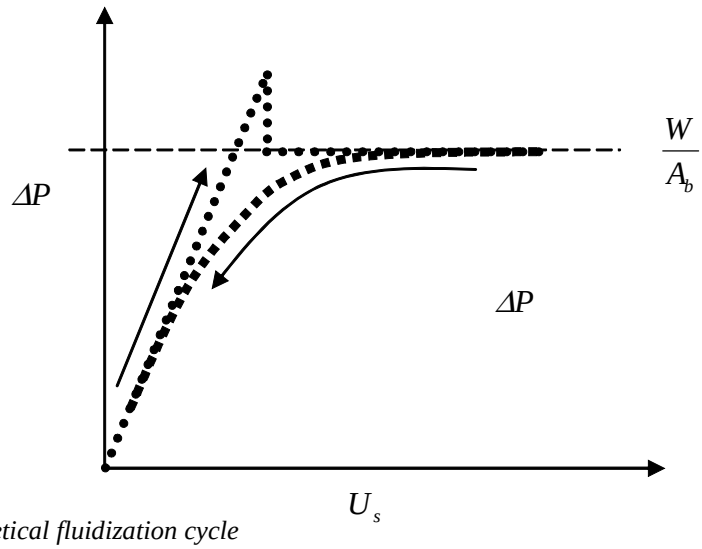

Fig 6.8 *Hypothetical fluidization cycle*

To test the ability of the fluidized-bed simulation to predict this behavior, the particles were brought to a bubbling state (U_s = 120 cm/s). Next, the gas velocity was slowly decreased in 37 equal steps to a superficial velocity of U_s = 56.76 cm/s over the course of 3.7 seconds (i.e., each gas velocity was maintained constant for 0.1 second). Three additional steps were used to take the superficial velocity to zero in 0.3 seconds. The inlet gas velocity was then gradually increased in stepped increments, using the reverse of the defluidization procedure. At each step, the gas velocity was maintained long enough to allow the bed to come to a statistical steady state (0.1 seconds). The steady-state pressure drop was then measured at each inlet velocity to compile a plot of pressure drop versus superficial velocity. The pressure drop across the bed was estimated by the pressure calculated at the lowest computational node along of the fluidized bed (i.e., the first computational node above the distributor plate). This quantity is averaged over time. The superficial gas velocity (U_s) was calculated by summing the overall volumetric flow rate through

the inlet jets and dividing this quantity by the cross-sectional area of the bed (A_b) as follows:

$$U_s = \frac{\sum_{i=1}^{n_{jets}} A_{jet} V_{jet}}{A_b} \tag{6.41}$$

where the volumetric flow rate through each jet is the specified gas velocity at that jet (V_{jet}) multiplied by the cross sectional area (A_{jet}) of that jet. The simulation predicts the expected hysteretic behavior, as is exhibited in Figure 6.9. These results also display large variation in the pressure drop just above the minimum fluidization velocity due to bubbling. There also some notable discrepancies between the predicted behavior and the behavior that has been observed in experiments. The pressure decrease at incipient fluidization is not as abrupt in the simulation results as it has been observed in experimental results. Also the packed bed portion of the defluidization curve predicted here is more linear than in experimental data [37].

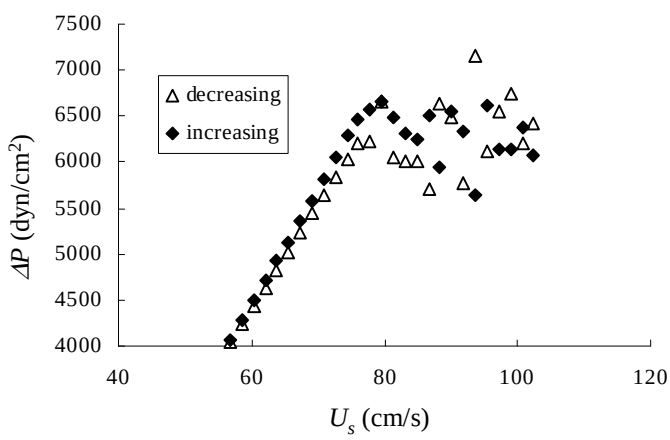

Fig. 6.9 *Results of fluidized bed simulation showing hysteresis in fluidization curve.*

6.4.2.2 Quantitative Validation

In addition to the qualitative benchmarks discussed in the previous section, plots of pressure drop versus superficial velocity also provide quantitative validation. Specifically, once the inlet velocity is high enough to fluidize all particles in the bed, the pressure drop across the particles multiplied by the cross-sectional area should balance the total weight [38]. This pressure drop was determined using the same procedure described in the previous section. The calculation of the weight of the particles is complicated by the discrete nature of the solution to the gas-phase equations, which does not allow for calculation of the pressure at the very bottom of the fluidized bed. As illustrated in Figure 6.10, the lowest point at which the pressure is calculated is at the middle of the lowest computational cell. Therefore, when comparing the pressure drop to the weight of the particles, only those particles above the middle of the lowest computational cell are considered.

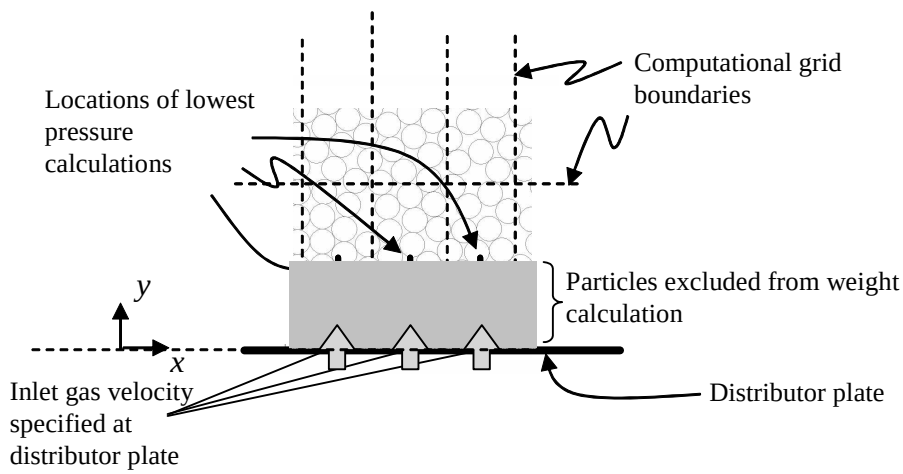

Fig. 6.10. *Methodology in calculating theoretical fluidized bed weight (W_{theo}).*

As expected, the weight of these particles, which will be called the theoretical bed weight (W_{th}), is balanced by the simulated pressure drop, as displayed in Figure 6.11. The data presented in Figure 6.11 is the average of three replicate runs and the

error bars are the standard deviation in the pressure at each superficial velocity. The inclusion of additional replicates did not reduce the size of the error bars.

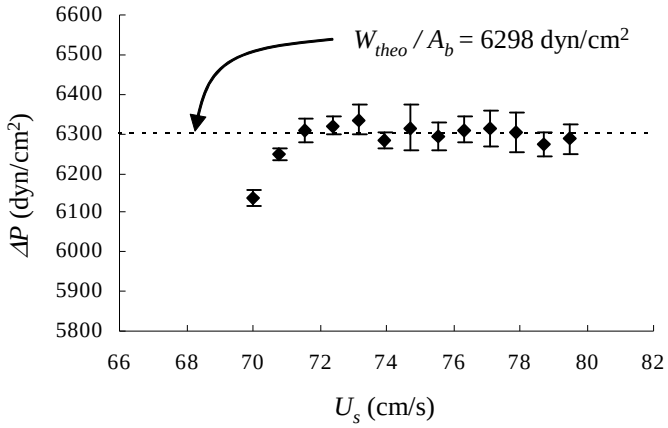

Fig 6.11. *Comparison of calculated pressure drop to weight of particle bed.*

Another important quantitative benchmark is the minimum fluidization velocity. The minimum fluidization generally refers to the velocity above which further increases in the superficial velocity do not cause a further increase in the bed pressure drop. In previous efforts, however, some ambiguity exists in the exact procedure used to determine the minimum fluidization velocity. Figure 6.12 depicts the typical defluidization and fluidization branches of the pressure drop (ΔP) versus superficial velocity plot (U_s). As the superficial velocity is increased through the packed bed regime, a point will be reached at which the pressure drop is equal to the weight of the particles (point A in Figure 6.12). Some efforts have identified this velocity as the minimum fluidization velocity [39, 40] even though the particles are not fluidized at this point. As the superficial velocity is increased further, a point is reached at which the pressure overshoot is sufficient to free the particles from their packed configuration (point B in Figure 6.12). This point has been identified as the minimum fluidization velocity by some authors [38], although the pressure will

decrease slightly beyond this point as the particle bed expands. As the superficial velocity is decreased from the bubbling state, a velocity is reached where the pressure drop starts to decrease (point C in Figure 6.12). At this point, the fluidized particles are gradually transitioning to the packed state. Some references have identified this point as the minimum fluidization velocity [15, 18, 20, 41]. While all three of these velocities loosely satisfy the vague definition of the minimum fluidization velocity given earlier, the associated numerical values are different. For the purposes of this project, point A is referred to as the theoretical minimum fluidization velocity ($U_{mf,th}$), point B is referred to as the incipient fluidization velocity ($U_{mf,in}$), and point C is referred to as the defluidization velocity ($U_{mf,df}$).

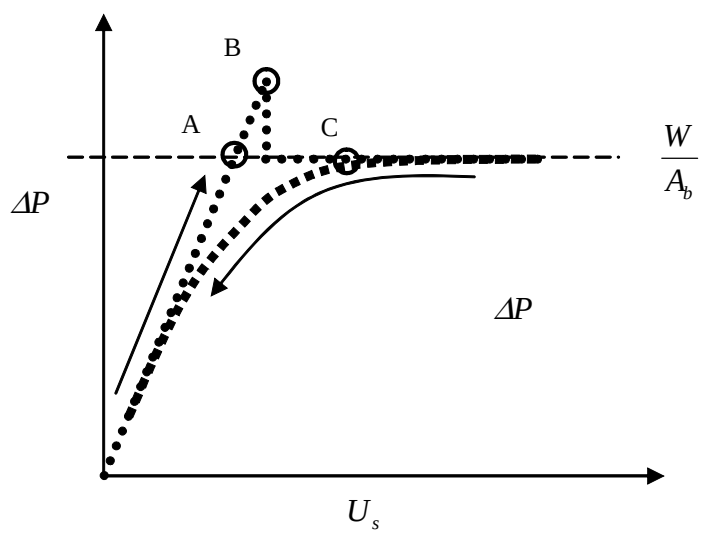

Fig 6.12 *Points identified as minimum fluidization velocity in previous studies.*

The procedure for calculating these critical velocities involves graphical analysis of the pressure drop versus superficial velocity curve obtained from simulations. A representative defluidization (decreasing U_s) curve is displayed in Figure 6.13. Plots such as this are used to identify the defluidization velocity. A

straight line is fitted to the points in the packed bed region and the intersection of this line with the W'/A_b line is the defluidization velocity.

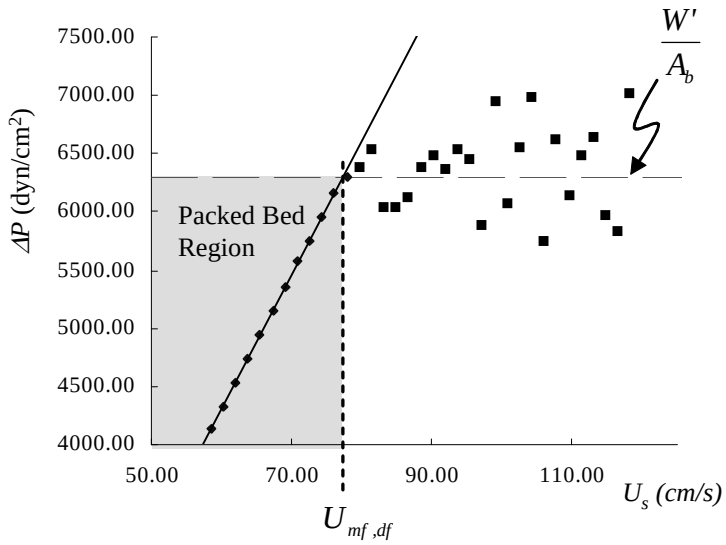

Fig 6.13 *Typical defluidization curve (decreasing U_s) used to identify defluidization velocity.*

A fluidization curve (increasing U_s) is displayed in Figure 6.14. Plots such as this are used to calculate the theoretical minimum fluidization velocity, the incipient fluidization velocity and the pressure overshoot (ΔP_{over}). In order to calculate the theoretical minimum fluidization, a straight line is fitted to all the points in the packed bed region of the plot. The theoretical minimum fluidization is taken to be the intersection of this straight line and the W'/A_b line. Those data points above the W'/A_b line, yet to the left of the bubbling region are considered to be in the pressure overshoot region. The incipient fluidization velocity is read at the maximum pressure recorded in the pressure overshoot region. The pressure overshoot is simply the difference between the maximum pressure in this region and the W'/A_b line.

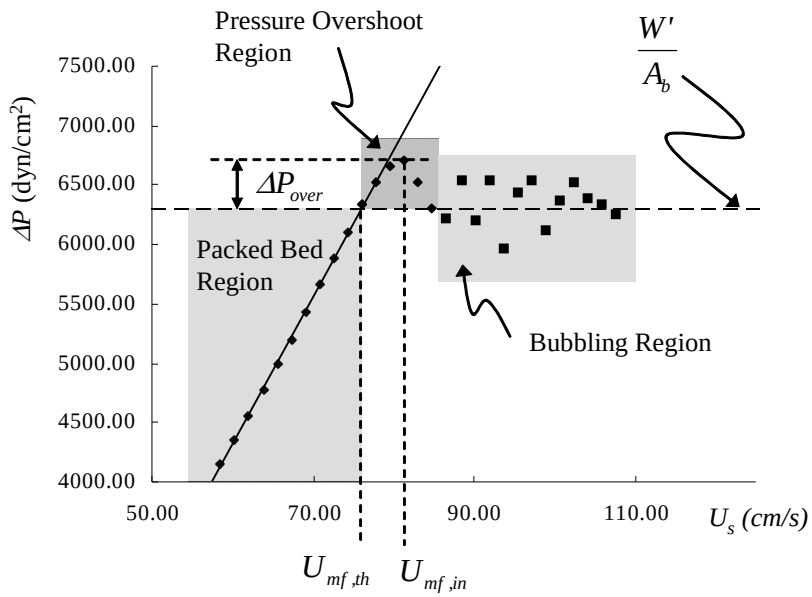

Fig. 6.14 *Typical fluidization (increasing U_s) curve used to identify the pressure overshoot, theoretical minimum fluidization velocity and incipient minimum fluidization velocity.*

Correlations for the minimum fluidization velocity are well-documented [38, 42]. These correlations are developed by equating the weight of the particles in the bed (divided by the bed cross-sectional area) with empirical relations for the pressure drop in a packed bed such as the Ergun equation [38]. The intersection of these correlations is often referred to as the minimum fluidization velocity, which corresponds to the theoretical minimum fluidization velocity ($U_{mf,th}$) described above. These correlations are highly sensitive to the void fraction at minimum fluidization. For example, for a change in the void fraction from 0.43 to 0.46, the Ergun equation predicts that the theoretical fluidization velocity changes from 68.53 cm/s to 80.89 cm/s. With such differences in mind, simulation results are compared with correlation predictions to ensure that the simulation results are reasonable. Specifically, the void fraction calculated by the simulation at minimum fluidization is

employed in the correlation equation. An upper and lower limit are used for the void fraction because this value fluctuates with time and location in the bed. The upper limit of the void fraction was taken from the average void fraction along the centerline plus the standard deviation, while the lower limit was the same average minus the standard deviation. In Figure 6.15, the range of predicted incipient fluidization velocities is compared to the theoretical minimum fluidization velocity predicted by the fluidized-bed model for three particle diameters (d_p). The transition from packed bed to fluidized bed calculated by the simulation falls within the range of fluidization velocities predicted by the Ergun correlation for each particle diameter.

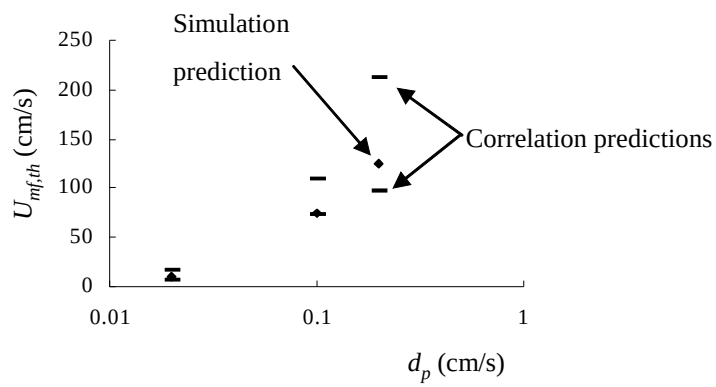

Fig. 6.15 *Theoretical minimum fluidization velocities at varying particle diameter.*

From this point on, pressure drop results will be presented as a normalized pressure drop (ΔP^*), which is the pressure drop divided by the theoretical particle weight (W'/A_b). Furthermore, critical fluidization velocities will be presented in a normalized form ($U^*_{mf,**}$) which is the given critical velocity divided by the corresponding velocity for the non-cohesive case. In plots of the fluidization cycle and defluidization cycle, the superficial velocity will be normalized by the theoretical minimum fluidization velocity predicted by the non-cohesive simulation (Table 6.3).

The other values of the non-cohesive critical fluidization velocities used for normalization are also presented in Table 6.3.

Table 6.3*. Non-cohesive critical velocities*

$U_{mf,th}$	$U_{mf,in}$	$U_{mf,df}$
71.93	74.32	72.99

6.5 References

1. D. S. Boyalakuntla, "Simulation of Granular and Gas-Solid Flows Using Discrete Element Method", PhD dissertation, Carnegie Mellon University, 2003.
2. M. Syamlal, W. Rogers, and T. J. O'Brien, MFIX Documentation Theory Guide, U.S. Department of Energy, Morgantown, West Virginia, 1993.
3. E. Barthel and G. Haiat, Approximate model for the adhesive contact of viscoelastic spheres, *Langmuir* 18 (2002) 9362.
4. M. Syamlal and T. O'Brien, Derivation of a drag coefficient formula from velocity-voidage correlations, *DOE internal report* (1994)
5. J. M. Dalla Valle, Micromeritics, Pitman, London, 1948.
6. J. Garside and M. R. Al-Dibouni, Velocity-voidage relationships for fluidization and sedimentation in solid-liquid systems, *Ind. Eng. Chem., Process Des. Dev.* 16 (2) (1977) 206.
7. S. V. Patankar, Numerical Heat Transfer and Fluid Flow, Hemisphere, New York, 1980.
8. M. Syamlal, MFIX Documentation Numerical Technique, Morgantown, West Virginia, 1998.
9. M. P. Allen and D. J. Tildesley, Computer Simulation of Liquids, Oxford University Press, Oxford, 1987.
10. W. Goldsmith, Impact: the theory of physical behavior of colliding solids, E. Arnold, London, 1960.
11. C. K. Lun and S. B. Savage, The effects of an impact velocity dependent coefficient of restitution on stresses developed by sheared granular materials, *Acta Mechanica* 63 (1986) 15.
12. S. F. Foerster, M. Y. Louge, H. Chang, and K. Allia, Measurements of the collision properties of small spheres, *Phys. Fluids* 6 (3) (1994) 1108.
13. G. Kuwabara and K. Kono, Restitution coefficient in a collision between two spheres, *Japanese Journal of Applied Physics* 26 (8) (1987) 1230.
14. L. Labous, A. D. Dosato, and R. N. Dave, Measurements of collisional properties of spheres using high-speed video analysis, *Physical Review E* 56 (5) (1997) 5717.
15. D. Gera, M. Gautam, Y. Tsuji, T. Kawaguchi, and Y. Tanaka, Computer simulation of bubbles in large-particle fluidized beds, *Powder Technology* 98 (1998) 38.
16. A. V. Potapov and C. S. Campbell, Computer simulation of shear-induced particle attrition, *Powder Technology* 94 (2001) 109.
17. Y. Tsuji, T. Kawaguchi, and T. Tanaka, Discrete particle simulation of two-dimensional fluidized bed, *Powder Technology* 77 (1993) 79.
18. T. Kawaguchi, T. Tanaka, and Y. Tsuji, Numerical simulation of two-dimensional fluidized beds using the discrete element method (comparison between two- and three-dimensional models), *Powder Technology* 96 (1998) 129.
19. S. Limtrakul, A. Chalermwattanatai, K. Unggerawirote, Y. Tsuji, T. Kawaguchi, and W. Tanthapanichakoon, Discrete particle simulations of solids motion in a gas-solid fluidized bed, *Chemical Engineering Science* 58 (2003) 915.
20. T. Mikami, H. Kamiya, and M. Horio, Numerical simulation of cohesive powder behavior in a fluidized bed, *Chemical Engineering Science* 53 (10) (1998) 1927.

21. B. H. Xu and A. B. Yu, Numerical simulation of the gas-solid flow in a fluidized bed by combining discrete particle method with computational fluid dynamics, *Chemical Engineering Science* 52 (16) (1997) 2785-2809.
22. S. Yuu, T. Umekage, and Y. Johno, Numerical simulation of air and particle motions in bubbling fluidized bed of small particles, *Powder Technology* 110 (2000) 158.
23. F. P. Bowden and D. Tabor, Friction and lubrication, Wiley, London, 1956.
24. A. B. Stevens and C. M. Hrenya, Comparison of soft-sphere models to measurements of collision properties during normal impacts, *submitted to Powder Technology* (2004)
25. H. King, R. White, I. Maxwell, and N. Menon, Inelastic impact of a sphere on a massive plane: nonmonotonic velocity-dependence of the restitution coefficient, (not published)
26. J. Israelachvili, Intermolecular and Surface Forces, Academic Press London, London, 1991.
27. J. P. K. Seville, Processing of Particulate Solids, Blackie Academic and Professional, London, 1997.
28. B. G. M. van Wachem, van der Schaaf J., Schouten, J.C., Krishna, R., van den Bleek, C.M., Experimental validation of Lagrangian-Eulerian simulations of fluidized beds, *Powder Technology* 116 (2001) 155-165.
29. B. P. B. Hoomans, J. A. M. Kuipers, W. J. Briels, and W. P. M. V. Swaaij, Discrete particle simulation of bubble and slug formation in a two-dimensional gas-fluidised bed: a hard-sphere approach, *Chemical Engineering Science* 51 (1) (1996) 99.
30. B. P. B. Hoomans, J. A. M. Kuipers, M. A. M. Salleh, M. Stein, and J. P. K. Seville, Experimental validation of granular dynamics simulations of gas-fluidised beds with homogenous in-flow conditions using positron emission particle tracking, *Powder Technology* 116 (2001) 166.
31. J. R. Grace and F. Taghipour, Verification and validation of CFD models and dynamic similarity for fluidized beds, *Powder Technology* 139 (2004) 99.
32. N. Xie, F. Battaglia, and R. O. Fox, Simulations of multiphase reactive flows in fluidized beds using in situ adaptive tabulation, *Combustion Theory and Modeling* 8 (2) (2004) 195.
33. M. Syamlal and T. J. O'Brien, Fluid dynamic simulation of O-3 decomposition in a bubbling fluidized bed, *AIChE Journal* 49 (11) (2003) 2793.
34. T. McKeen and T. Pugsley, Simulation of cold flow FCC stripper hydrodynamics at small scale using computational fluid dynamics, *International Journal of Chemical Reactor Engineering* A18 (2003)
35. T. McKeen and T. Pugsley, Simulation and experimental validation of a freely bubbling bed of FCC catalyst, *Powder Technology* 129 (2003) 139.
36. D. Kunii and O. Levenspiel, Fluidization Engineering, Butterworth-Heinemann, Boston, 1991.
37. S. C. Tsinontides and R. Jackson, The mechanics of gas fluidized beds with an interval of stable fluidization, *Journal of Fluid Mechanics* 255 (1993) 237.
38. M. Rhodes, Introduction to Particle Technology, John Wiley and Sons Ltd., West Sussex, England, 1998.
39. B. H. Xu, Y. C. Zhou, A. B. Yu, and P. Zulli, Force structures in gas fluidized beds of fine powders, *World Congress on Particle Technology 4, Sydney, Australia* (2002)
40. M. J. Rhodes, X. S. Wang, M. Nguyen, P. Stewart, and K Liffman, Onset of cohesive behavior in gas fluidized beds: a numerical study using DEM simulation, *Chemical Engineering Science* 56 (2001) 4433-4438.
41. P. C. Wright and J. A. Raper, Role of liquid bridge forces in cohesive fluidization, *Transactions of the Institution of Chemical Engineers* 76 (1998) 753.
42. C. J. Geankopolis, Transport processes and unit operations, Allyn and Bacon, Boston, 1983.

Chapter 7. Comparison of Square-Well Potential and Hamaker Model for van der Waals Forces

As stated in Chapter 1, one of the main objectives of this work is to assess the effectiveness of the square-well potential to capture the effect of cohesion in particulate systems. To achieve this objective, a comparison is made between the simulation results based on a square-well model for cohesion with those of a more elaborate model for cohesion, namely the Hamaker description of van der Waals forces. This comparison is a two-step process. First, a method is devised to determine parameters for both cohesion models (i.e., square well and Hamaker) that would be expected to produce an "equivalent" effect in the discrete-particle simulations. The second part of this process is to devise appropriate methods for comparing the results of the two models. This first part of this chapter deals with the former part of this process, which is the development of a mapping from Hamaker parameters to equivalent square-well parameters. The second part of this chapter covers the qualitative and quantitative methods used to compare the results of the two treatments, with a focus on a fluidized-bed system.

7.1 Parameter Mapping between Hamaker Model and Square-Well Model

In order for a simplified model like the square-well to be useful, a physical basis for choosing values of input parameters is needed. The inputs for the more elaborate Hamaker model are based on material considerations and thus a mapping from these quantities to the square-well inputs is sought. More specifically, the input parameters needed for the Hamaker model is the Hamaker constant (A) and a cutoff

distance (H_{cut}), whereas the square-well model requires input values for the well depth (D) and the well width (r_{outer}). The Hamaker constant and cutoff distance control the magnitude and characteristic length, respectively, in the Hamaker model. With the square-well model, the well depth controls the magnitude of the cohesive force and the well width (defined in terms of the ratio of well width to inner radius, r_{outer}/r_{inner}) controls the length scale associated with the square-well model. The Hamaker cutoff distance (4×10^{-10} m) is set to match the interatomic distance of many common solids [1]. Because these models are physically different, no set of parameters will produce *exactly* the same effects on individual particles. However, it may be possible for the two models to produce *similar* results on a locally-averaged scale. With these ideas in mind, several strategies were considered as the basis for the mapping between parameters, as detailed below.

7.1.1 Force Comparison

A basic gauge of the level of particle cohesion is the magnitude of the cohesive force experienced by both particles. Unfortunately, using this force as a common ground to determine equivalent parameters for the square-well and Hamaker models has some fundamental problems. As displayed in Figure 7.1, the Hamaker model is defined by a cohesive force that varies as a function of separation distance. Therefore, to use a single force to characterize the level of cohesion, additional stipulations would be necessary (e.g. specific separation distance, averaging over a specified range).

A characteristic force is even less intuitive with the square-well model, since this model is not defined in terms of force, but in terms of the kinetic energy change for the given two-particle system. This change in kinetic energy is implemented in the form of a momentum impulse, thereby making the force infinite at a given distance between the particles and zero everywhere else (Figure 7.1). For these reasons, the use of an interparticle force as a basis for the mapping from the Hamaker model to the square-well model is inadequate.

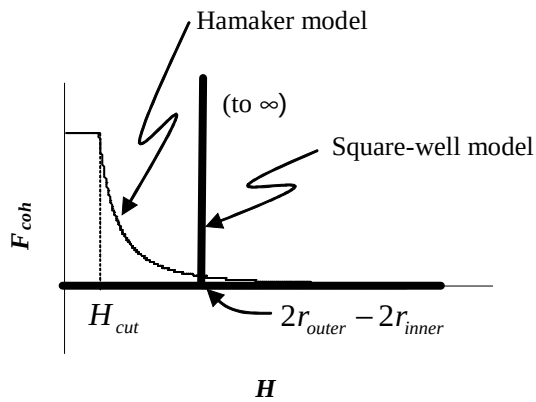

Fig. 7.1 *Force versus separation distance for Hamaker and square-well cohesion models.*

7.1.2 Potential Energy Comparison

Another possible mapping method is to set the parameters in each model such that the overall potential energy change in a given particle-particle interaction is the same for each model. When using the square-well model, the overall potential energy change is simply equal to the depth of the square well. However, the overall potential energy change induced by the Hamaker model is more complicated. In general, the energy change between two bodies experiencing an attractive force is equal to the negative of the work done by the attractive force [2]. This quantity can be obtained by integrating the attractive force over the distance traveled by the two bodies:

$$\Phi_{vdW} = -\int_{H_1}^{H_2} F_{vdW}\, dH \tag{7.1}$$

where Φ_{vdW} is the potential energy of a two-particle system experiencing attractive Hamaker forces, H_1 is their initial separation distance and H_2 is their final separation distance. As described in Section 6.3.1, the Hamaker model used here is characterized by a force that changes with separation distance (equation 6.35) until a specified cutoff distance is reached, below which the force remains constant (equation 6.38). Using both of these expressions in the above equation leads to the following expression for the change in potential energy:

$$\Phi_{vdW} = -\int_{\infty}^{H_{cut}} \frac{Ar_{inner}}{12H^2} dH - \int_{H_{cut}}^{-\delta_{n,max}} 2\pi r_{inner}\, \gamma dH \tag{7.2}$$

where A is the Hamaker constant, r_{inner} is the particle radius, H is the surface-to-surface particle separation distance, γ is the surface energy and $\delta_{n,max}$ is the maximum normal overlap between the particles during the soft-sphere collision. Because the Hamaker van der Waals force is negligible at large separation distances, integration of equation 7.2 leads to the following expression:

$$\Phi_{vdW} = -\frac{Ar_{inner}}{12H_{cut}} - 2\pi r_{inner}\, \gamma\left[H_{cut} + \delta_{n,max}\right] \tag{7.3}$$

While the distance traveled by the particles from the inner cutoff to the maximum overlap is very small, the van der Waals force is also at its maximum over this interval (Figure 7.1), so the second term in equation 7.3 cannot be ignored. This treatment leads to the potential energy displayed in Figure 7.2. In order to calculate a value for the Hamaker potential energy change, the maximum overlap ($\delta_{n,max}$) must be known. For a non-cohesive system, this quantity can be calculated from the

equation of motion of the two colliding particles combined with the spring-and-dashpot force law (Appendix B). However, this solution shows that the maximum overlap, and thus the potential energy change, is a function of the initial relative normal velocity. Because the potential energy change with the square-well model is not a function of relative normal velocity, this mapping method is inconsistent at the particle level. Furthermore, the determination of the maximum overlap, upon which this mapping method depends, is much more complex with the inclusion of cohesion (Appendix C). In particular, if the Hamaker cohesion force is included in the particle equations of motion, an analytical solution is not possible and the maximum overlap must be determined numerically. Overall, these two issues indicate that a mapping method based on achieving the same potential energy change is a poor choice.

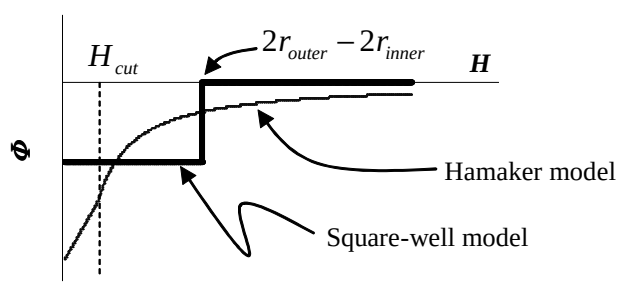

Fig. 7.2 *Potential energy associated with the Hamaker and square-well cohesion models.*

7.1.3 Escape-Velocity Comparison for Head-On Collisions

Another possible method of mapping input parameters is to match the "escape" velocity that demarcates agglomeration (capture) and separation (escape) of two colliding particles. By default, this method will overcome the issues related to the initial, relative, normal velocity discussed in the previous section. With both models, a unique velocity exists such that all interactions with an approaching relative velocity below the escape velocity will result in the formation of an agglomerate. For

head-on (normal) collisions, the parameters in each model that control the magnitude of the cohesive force (*A* in the Hamaker model and *D* in the square-well model) dictate the escape velocity. Higher levels of cohesion (higher *A* or *D*) result in higher escape velocities. (Note that head-on collisions preclude the influence of length scale, namely r_{inner}/r_{outer} and H_{cut}, on the escape velocity. The influence of length-scale on oblique collisions will be detailed in Section 7.3)

For the square-well model, the escape velocity can be calculated analytically. During an interaction between the ith and j^{th} particles, the criterion for agglomerate formation is defined in equation 3.8 as follows:

$$\left(\vec{k}_{ij,3} \cdot \vec{v}_{ij,c}\right)^2 - \frac{4D}{m} \leq 0 \qquad (7.4)$$

where $\vec{k}_{ij,3}$ is the unit vector between particle centers at the instant of the departing cohesive interaction, $\vec{v}_{ij,c}$ is the relative velocity after the inelastic collision and m is the particle mass. This expression defines the minimum departing velocity necessary to avoid agglomeration. By combining equation 7.3 with the equations relating the post-collisional velocities to the pre-collisional velocities for inelastic collisions (equation 3.3) and approaching cohesive interactions (equation 3.8), the minimum approaching relative velocity for escape ($v_{ij,esc}$) in a head-on collision can be obtained as follows (Appendix D):

$$v_{ij,esc} = \sqrt{\frac{4D}{m}\left(\frac{1}{e^2} - 1\right)} \qquad (7.5)$$

This expression can then be rearranged to provide the well depth required to achieve the desired escape velocity for a given coefficient of restitution:

$$D = \frac{m\left(v_{ij,esc}\right)^2}{4\left(\frac{1}{e^2} - 1\right)} \tag{7.6}$$

However, this expression is only valid for head-on collisions as the unit vector connecting the particle centers is not constant during the cohesive interaction sequence (approaching cohesive interaction, inelastic collision, departing cohesive interaction) for oblique interactions. If the normal unit vector changes during the interaction sequence derivation presented in Appendix D is not valid.

For the Hamaker model, an analytical solution for the escape velocity is not possible (Appendix C). Nonetheless, the escape velocity can be obtained numerically via a series of two-particle simulations. More specifically, as depicted in Figure 7.3, two particles are separated by a finite distance in the *x*-direction and have the same y-

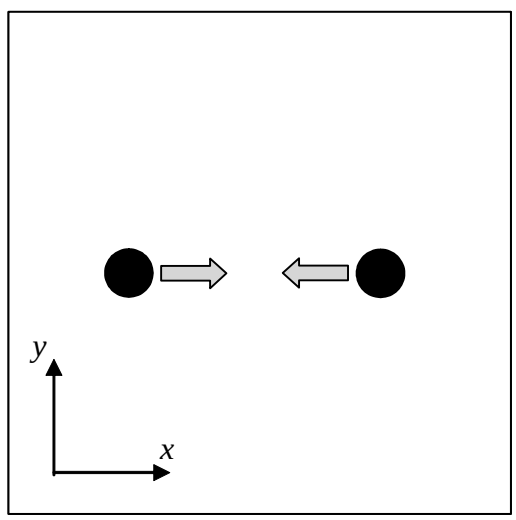

Fig. 7.3 *Layout of two-particle simulations used to determine escape velocity.*

coordinates. Furthermore, both particles are given a zero velocity in the *y*-direction. The *x*-component of velocities are set to equal and opposite values. The simulation is allowed to proceed in time until a determination is made as to whether the particles escape or agglomerate. To determine the escape velocity, a series of simulations are

run and the *x*-component of velocity of each particle is gradually increased (or decreased) in each simulation until the transition from agglomeration to escaping (or vice-versa) is achieved.

For the purposes of this work, equation 7.5 is used to develop a table of escape velocities for various cohesive well depths. Two-particle simulations are used to develop a table of escape velocities associated with different levels of cohesion with Hamaker model. A comparison between both tables is then used to match equivalent cohesion parameters from each model (*D* and *A*). As detailed in the next section, many-particle simulations are then run with both models to assess the effectiveness of this mapping method. The values used in this assessment process are presented in Table 7.1.

Table 7.1. *Normal escape velocities obtained using both the square-well and Hamaker van der Waals models*

D (dyn cm)	$v_{ij,esc}$ ***(cm/s)***	***A (dyn cm)***	$v_{ij,esc}$ ***(cm/s)***
1.00E-04	0.179	3.34E-12	0.179
5.00E-04	0.400	7.49E-12	0.400
1.00E-03	0.566	1.06E-11	0.566

7.2 Assessment of Mapping Method via Many-Particle Simulations

The escape-velocity mapping is based on the behavior of two-particle interactions. The mapping is now extended to many-particle systems to determine if similar fluidized bed behaviors are obtained. The range of cohesive forces investigated is chosen to obtain the maximum cohesive forces possible, without exhibiting plugging and/or channeling. The useful range of parameters for each model that produce these conditions provides an initial means of testing the escape-velocity mapping method. For these simulations, r_{outer}/r_{inner} is kept constant at 1.01 and H_{cut} is

kept constant at 4 x 10^{-10} m. The effect of these parameters is examined in Section 7.2.2.3.

7.2.1 Qualitative Comparison: Defluidization

From a practical standpoint, the most undesirable consequence of cohesion in fluidized beds is the inability to fluidize in a conventional manner (homogenous or bubbling) due to the formation of plugs or channels. In terms of the Geldart classification [3] (see Figure 1.2), this behavior is exhibited by for Type C (relatively small, cohesive) particles. The simulation developed here is capable of predicting this type of behavior with both cohesion models. With the square-well model, plugging and channeling occur at roughly $D > 10^{-3}$, while simulations using the van der Waals model exhibits plugging and channeling at approximately $A > 10^{-11}$. These parameters map to escape velocities that are roughly same (see Table 7.1). It is worthwhile to note, though, that the transition from Type A (fluidizable) to Type C (not fluidizable) behavior is not sufficiently abrupt to be used as a quantitative benchmark for validating the mapping.

As an aside, this level of cohesion ($A = 10^{-11}$) corresponds to a cohesive force to particle weight ratio of approximately 20. Previous efforts to simulate cohesive gas-solid flows have observed similar levels of cohesion at the Type A – Type C boundary. Rhodes *et al.* [4] observed Type C behavior at cohesive-force-to-particle-weight-ratios greater than 46 with a simplified surface cohesion model. Ye *et al.* [5] observed this transition at a ratio of 56 with a van der Waals model. From an experimental standpoint, the cohesive-force-to-particle-weight ratio for the transition

to Type C behavior is known to vary significantly depending on the nature of the cohesive forces. Data provided by Molerus [6] indicate that the Type A-Type C transition occurs for a cohesive-force-to particle-weight ratio of about 1900 for micron-sized particles experiencing van der Waals forces. Experiments with controlled liquid bridging forces by McLaughlin and Rhodes [7] revealed that the critical ratio is approximately 1. While defluidization occurs at relatively similar levels of cohesion (i.e. mapped to the same escape velocity) for both the models investigated here, the nature of the defluidization is different.

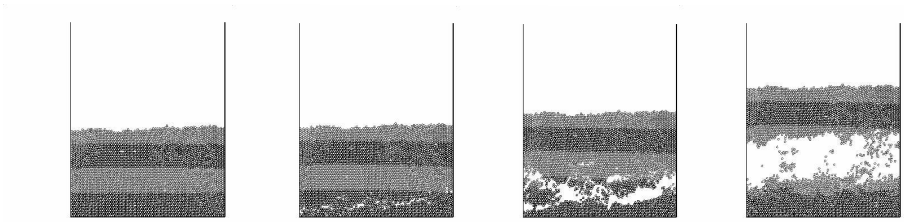

t = 0.4 sec, $U_s^* = 0.94$ | t = 0.5 sec, $U_s^* = 1.02$ | t = 0.6 sec, $U_s^* = 1.10$ | t = 0.7 sec, $U_s^* = 1.18$

Fig. 7.4 *Square-Well model: Snapshots displaying plugging (D=1x10^{-3} erg).*

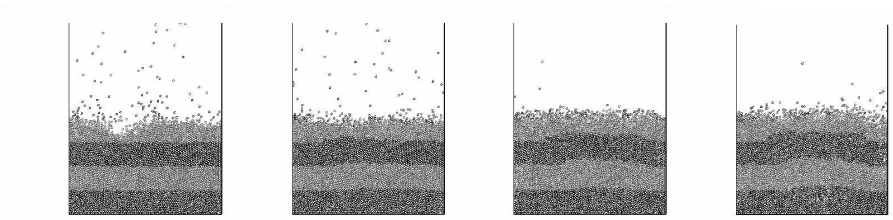

t = 0.4 sec, $U_s^* = 0.94$ | t = 0.5 sec, $U_s^* = 1.02$ | t = 0.6 sec, $U_s^* = 1.10$ | t = 0.7 sec, $U_s^* = 1.18$

Fig. 7.5 *Hamaker model: Snapshots displaying plugging (A=1x10^{-11} erg)*

As revealed in Figure 7.4, the square-well model forms plugs that extend across the bed diameter as a single mass. Plugs formed with the Hamaker model are not as strong and tend to break apart into stable channels as illustrated in Figure 7.5. For higher levels of cohesion, simulations using the van der Waals model exhibit the formation of a completely static bed structure as in Figure 7.6. This phenomenon is

not observed with simulations using the square-well potential. The plugs evident in Figure 7.4 are observed at all higher levels of cohesion. Video images of fluidized bed experiments [8] with Type C particles indicate that the solid-plugs predicted by the square-well model more closely approximate the experimental system. However, some experiments have shown the formation of stable, expanded bed structures due to cohesive effects [9], thus indicating that the Hamaker prediction may be more accurate.

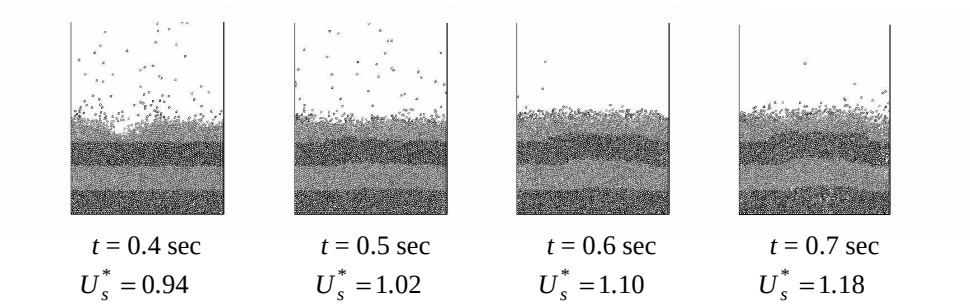

Fig. 7.6 *Hamaker model: Snapshots showing formation of static bed structure at high levels of cohesion ($A=1x10^{-10}$ erg).*

7.2.2 Qualitative Comparison: Mixing

In systems that do not exhibit plugging and channeling, mild levels of cohesion may have a significant effect on the mixing behavior. Figures 7.7 and 7.8 illustrate mixing behavior for the square-well and Hamaker models, respectively, during a fluidization cycle. In these snapshots, the particles were assigned colors in the left-most image so that the relative particle movement could be observed in the other three images. These simulations were run using the base parameter set presented in Table 6.2, with exceptions noted in the figure captions. The square-well and Hamaker parameter values used in both figures were matched using the escape-

velocity mapping. Qualitatively, the nature of the mixing associated with each model appears similar.

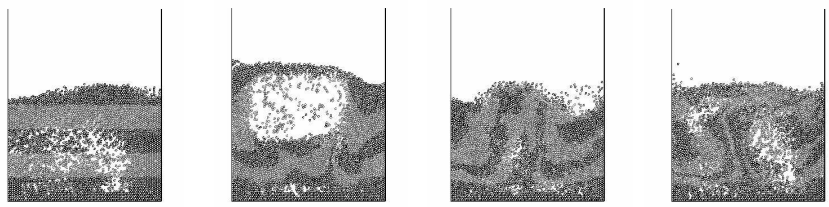

t = 7.5 sec	t = 7.6 sec	t = 7.7 sec	t = 7.8 sec
$U_s^* = 1.30$	$U_s^* = 1.33$	$U_s^* = 1.35$	$U_s^* = 1.38$

Fig 7.7 *Square-Well model: Mixing behavior in simulation (D=5x10^{-4} erg).*

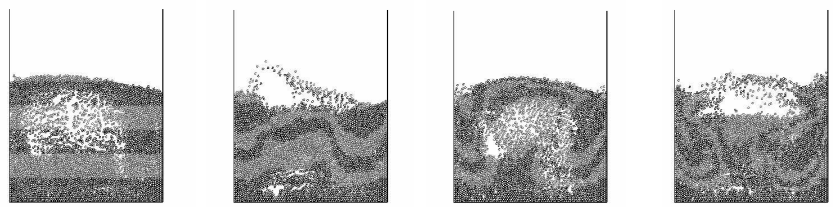

t = 7.5 sec	t = 7.6 sec	t = 7.7 sec	t = 7.8 sec
$U_s^* = 1.30$	$U_s^* = 1.33$	$U_s^* = 1.35$	$U_s^* = 1.38$

Fig 7.8 *Hamaker model: Mixing behavior in simulation (A=7.49x10^{-12} erg).*

In order to further investigate the nature of mixing in both models, a mixing index is used to quantify the extent of mixing [10]. The mixing index used here is defined by dividing all the particles in the bed into two "families" as seen in Figure 7.9. Family 1 includes all the particles that have a height equal to or greater than the median particle height for the bed in its initial, packed state (i.e., top half of bed). Family 2 includes all the particles with a height less than the median particle height (i.e., bottom half of bed). The mixing index, *I*, is defined as the ratio of average height of all the particles in family 1, $\langle h_1 \rangle$, to the average height of all the particles in family 2, $\langle h_2 \rangle$, as defined below:

$$I = \frac{\langle h_1 \rangle}{\langle h_2 \rangle} \qquad (7.7)$$

$$\langle h_1 \rangle = \frac{1}{n_1} \sum_{i=1}^{n_1} y_i \qquad (7.8)$$

$$\langle h_2 \rangle = \frac{1}{n_2} \sum_{i=1}^{n_2} y_i \qquad (7.9)$$

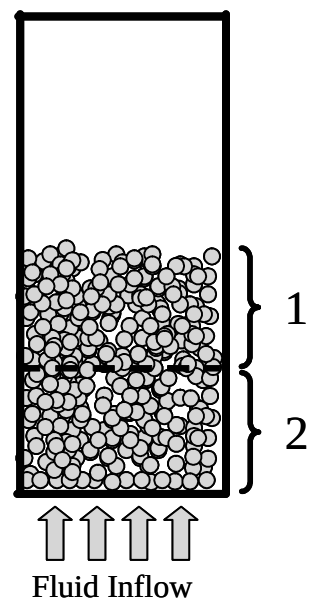

Fig. 7.9 *Method used to divide particles into families for calculation of mixing index.*

where n_1 is the number particles in family 1, n_2 is the number of particles in family 2, and y_i is the height of the ith particle. For a system that remains segregated, the mixing index has a value of 3, while a perfectly mixed system exhibits a mixing index of 1. In Figure 7.10 the evolution of the mixing index over time is shown for several different levels of cohesion using the square-well model. Figure 7.11 displays similar results for simulations using the Hamaker model, with input parameters mapped according to the escape-velocity criterion. These figures also show the escape velocity ($v_{ij,esc}$) associated with each level of cohesion. As a rough estimate, the mapping does appear to provide a good common ground between the two models.

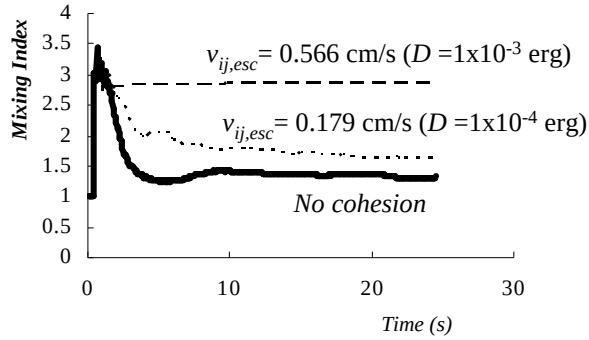

Fig. 7.10 *Evolution of mixing index in time for simulations using the square-well cohesion model.*

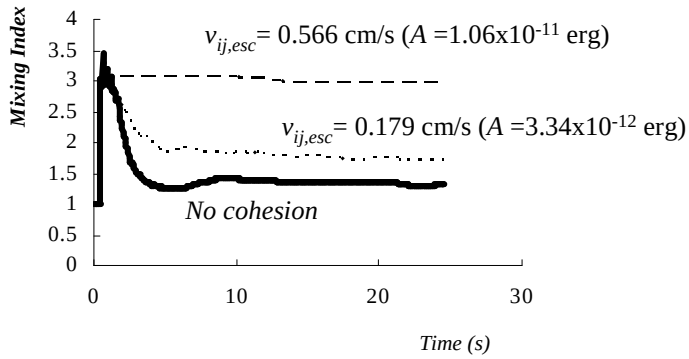

Fig. 7.11 *Evolution of mixing index in time for simulations using the Hamaker model.*

7.2.3 Quantitative Comparison: Minimum Fluidization Velocity

Experimental results have shown that cohesive forces can lead to an increase in the minimum fluidization velocity [11-14]. In the current section, the effects of cohesion are examined in terms of its influence on the three velocities associated with minimum fluidization defined previously (Section 6.4), namely the theoretical minimum fluidization velocity ($U_{mf,th}$), the incipient fluidization velocity ($U_{mf,in}$) and the defluidization velocity ($U_{mf,df}$). Both the square-well model and the Hamaker model are used to simulate defluidization and fluidization curves, with parameters chosen such that both models map to the same escape velocity. The procedure

employed in these simulations is the same as described in Section 6.4. Namely, the fluidized bed starts in the bubbling state and the defluidization cycle is implemented first, before the fluidization cycle.

The effects of cohesion on the defluidization velocity, theoretical minimum fluidization velocity, and incipient fluidization velocity are displayed in Figures 7.12-7.14, respectively, for simulations using both the Hamaker model and the square-well model. The simulation parameters outlined in Table 6.2 were used in all of these simulations. For each model, three levels of cohesion were implemented using the parameters in Table 7.1. In order to gauge the effectiveness of the mapping, results from both models are presented on the same plots as a function of the escape velocity. Three replicates were run for each parameter set and the standard deviation of the replicates is represented by error bars at each data point. The simulation of more replicates does not lead to a significant decrease in this standard deviation.

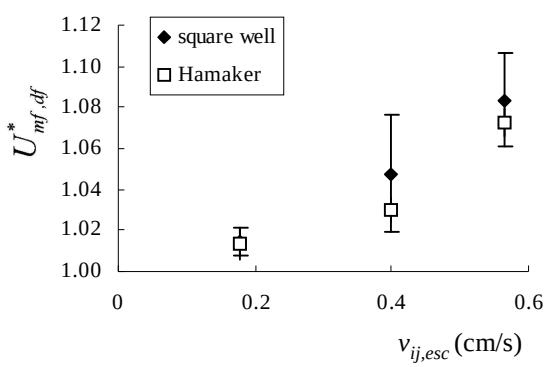

Fig. 7.12 *Defluidization velocity as a function of cohesive forces for both the Hamaker and square-well models.*

The parameter mapping works well for the defluidization velocity, as is displayed in Figure 7.12, with results from both cohesion models showing reasonable agreement at each escape velocity. Furthermore, experimental efforts by Wright and Raper [11, 14] and simulation efforts by Mikami et al. [15] and Kobayashi et al. [16]

all examined the behavior of the defluidization velocity (as defined in this work in Section 6.4). In each of these efforts an increase in the defluidization velocity was observed as the magnitude of cohesion is increased, which is consistent with the simulation results presented here (since an increase in escape velocity corresponds to an increase in the level of cohesion, as prescribed by *A* and *D*).

Results from the increasing-velocity branch of the fluidization curve are presented in Figures 7.13-7.14. These plots further illustrate the effectiveness of the escape-velocity mapping. However, the mapping exhibits some limitations at the higher levels of cohesion. A comparison of these results to previous experimental results, however, is not straightforward. A review of both experimental and simulation studies reveals some ambiguity in the observed behavior of those critical velocities. The general increase in the minimum fluidization velocity with an increase in the magnitude of cohesion is consistent with many experimental studies [11-14] and simulation studies [15, 16]. These results agree with the results shown here. Unfortunately, very few efforts have provided enough detail to determine which critical velocity has been measured (theoretical or incipient). Therefore, it is difficult to comment on the validity of the results presented here for the theoretical minimum fluidization (Figure 7.13) and incipient fluidization (7.14).

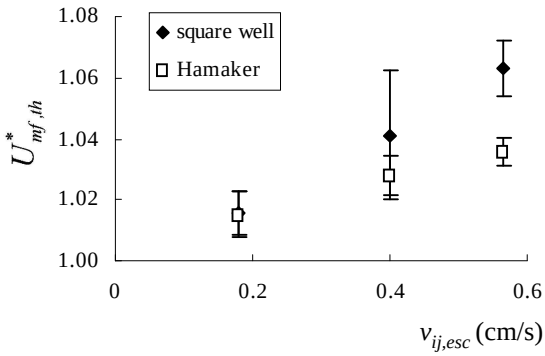

***Fig 7.13**. Theoretical minimum fluidization velocity as a function of cohesive force for both cohesion models.*

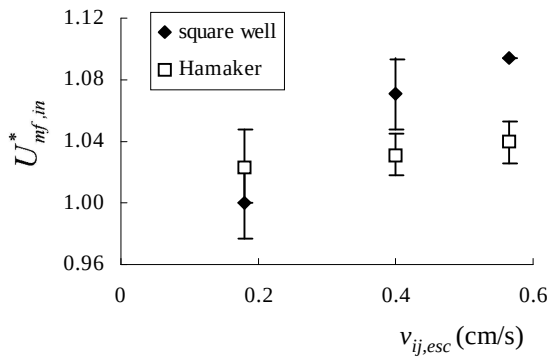

***Fig 7.14**. Incipient minimum fluidization velocity as a function of cohesive forces for both cohesion models.*

7.2.4 Quantitative Comparison: Average Particle Movement

To further evaluate the effectiveness of the escape-velocity mapping, particle displacement over a set time interval is examined, similar to that used by Wang and Rhodes [17]. An extreme example of small displacement is the plugging and channeling exhibited by Type C particles. On the other end of the spectrum is a vigorous, bubbling fluidization, in which net particle displacement is relatively high. The level of particle displacement is calculated by recording the distance moved by each particle (Δl_i) over the time increment $t_1 - t_2$:

$$\Delta l_i = \sqrt{(x_{t1} - x_{t2})^2 + (y_{t1} - y_{t2})^2} \tag{7.10}$$

where x_{t1} and y_{t1} are the *x*- and *y*-positions of a given particle at time t_1, and x_{t2} and y_{t2} are the *x*- and *y*-positions of a given particle at time t_2. This quantity is then averaged over every particle in the simulation to obtain the average particle movement (Δl_{avg}) in the given time increment.

$$\Delta l_{avg} = \frac{1}{n}\sum_{i=1}^{n} \Delta l_i \tag{7.11}$$

where *n* is the number of particles in the simulation. The values reported in Figure 7.15 are also averaged over 30 temporal data collection intervals that each lasts 0.3 seconds. These results were taken using the simulation parameters presented in Table 6.2 and the cohesion parameters presented in Table 7.1. A time interval of 0.25 seconds was used to calculate the average movement and each simulation employed a constant superficial velocity of 77 cm/s. Furthermore, the system was allowed to come to a steady state before the particle mobility was measured and three replicates were run for each case in order to obtain an estimate of the error. Figure 7.16 illustrates how the values of the average particle movement show good agreement at similar escape velocities, regardless of which cohesion model is used.

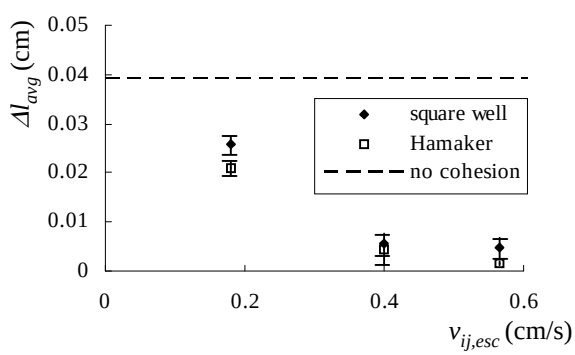

Fig. 7.15 *Average particle movement with both cohesion models compared to escape velocity.*

7.3 Effect of length scale

One drawback of the escape-velocity mapping is that it does not account for the length scale of the square-well and Hamaker models. With regard to the square-well model, changes in the well-width to particle radius ratio (r_{outer}/r_{inner}) will not affect the escape velocity for head-on (normal) collisions. However, changes in r_{outer}/r_{inner} will affect the nature of the collision for oblique impacts, presenting an obvious limitation of the escape-velocity mapping as it is used with the square-well model. With regard to the Hamaker model, changes in the cutoff distance (H_{cut}) will affect the head-on escape velocity, however the primary effect of H_{cut} is to alter the magnitude of the constant γ associated with surface adhesion force (equation 6.38). Because H_{cut} is so small, it is expected that changes in H_{cut} do not significantly affect oblique collisions. Two approaches are taken to assess the effect of the characteristic length scale in each model. First, two-particle simulations are used to directly predict the effect calculating the escape velocity for various angles of approach (i.e., oblique collisions). Second, simulations using the square-well model are run with various values for r_{outer}/r_{inner}, and simulations with the Hamaker model are run using various values for H_{cut}. The results of these simulations are then compared on the basis of predicted defluidization velocity and average particle movement.

Figure 7.16 illustrates the configuration used to determine the effect of oblique collisions on the escape velocity. The escape velocity was measured as the minimum relative normal velocity needed to escape agglomeration with the relative normal velocity measured just before the first cohesive interaction.

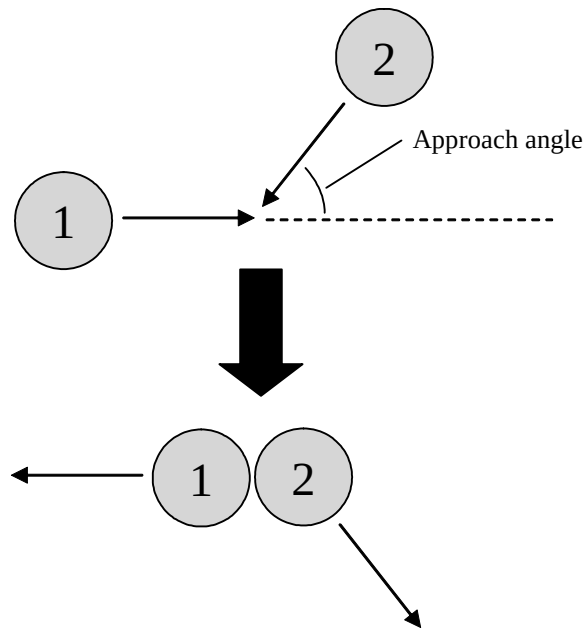

Fig. 7.16 *Layout of two-particle simulations used to determine effect of square-well width on escape velocity.*

Figure 7.17 reports the escape velocity in simulations using the square-well model with two different well depths and three different values of r_{outer}/r_{inner}. At larger r_{outer}/r_{inner}, the escape velocity varies somewhat, but overall the approach angle has little effect on the escape velocity except at very high approach angles. Similar results are obtained for the Hamaker model (with varied H_{cut}) as displayed in Figure 7.18. As stated earlier, varying H_{cut} will affect the head-on escape velocity, so when varying H_{cut} the Hamaker constant was also varied in order to achieve the same

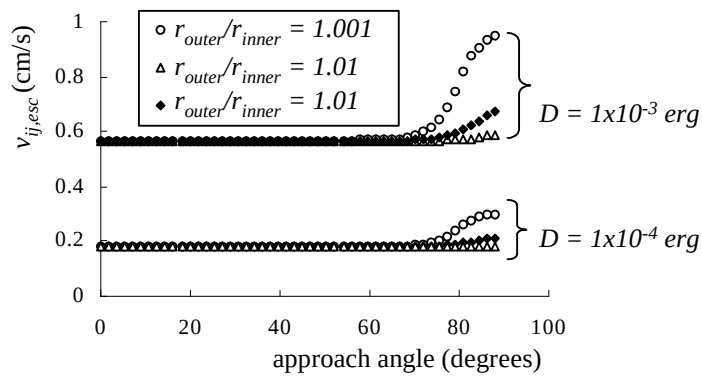

Fig. 7.17 *Square-Well model: Effect of approach angle on the escape velocity.*

escape velocity for the head-on case. The parameters used in this plot are summarized in Table 7.2. While the Hamaker model shows a significant variation in the escape velocity as the approach angle is increased (similar to the square-well

Table 7.2 *Parameter values used in two-particle investigation of oblique collisions.*

H_{cut} (m)	A (erg)	$v_{ij,esc}$ (cm/s)
4.0 x 10^{-9}	1.04 x 10^{-9}	0.566
4.0 x 10^{-10}	1.06 x 10^{-11}	0.566
4.0 x 10^{-11}	1.06 x 10^{-13}	0.566
4.0 x 10^{-9}	3.15 x 10^{-10}	0.179
4.0 x 10^{-10}	3.34 x 10^{-12}	0.179
4.0 x 10^{-11}	3.36 x 10^{-14}	0.179

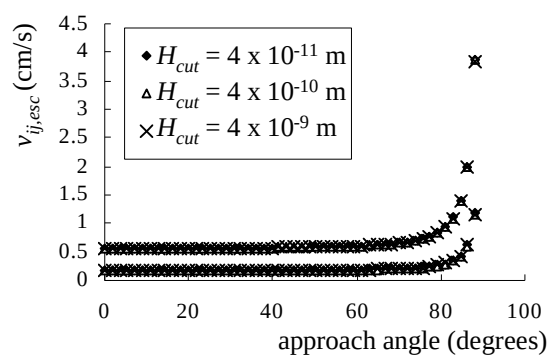

Fig. 7.18 *Hamaker model: Effect of approach angle on the escape velocity.*

model), the escape velocity mapping accounts for this dependency. Combinations of A and H_{cut} that result in the same escape velocity for the head-on case (zero approach angle), continue to predict the same escape velocity at all approach angles. For both

cohesion models, the escape velocity deviates significantly from the "head-on" case only at very high collision angles. This deviation is partly due to the increased effects of friction as the particles develop a larger component of tangential relative velocity at higher approach angles. Two-particle simulations run without friction (results not shown here) displayed a slight decrease in the escape velocity at very large approach angles.

Figure 7.19 shows the effect of r_{outer}/r_{inner} on average particle movement for two different square-well depths. Although there is some variation in the square-well results as r_{outer}/r_{inner} is varied, the results at all r_{outer}/r_{inner} are relatively close for each escape velocity.

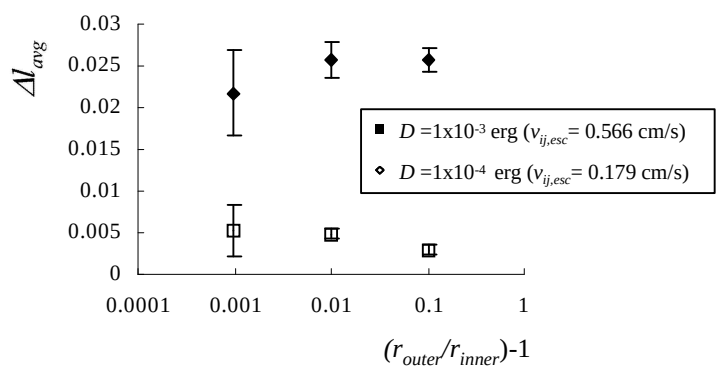

Fig. 7.19 *Square-Well model: Effect of the r_{outer}/r_{inner} on the average particle movement.*

The effects of r_{outer}/r_{inner} on the defluidization velocity are examined in Figure 7.20. At both well depths, the defluidization velocity is relatively close for the two larger r_{outer}/r_{inner}. For the smallest r_{outer}/r_{inner}, however, the defluidization velocity changes significantly. Changing r_{outer}/r_{inner} from 1.01 to 1.001 has a clear effect on the defluidization velocity.

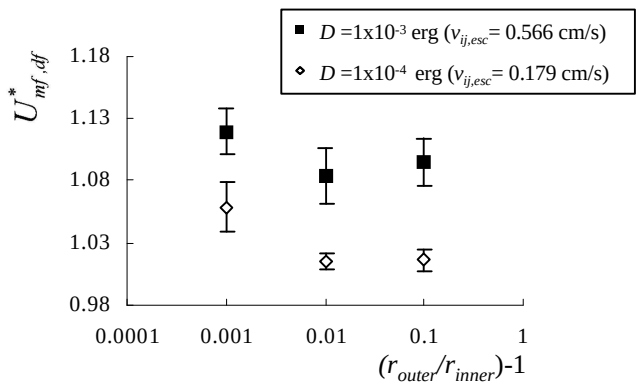

Fig. 7.20 *Square-Well model: Effect of the r_{outer}/r_{inner} on the defluidization velocity for two well widths.*

Figure 7.21 displays the effect of H_{cut} on the predicted defluidization velocity in simulations that utilize the Hamaker model. For reference, the results of simulations with higher and lower levels of cohesion are also presented. These results indicate the H_{cut} has little effect on the predicted defluidization velocity as long as the Hamaker parameters predict equivalent head-on escape velocities.

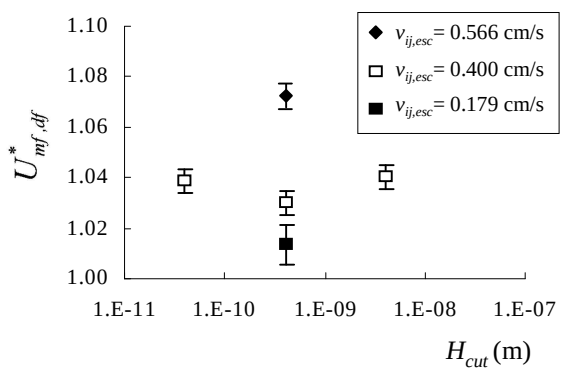

Fig. 7.21 *Hamaker model: Effect of H_{cut} on the defluidization velocity.*

7.4 Summary of Efforts to Develop Mapping Between Cohesion Models

Several different methods have been considered as a possible means to map cohesion parameter values from the Hamaker model parameters to equivalent square-well model to parameters. The escape velocity in a two-particle, head-on collision

appears to provide a good common ground. The effectiveness of the mapping was assessed by examining defluidization behavior, mixing behavior, fluidization velocities and average particle movement. When possible, simulation results from both models were also compared with experimental trends.

A possible drawback of this mapping method is that it does not include the length scale associated with the cohesion model. For the square-well model, the length scale can be varied by changing the width of the square well. The average particle movement in simulations using the square-well potential does not change significantly as the square-well length scale is varied, however the defluidization velocity does increase significantly for well a width to inner radius ratio close to unity (r_{outer}/r_{inner} =1.001). These results indicate that the applicability of this mapping may be limited to larger well width to inner radius ratios (r_{outer}/r_{inner} >1.001). The characteristic length associated with the Hamaker model is controlled by the cutoff distance (H_{cut}). Two-particle simulations show that sets of Hamaker parameters (A and H_{cut}) that produce equivalent escape velocities for the head-on case, exhibit the same escape velocity for all approach angles. This indicates that the escape velocity can successfully account for variations in the length scale of the Hamaker model. Furthermore, predictions of the defluidization velocity do not vary significantly as H_{cut} is varied with simulations using mapped Hamaker parameters.

7.5 References

1. J. P. K. Seville, Processing of Particulate Solids, Blackie Academic and Professional, London, 1997.
2. F. J. Keller, W. E. Gettys, and M. J. Skove, Physics, McGraw-Hill, 1993.
3. D. Geldart, Types of Gas Fluidization, *Powder Technology* 7 (1973) 285-292.

4. M. J. Rhodes, X. S. Wang, M. Nguyen, P. Stewart, and K Liffman, Onset of cohesive behavior in gas fluidized beds: a numerical study using DEM simulation, *Chemical Engineering Science* 56 (2001) 4433-4438.
5. M. Ye, M. A. van der Hoef, and J. A. M. Kuipers, A numerical study of fluidization behavior of Geldart A particles using a discrete particle model, *Powder Technology* 139 (2004) 129.
6. O. Molerus, Interpretation of Geldart's type A, B, C and D powders by taking into account interparticle cohesion forces, *Powder Technology* 33 (1982) 81.
7. L. J. McLaughlin and M. J. Rhodes, Prediction of fluidized bed behaviour in the presence of liquid bridges, *Powder Technology* 114 (2001) 213.
8. M. Rhodes, Fluidization of particles by fluids, http://www.erpt.org/012Q/rhod-04.htm (2001).
9. S. M. P. Mutsers and K. Rietema, The effect of interparticle forces on the expansion of a homogeneous gas-fluidized bed, *Powder Technology* 18 (1977) 239.
10. S. Y. Wu and J. Baeyens, Segregation by size difference in gas fluidized beds, *Powder Technology* 98 (1998) 139.
11. P. C. Wright and J. A. Raper, Examination of dispersed liquid-phase three-phase fluidized beds: Part 1 Non-porous, uniform particle systems, *Powder Technology* 97 (1998) 208.
12. J. P. K. Seville and R. Clift, The effect of thin liquid layers on fluidization characteristics, *Powder Technology* 37 (1984) 117.
13. M. L. Passos and A. S. Mujumdar, Effect of cohesive forces on fluidized and spouted beds of wet particles, *Powder Technology* 110 (2000) 222.
14. P. C. Wright and J. A. Raper, Role of liquid bridge forces in cohesive fluidization, *Transactions of the Institution of Chemical Engineers* 76 (1998) 753.
15. T. Mikami, H. Kamiya, and M. Horio, Numerical simulation of cohesive powder behavior in a fluidized bed, *Chemical Engineering Science* 53 (10) (1998) 1927.
16. T. Kobayashi, T. Mukai, T. Kawaguchi, T. Tanaka, and Y. Tsuji, DEM analysis of flow patterns of Geldart's group A particles in fluidized bed, *World Congress on Particle Technology 4, Sydney, Australia* (2003)
17. X. S. Wang and M. J. Rhodes, Mechanistic study of defluidization by numerical simulation, *Chemical Engineering Science* 59 (2004) 215.

Chapter 8 Hysteresis in Fluidized Beds of Geldart Type A Particles

8.1 Relevant Efforts

As mentioned previously, systems with relatively high levels of cohesion are unable to fluidize in a conventional manner. Instead, the bed is characterized by the formation of plugs and channels. Moderate levels of cohesion may have more subtle, yet significant, effects on fluidized-bed operation. For example, one phenomenon that is sometimes attributed to mild cohesion is a pressure overshoot that can occur during the fluidization process (which is associated with the hysteresis observed between fluidization and defluidization cycles). A better understanding of this phenomenon, which is detailed below, is the target of the current effort.

Tsinontides and Jackson [1] provide a detailed description of the defluidization-fluidization cycle in their investigation into the range of stable, non-bubbling fluidization exhibited by small, light particles (Geldart Type A). Their effort includes experimental measurements and a physically-based model. In the experiments, the fluidized bed started in a bubbling state. The superficial velocity (U_s) was decreased in stepwise increments to take the bed through a defluidization cycle into the packed state. The superficial velocity was then increased beyond the point of minimum fluidization. Their experimental results exhibit a pressure overshoot between the theoretical ($U_{mf,th}$) and incipient ($U_{mf,in}$) minimum fluidization velocities in which the pressure drop (ΔP) exceeds the total particle weight (W) normalized by the bed cross-sectional area (A_b). These trends are illustrated in Figure 8.1.

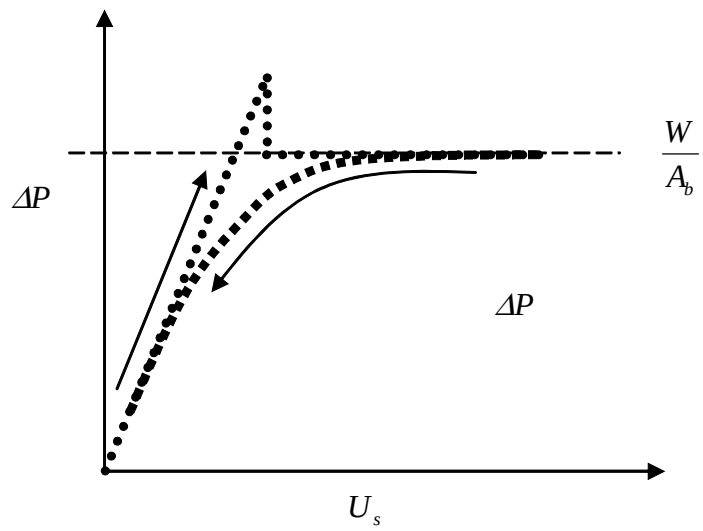

Fig. 8.1 *Sketch of fluidization-defluidization cycle showing pressure overshoot.*

Tsinontides and Jackson [1] also examined trends in bed expansion during the defluidization-fluidization cycles. A packed bed structure is observed for all superficial velocities below the incipient fluidization velocity, as illustrated in Figure 8.2. Once the incipient fluidization velocity is reached, the packed bed expands to a fluidized bed rapidly before showing gradual expansion as the gas velocity is increased further. As the gas velocity is decreased from the bubbling state, the bed height exhibits a hysteresis with the defluidization height being higher than the fluidization height at each gas velocity.

As sketched in Figure 8.3, the experimental results of Tsinontides and Jackson [1] reveal that hysteresis becomes more pronounced as the width of the fluidized bed is decreased, indicating that frictional interactions with the sidewalls may be an important mechanism in the hysteresis. (The area of the sidewall in contact with the particle bed relative to the total particle weight increases as the bed gets smaller, whereas the magnitude of cohesive effects does not change relative to the total

particle weight as long as the bed height is kept constant). However, their results also show the hysteresis is more pronounced when moist air is used, indicating that cohesive particle interactions may be an important cause of the hysteresis phenomenon. The final conclusion of the authors is that the hysteresis is due to some combination of effects from particle-sidewall friction and particle cohesion. They further note that their inability to independently control frictional and cohesive effects within their experimental system restricted the level of insight they could achieve into this phenomemon.

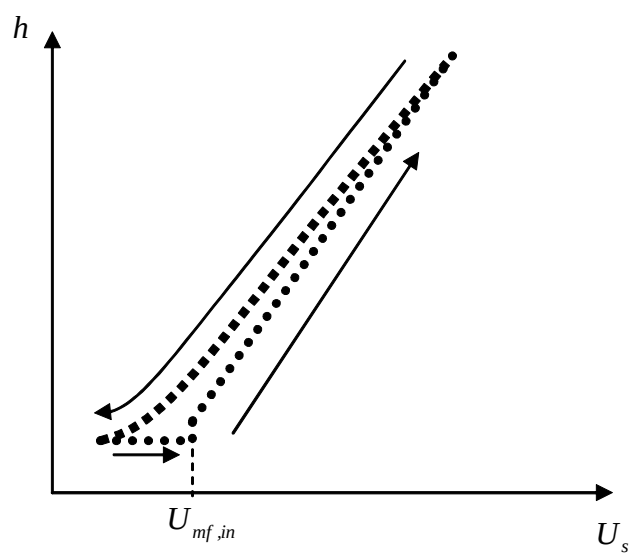

Fig. 8.2 *Sketch of bed expansion behavior during defluidization-fluidization cycle.*

Jackson [2] further elaborated on the experimental observations of Tsinontides and Jackson [1] by presenting a one-dimensional force balance model for the defluidization-fluidization cycle in fluidized beds:

$$\frac{d\sigma_s}{dy} \pm \frac{4}{D_{bed}} \mu j \sigma_s = \rho_s \varepsilon_g g - \beta(\varepsilon_g) \frac{U_s}{1-\varepsilon_g} \qquad (8.1)$$

where y is the axial direction, σ_s is the cross-sectional average of the yy-component of stress associated with enduring particle-particle contacts, D_{bed} is the width of the fluidized bed, μ is the friction coefficient between particles and the walls, j is the Janssen constant (a proportionality constant to relate the normal stress on the wall with the friction force in the vertical direction), ρ_s is the particle density, ε_g is the void fraction, β is the drag coefficient, and U_s is the superficial gas velocity.

This model, which does not incorporate cohesive effects, predicts a pressure overshoot and a jump in bed height at minimum fluidization. The pressure overshoot is attributed to frictional interactions with the walls which are incorporated by the second term on the left-hand side of equation 8.1. This term is negative for fluidization and positive for defluidization. Furthermore, the dependence of the pressure overshoot on bed diameter is inherent in this friction term (overshoot decreases as D_{bed} increases). Subsequent experimental investigations have yielded similar conclusions regarding the relative importance of wall friction [3,4].

Experimental results by Srivastava and Sundaresan [3] also exhibit an increase in the pressure overshoot as the bed diameter is decreased. The experimental results agree well with the one-dimensional model developed by Jackson [2] in which the particle-wall friction coefficient is used as a fitted parameter. As stated previously, this model does not account for cohesive interactions and attributes the pressure overshoot exclusively to frictional interactions with the sidewalls.

Experimental efforts by Loezos *et al.* [4] also indicate an increase in the pressure overshoot as the fluidized bed width is decreased. This effect is again captured by the non-cohesive model developed by Jackson [2]. The data further shows that smaller

particles (which have a relatively high cohesive-force-to-weight-ratio) exhibit a larger pressure overshoot than the larger particles. Because a different set of fitting parameters is used for each type of particle, this model is able to account for this dependency without addressing cohesion explicitly. Based on their results, Loezos *et al.* conclude that frictional interactions between particles and the walls are the primary reason for the pressure overshoot.

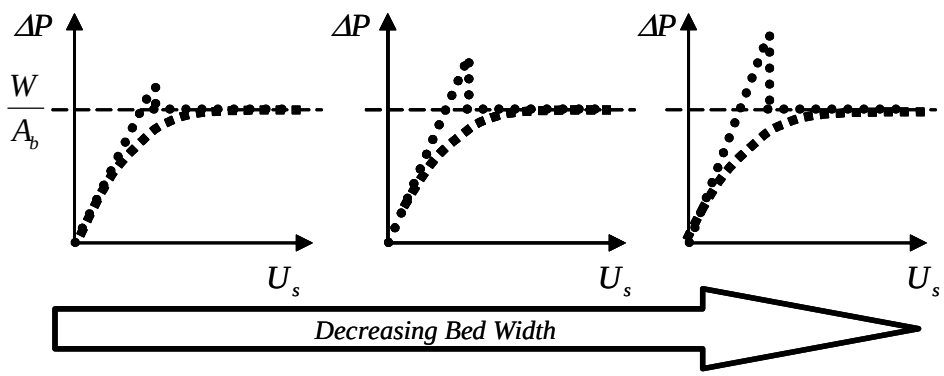

Fig. 8.3 *Effect of bed width on the hysteresis in the fluidization-defluidization cycle observed experimentally.*

The aim of the current work is to better understand the *relative* importance of the various mechanisms associated with the pressure overshoot. More specifically, the experimental efforts described previously are limited in their ability to independently control and measure the contributions to the pressure overshoot (e.g., particle friction with walls and particle cohesive force with distributor plate). Two benefits of an Eulerian-Lagrangian simulation are (i) the ability to independently control levels of cohesion and friction (i.e., can turn these mechanisms "on" and "off") and (ii) to compare the relative magnitude of each contributing force. Correspondingly, Eulerian-Lagrangian simulations of defluidization-fluidization cycles were carried out to further explore the pressure-overshoot phenomenon.

8.2 Defluidization-Fluidization Cycle via Square-Well Model

Simulations were run using the square-well model with the parameters presented in Table 6.2, unless otherwise stated. The procedure for each simulation was to start at a superficial velocity large enough to produce bubbling, ramp the gas velocity down to the packed bed state, and then ramp the velocity back up to the bubbling state. For simplicity, the results presented here only show the fluidization cycle (increasing superficial velocity), because the pressure overshoot is not observed during the defluidization cycle. Beds of different diameters were simulated, and the number of particles is varied to keep the bed height constant in all simulations (which mimics the previous experiments [1,3,4]. The data in these plots represents the average of three replicate runs. Error bars are based on the standard deviation in the results. Large error bars on the right side of each plot are due to the bubbling behavior displayed at higher superficial velocities. Figure 8.4 illustrates the effect of cohesion predicted by the square-well model. Simulations run without cohesion (Figure 8.4a) show essentially no pressure overshoot, while the addition of cohesion (Figure 8.4b) appears to give rise to a significant pressure overshoot. These results indicate that cohesion is a factor that leads to pressure overshoot.

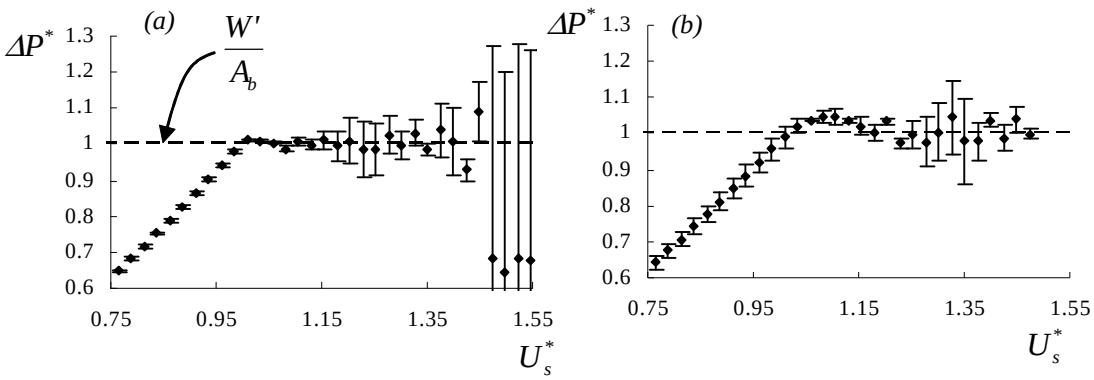

Fig. 8.4 *Square-well model: Normalized fluidization curve (a) without and (b) with cohesion ($D=5x10^{-4}$ erg).*

To gauge the importance of frictional effects, simulations were run with a much larger coefficient of friction (μ = 1.0) than that used for Figure 8.4 (μ = 0.3). No cohesive forces were implemented. These results, as displayed in Figure 8.5, indicate that an increase in the level of friction does not appear to result in a significant pressure overshoot. Collectively, these results suggest that cohesive forces are not only significant, but required, for the pressure overshoot at the conditions examined.

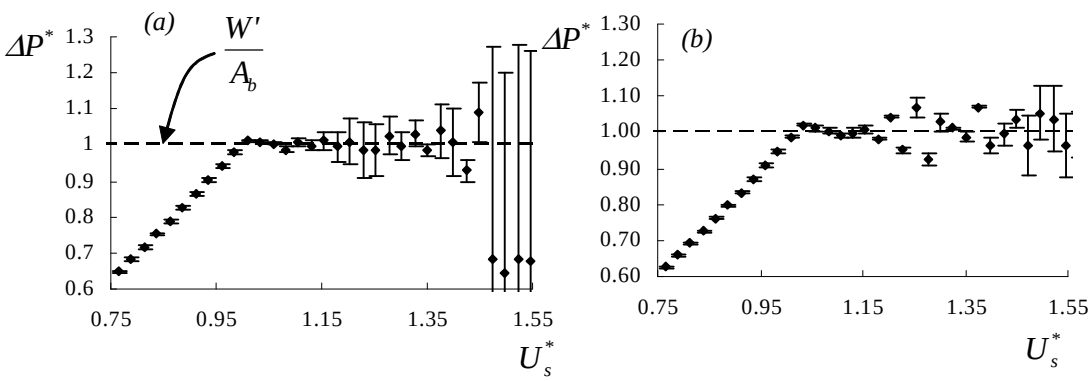

Fig. 8.5 *Square-Well model: Fluidization cycle with no cohesion (D=0) (a) typical friction (μ = 0.3) and (b) a high level of friction (μ = 1.0).*

A more detailed understanding of effects of cohesion on pressure overshoot is possible by considering the three types of cohesive interactions: particle-particle cohesion, particle-sidewall cohesion, and particle-distributor-plate cohesion. In order to investigate the significance of each cohesion type, simulations were run in which each interaction type is excluded. These results are presented in Figure 8.6. When comparing these three plots, the pressure overshoot is lowest in simulations that exclude particle-particle cohesion (Figure 8.6a). This finding indicates that particle-particle cohesive interactions have the strongest influence on the pressure overshoot out of the three interactions.

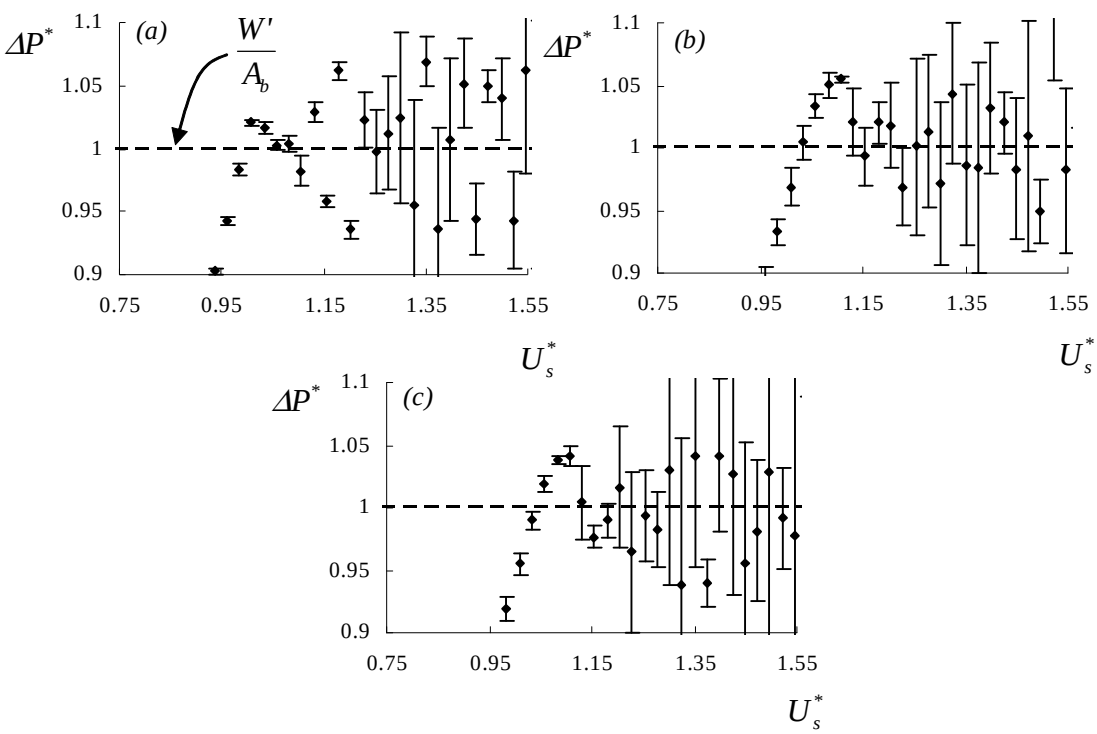

Fig 8.6. *Square-Well model: Fluidization curves for cases of (a) no particle-particle cohesion, (b) no particle- sidewall cohesion and (c) no particle-distributor-plate cohesion ($D=5x10^{-4}$ erg).*

In the context of a macroscopic force balance in the axial direction over the bed, this result appears counter-intuitive. Cohesive interactions between particles and the distributor introduce an obvious external force on the bed of particles in the axial

direction. Cohesive interactions between particles and the sidewalls enhance frictional interactions, leading to a net external force on the particles in the axial direction. However, it is initially unclear in what manner particle-particle cohesion impacts the force balance.

The effects of particle-particle cohesion on the pressure overshoot are partly due to the manner in which pressure drop is calculated. As described in Section 6.2, the pressure cannot be calculated at the distributor plate, but only at the computational node just above the distributor. Therefore, when particle-particle cohesion is present, the pressure calculated at this node is supporting the particles above it and overcoming cohesive interactions between the supported particles and the particles below the node, as illustrated in Figure 8.7. This leads to a pressure drop beyond that needed to support the weight of the particles above the lowest computational node.

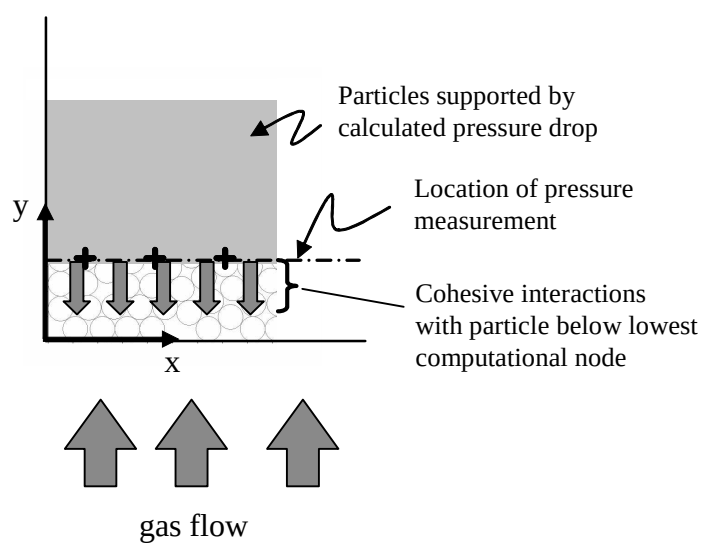

Fig. 8.7 *Possible mechanism for pressure overshot in simulation with no particle-distributor cohesive forces.*

To determine if the effects of particle-particle cohesive forces are an artifact of the numerical methods described in previous paragraph, the net forces on the particles from various mechanisms (e.g. particle-distributor-plate cohesion, particle-

sidewall friction, particle-wall contact forces, particle-fluid forces, and gravity) were examined. Figure 8.8 displays the net force (in the *y*-direction) applied to the particles from the fluid compared to the net gravitational forces applied to the particles (these two forces are comparable in magnitude while the other three listed forces are much smaller). This data is from the same three cases considered in Figure 8.6. The information in these plots applies to all the particles in the fluidized bed and

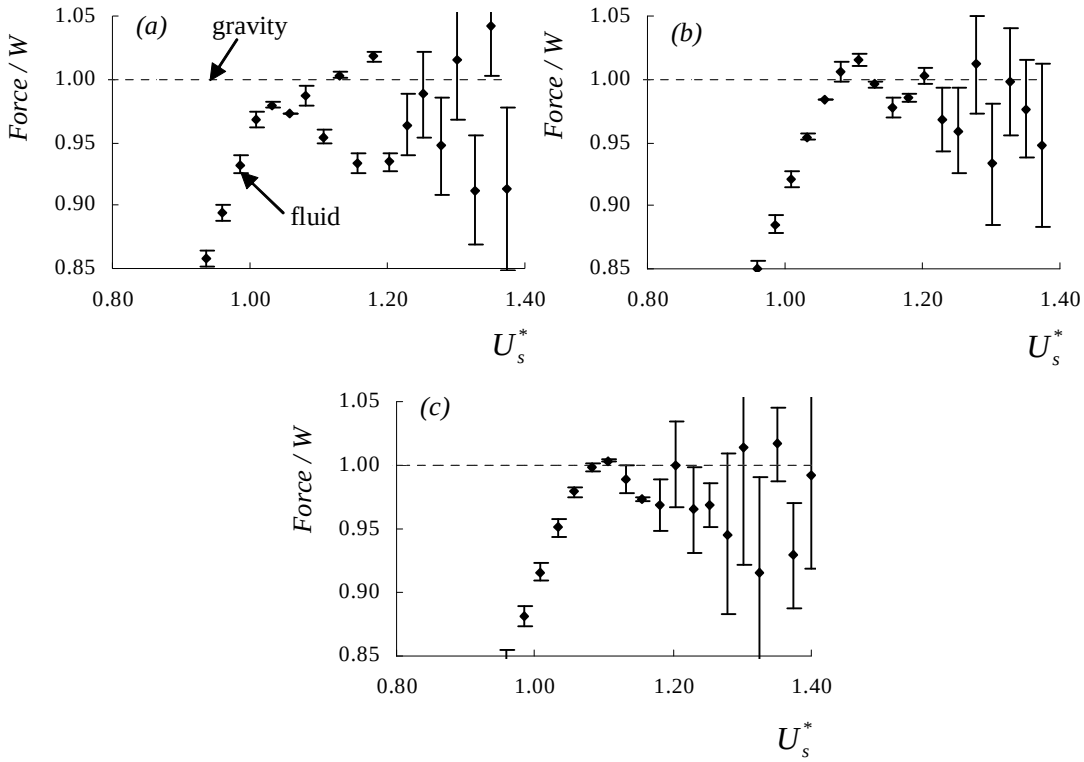

Fig. 8.8 *Square well model: Net forces imposed on the particle from the fluid and gravity for the case of (a) no particle-particle cohesion, (b) no particle-sidewall cohesion, and (c) no particle-distributor cohesion (D=5x10^{-4} erg).*

is not complicated by issues associated with pressure drop measurement (i.e., excluded particles below lowest computational node). In the net-force plots, the only case in which the fluid forces exceed the gravitational forces is for excluded particle-sidewall cohesion (Figure 8.8b). For the case of excluded particle-distributor cohesion (Figure 8.8c), the fluid forces just equal the gravitational forces at the point

of minimum fluidization. Finally, for the case of excluded particle-particle cohesion (Figure 8.8a), the fluid forces are less than the gravitational forces at all times.

Comparing the data in Figures 8.6 and 8.8 leads to two general conclusions. First, the low fluid force in the simulations that exclude particle-particle cohesive forces (Figure 8.8a) illustrates that the effect of particle-particle cohesive forces on the pressure overshoot is not just an artifact of the numerical methods. The exact nature in which these interparticle forces can lead to a net effect on overall bed will be discussed at the end of this section. The second conclusion that can be drawn from these results is that cohesive interactions with the distributor plate have a larger effect on the pressure overshoot than cohesive interactions with the sidewalls. This conclusion is based on the results in Figures 8.8b and 8.8c. The fluid imposes a larger force on the particles in simulations that excluded particle-sidewall cohesive interactions (Figure 8.8b) than in simulations that excluded particle-distributor cohesive interactions (Figure 8.8c). This physical description of the system is further supported by an examination of the net forces observed in a simulation with no cohesive interactions excluded (i.e., all cohesion interactions are present). Figure 8.9 presents the force imposed on the particles from the fluid compared to the net gravitational force for the same operating parameters as used in Figures 8.4b. These results show fluid forces in excess of the gravitational force, consistent with the pressure overshoot displayed in Figure 8.4b. Figure 8.10 reports the net force imposed on the particles by cohesive interactions with the distributor and the net force imposed by frictional interactions with the sidewalls (cohesive interactions with the sidewalls have no *y*-component and only serve to enhance the frictional forces in

the *y*-direction with the sidewalls). Figure 8.10 shows a distinct negative spike in the net force from cohesive interactions with the distributor at the point of incipient fluidization. The frictional forces from the sidewalls (which may be enhanced due to cohesive interactions with the sidewalls) are much smaller in magnitude.

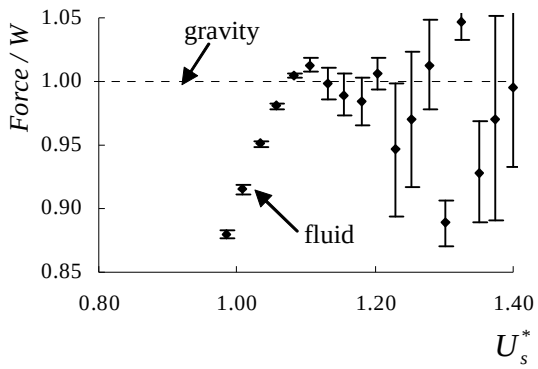

Fig. 8.9 *Square-well model: Net force imposed on the particles by fluid forces and gravity with no excluded cohesive interactions (D=5x10^{-4} erg).*

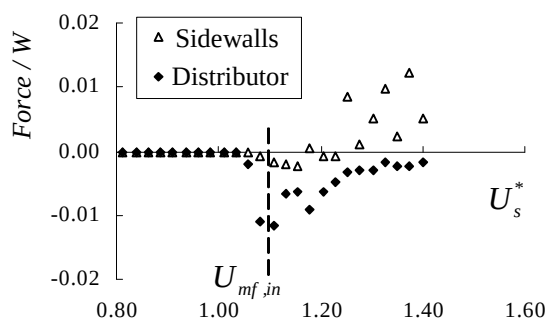

Fig. 8.10 *Square-well model: Net force imposed on the particles by cohesive interactions with the distributor and frictional interactions with the sidewalls (D=5x10^{-4} erg).*

The mechanisms through which particle-particle cohesive forces cause a change in the net fluid forces at incipient fluidization (Figure 8.7a) can be explained in the context of Jackson's one-dimensional, force balance model (Equation 8.1) [2]. According to Jackson, the fluidization process involves a gradual decrease in the normal stress at the base of the bed as the fluid drag force increases with an increase in superficial velocity, as sketched in Figure 8.11. As the superficial velocity

continues to increase, it will eventually reach a critical velocity at which the stress has been decreased to the yield point for dilation. In Jackson's model, the yield stress for dilation is zero and only frictional interactions with the sidewalls oppose bed expansion once the critical velocity is reached. However, Jackson notes that cohesive forces could lead to a nonzero (negative) yield stress. He also notes that the incorporation of such a tensile yield stress would allow the force balance model to predict the pressure overshoot without the inclusion of frictional interactions with the walls. Thus, the effects of particle-particle cohesion on the pressure drop predicted by the discrete-particle simulation are consistent with the model presented by Jackson.

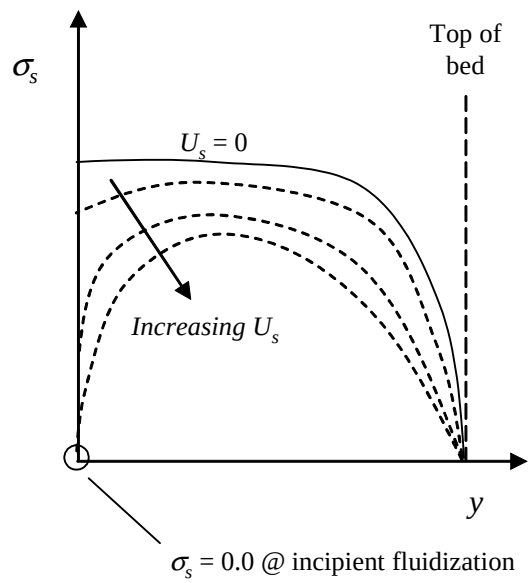

Fig. 8.11 *Sketch of normal stress behavior during fluidization cycle.*

8.3 Defluidization-Fluidization Cycle via Hamaker model

While the results shown in Figures 8.1-8.10 were obtained using the square-well cohesion model, similar simulations can be performed using the Hamaker model

for van der Waals forces. Figure 8.12 shows that the pressure overshoot exists in simulations using the Hamaker model, although it is somewhat less pronounced than the pressure overshoot predicted with the square-well model (Figure 8.4).

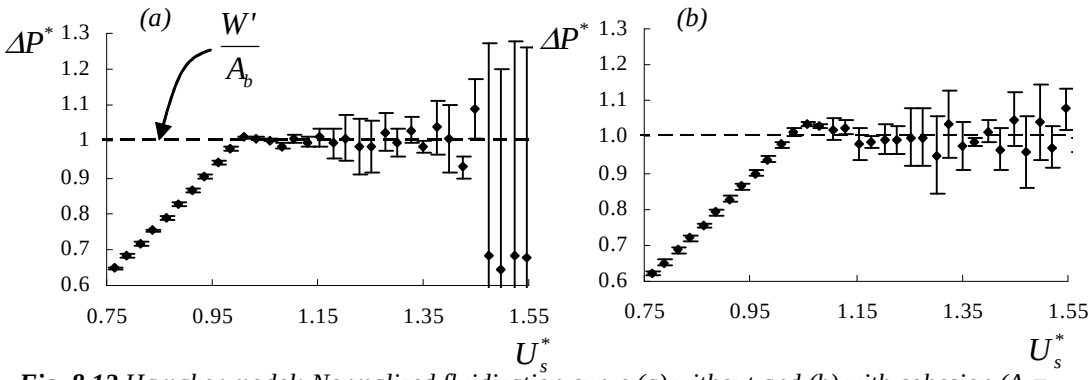

Fig. 8.12 *Hamaker model: Normalized fluidization curve (a) without and (b) with cohesion (A = 7.49 x 10^{-12} erg).*

These results are again examined by excluding certain interactions. Figure 8.13 shows the resulting fluidization curves when particle-particle (Figure 8.13a), particle-sidewall (Figure 8.13b) and particle-distributor (Figure 8.13c) cohesive forces are excluded. Unlike with the square-well model, the pressure overshoot does not change significantly in these plots. However, the duration of the pressure overshoot region is somewhat shorter for the case of excluded particle-particle cohesion (Figure 8.13a).

This system was analyzed further by recording the net forces from various interaction mechanisms as described in the previous section. Figure 8.14 displays the net force imposed on the particles from fluid forces and gravity for the same three cases examined in Figure 8.13. These plots show that the force exerted by the fluid on the particles does not exceed the gravitational forces in any simulation. However, the largest fluid force was attained for the case of excluded particle-distributor cohesion forces. These results indicate that particle-distributor cohesive forces

provide the least resistance to fluidization in simulations using the Hamaker model. Furthermore, it appears that the combination of particle-particle cohesive forces and particle side-wall cohesive forces have a significant effect. This conclusion is further supported by examining the net force from frictional interactions with the sidewalls.

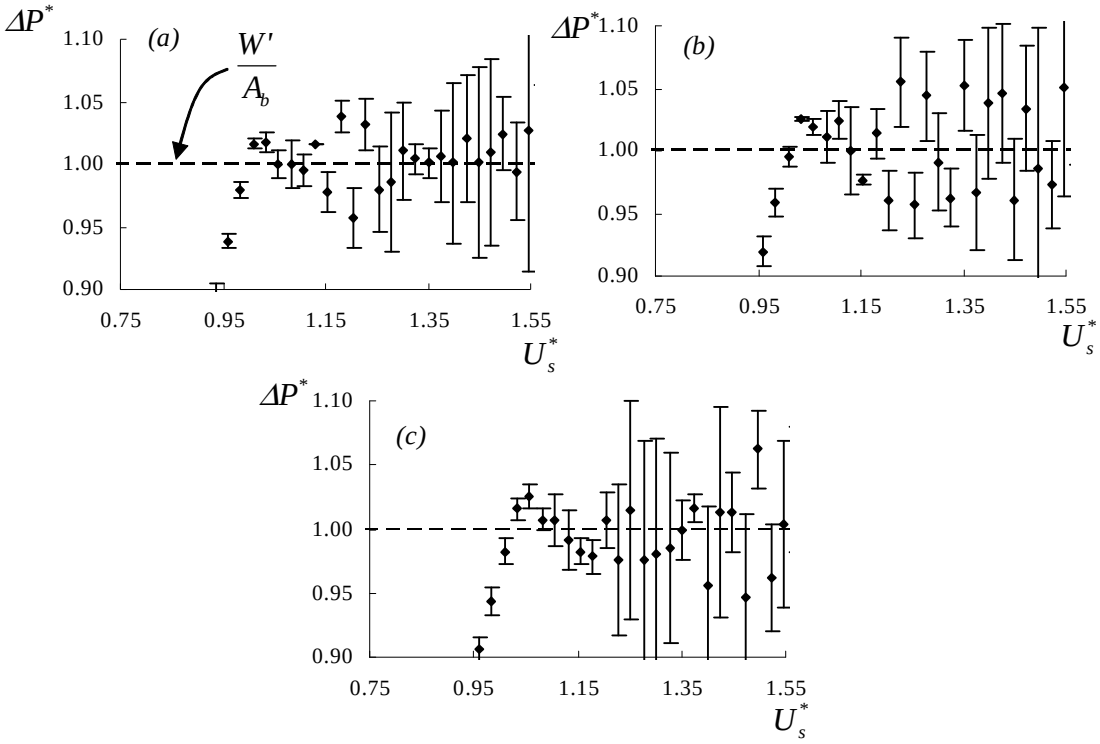

Fig 8.13 *Hamaker model: Fluidization curve for cases of (a) no particle-particle cohesion, (b) no particle sidewall cohesion and (c) no particle-distributor cohesion (A=7.49x10^{-12} erg).*

Figure 8.15a displays the net force imposed on the particles by frictional interactions with the sidewalls. These results show that there is a significant negative force from frictional interactions with the sidewalls near the point of incipient fluidization. Cohesive forces between particles and the distributor plate do not have a significant effect. For the Hamaker model, these forces are actually much larger in magnitude than the frictional forces with the wall. However, due to the nature of the Hamaker model, these forces are only significant when the particles are touching the

distributor plate. Correspondingly, these forces lead to a larger overlap with the distributor plate, which gives rise to a larger repulsive contact force than would have been generated in the absence of cohesive forces. The end result is that the forces between particles and the distributor plate do not produce a net downward force on the bed as shown in Figure 8.15b.

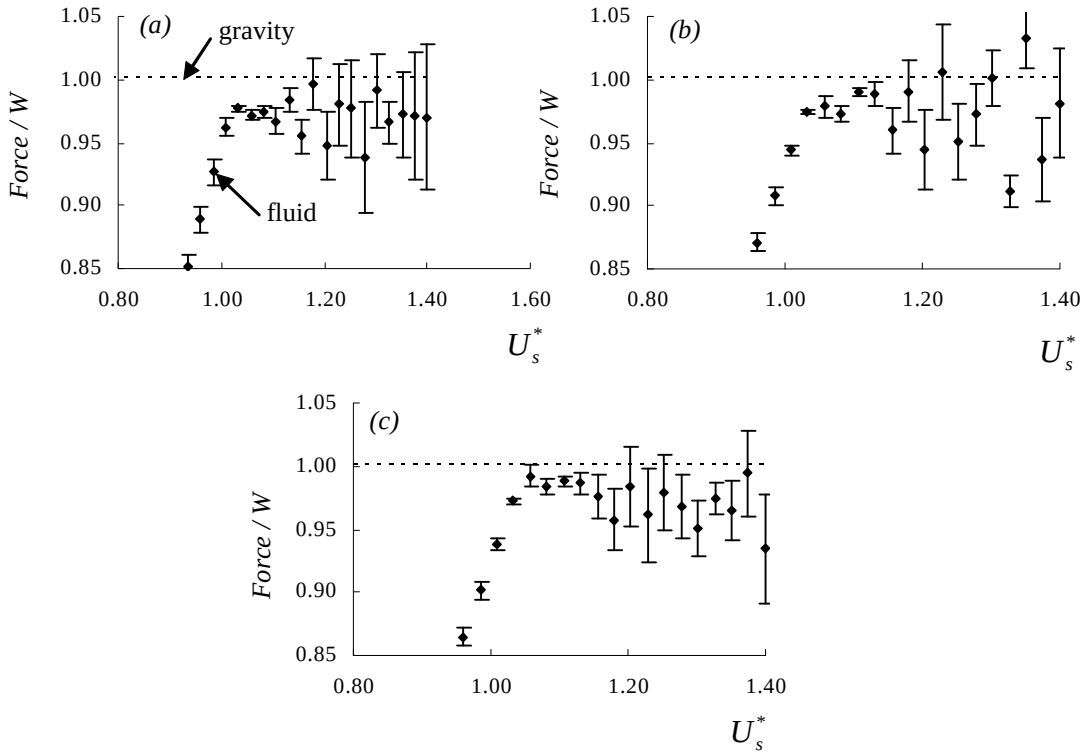

Fig. 8.14 *Hamaker model: Net forces imposed on the particle from the fluid and gravity for the case of (a) no particle-particle cohesion, (b) no particle-sidewall cohesion, and (c) no particle-distributor cohesion (A=7.49x10^{-12} erg).*

While the enduring nature of the contacts in the Hamaker model leads to a minimal net attraction with the distributor plate, it does lead to a significant enhancement of frictional forces with the sidewalls. The Hamaker model keeps particles in direct contact with the sidewalls. Because the particles are in contact with the sidewalls longer, frictional forces have a longer duration. The end result is

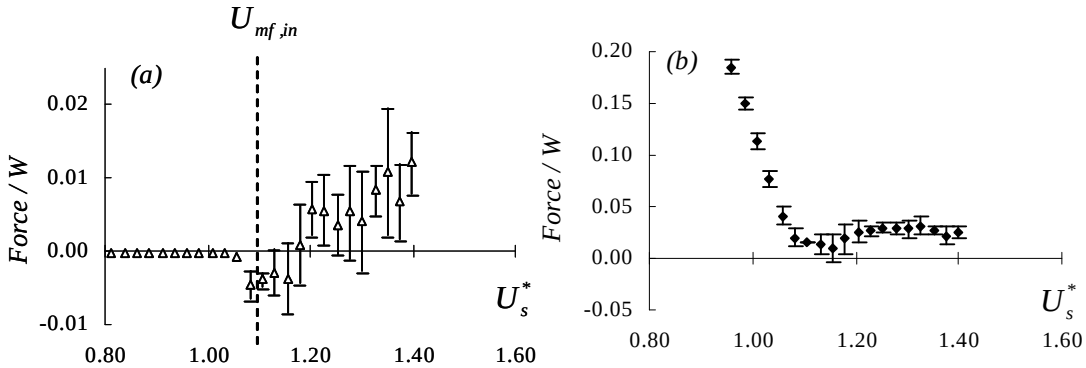

Fig 8.15 *Hamaker model: (a) Net force imposed on the particles from frictional interactions with the sidewalls (b) sum of normal contact force and cohesive force from distributor plate ($A=7.49x10^{-12}$ erg).*

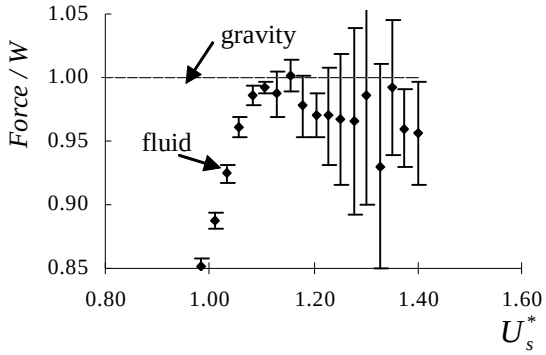

Fig. 8.16 *Hamaker model: Net force imposed on the particles by fluid forces and gravity with no excluded cohesive interactions ($A=7.49x10^{-12}$ erg).*

that the Hamaker model enhances frictional contacts with the sidewalls to a larger extent than the square well model (approximately two times larger in Figure 8.15 than Figure 8.10). The impulsive nature of the square-well model likely leads to a higher frequency of collisional contacts with the walls, but it does not lengthen the duration of each contact and does not affect this mechanism as significantly as the Hamaker model. Although both models are able to predict the pressure overshoot, the responsible mechanism is different based on simulation results.

8.4 Square-Well and Hamaker Model: Effects of bed width on pressure overshoot

A key result in the experimental efforts discussed in Section 8.1 is an increase in the pressure overshoot as the bed width is decreased. Figure 8.17 displays the pressure overshoot at two different bed widths for simulations using the square-well model, and shows that the pressure overshoot does not appear to vary significantly with bed width. Figure 8.18, on the other hand, indicates that the level of pressure overshoot does vary slightly with bed width for simulations using the Hamaker model. Specifically, a decrease in the pressure overshoot is observed as the bed width is increased, which is consistent with previous experiments [1, 3, 4].

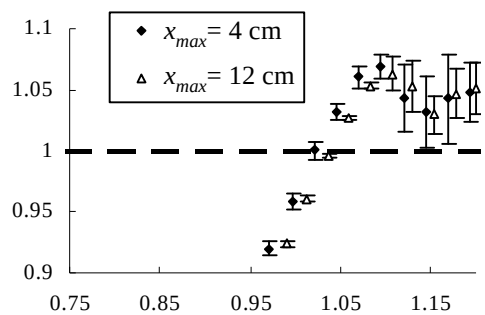

Fig 8.17. *Square-well model: Pressure overshoot fluidized beds with widths of 4cm and 12cm ($D=5.0x10^{-4}$ erg).*

An explanation for the dependency of the pressure overshoot on bed width via the Hamaker model and lack of dependency with the square-well model is possible by considering the mechanisms responsible for pressure overshoot in each model.

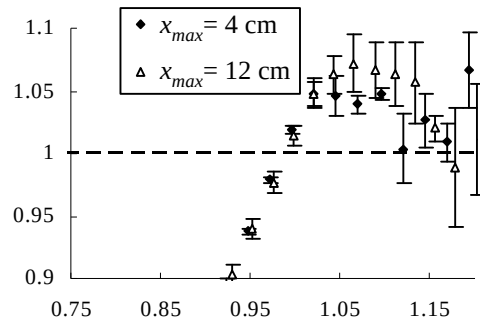

Fig 8.18 *Hamaker model: Pressure overshoot for fluidized beds with widths of 4cm and 12cm ($A=7.49x10^{-12}$ erg).*

As described earlier, cohesion between the particles and distributor plate has a significant effect on the pressure overshoot in simulations employing the square-well potential. This force is plotted in Figure 8.19 for two different bed widths, in which the force is normalized by the total weight of particles in the bed (note that the y-axis sizes are on different scales). The normalized net force from cohesive interactions between particles and the distributor plate does increase slightly as the bed width is increased, but this increase is not large enough to have a significant effect on the overall pressure drop.

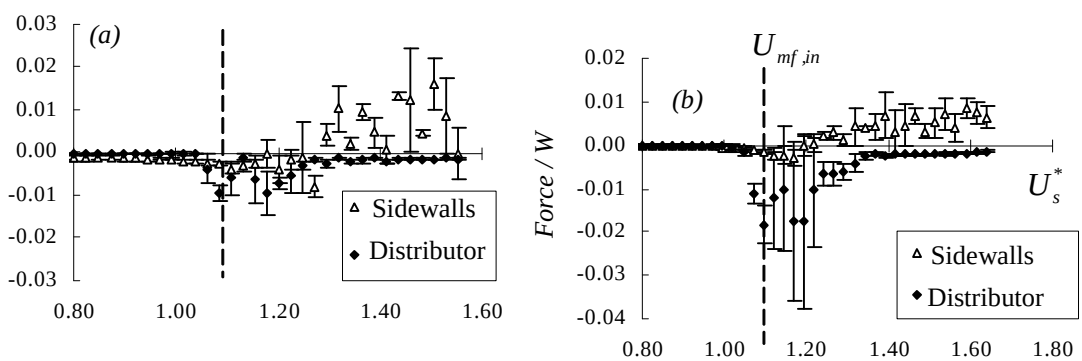

Fig 8.19 *Net force applied to the particles from frictional sidewall interactions and cohesive interactions with the distributor plate when using the square well model for fluidized beds with widths of (a) 4cm and (b) 12 cm.*

Frictional interactions with the sidewalls have a significant effect on the pressure overshoot in simulations using the Hamaker model (see Section 8.3). If the bed height is kept constant as the bed width is varied, the sidewall area (the portion in contact with the particles) will also stay constant (for this two-dimensional simulation). With a constant wall area, the net force from frictional sidewall interactions will also remain constant, even if the total number of particles changes. Figure 8.20 illustrates how the net dimensionless force from frictional side-wall interactions (normalized by the total particle weight) increases as the bed width is decreased. The constant level of frictional force combined with a decreasing number of particles (weight) leads to an increase in the pressure overshoot as the bed width is decreased. This increase in the dimensionless sidewall force is much more significant than the increase in distributor forces observed with the square-well model.

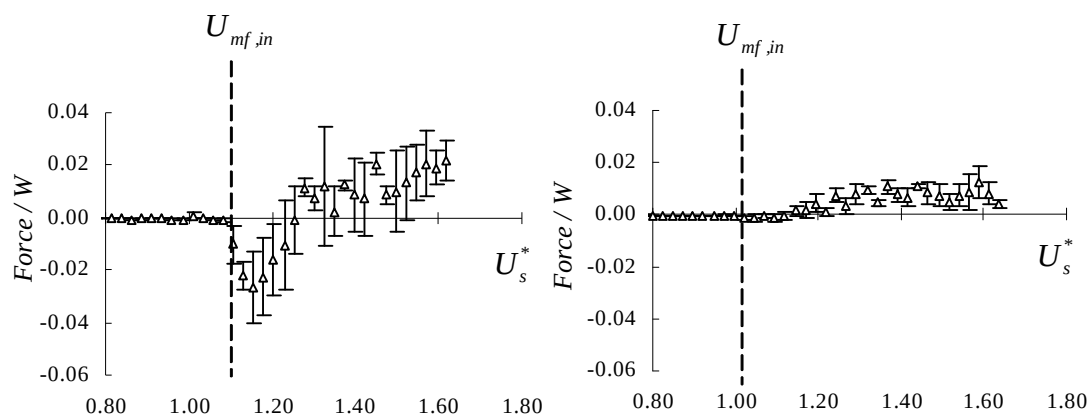

Fig 8.20 *Net force applied to the particles from frictional sidewall interactions when using the Hamaker model for fluidized beds with widths of (a) 4cm and (b) 12 cm.*

It is important to note that these results are specific to a two-dimensional system. In a two-dimensional system of constant bed height, the number of particles decreases directly proportional to the bed radius, while the wall area (sidewall area in

contact with particles) remains constant as the bed radius varies. Therefore the ratio of sidewall area to number of particles will be inversely proportional to the bed width for a two-dimensional system. In a three-dimensional (cylindrical) system (as was used in previous experiments), for a constant bed height, the number of particles will decrease with the square of the bed radius, while the sidewall area will decrease directly proportional to the bed radius. Therefore, the ratio of sidewall area to number of particles will be inversely proportional to the bed radius for a three-dimensional system, just as it is for a two-dimensional system. This ratio behaves the same in both systems despite the fact that the wall area varies with the bed radius for a three-dimensional system and is constant for a two-dimensional system. These findings add to the validity of the simulation results developed here and alleviate concerns that the results may simply be an artifact of the two-dimensional system. Furthermore, these results with the Hamaker model, showing a pressure overshoot that increases as the bed width is decreased, are consistent with the experimental results reviewed in Section 8.1.

In addition to the effects of bed width captured by the Hamaker model, both models capture the effects of increasing levels of cohesion noted by Loezos *et al.* [4]. Their results show that as the particle size is decreased (thus increasing the effects of friction relative to the particle weight) the magnitude of the pressure overshoot increases. Figure 8.21 illustrates the effects of different levels of cohesion predicted by both models, with the level of cohesion represented by the escape velocity introduced in Chapter 7. The model used by Leozos *et al.* [4] was able to predict this

increase in the pressure overshoot, but only by increasing the friction coefficient as the particle size decreased.

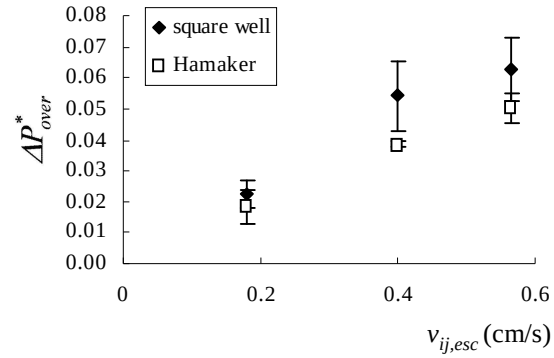

Fig. 8.21 *Effect of increased cohesion levels on the normalized pressure overshoot.*

8.5 Summary of results

The results with the square-well cohesion model and the Hamaker model for van der Waals forces present two different physical pictures of the fluidization cycle. Both models show that particle-particle cohesive forces have a significant effect on the pressure overshoot. Furthermore, the square-well model predicts that cohesive interactions between particles and the distributor plate affect the pressure overshoot. The Hamaker predicts shows that cohesive interactions between particles and the distributor plate have little effect on the pressure overshoot, but that cohesive interactions with the sidewalls do have a significant effect.

The results of the Hamaker model (decreasing pressure overshoot as bed width is increased) are in better agreement with experimental results. Furthermore, the Hamaker model provides a more elaborate description of particle cohesion than the square-well model, leading to more confidence in the results of the Hamaker model over the results of the square-well model. However, this finding does not

completely invalidate all results of the square-well model. The results presented here and in Chapter 7 indicate areas in which both models predict similar results and areas in which their results diverge.

The noted effects of particle-particle cohesion in both models are significant. Previous one-dimensional force balance models of the fluidization process are capable of predicting the pressure overshoot without the inclusion of cohesion. However, the success of these models depends largely on numerous empirical fitting parameters. The results from this effort indicate that those one-dimensional force balance models should also include cohesive forces. In future efforts, it may be possible to include cohesion in the form of a limiting tensile stress as suggested by Jackson [2].

8.6 References

1. Tsinontides, S.C. and R. Jackson, *The mechanics of gas fluidized beds with an interval of stable fluidization.* J. Fluid Mech., 1993. **255**: p. 237.
2. Jackson, R., *The nature and role of effective stress in fluidized systems*, in *Fluidization IX*, T.M. Knowlton, Editor. 1998, Engineering Foundation Publication: New York. p. 1.
3. Srivastava, A. and S. Sundaresan, *Role of wall friction in fluidization and standpipe flow.* Powder Technology, 2002. **124**: p. 45.
4. Loezos, P.N., P. Costamagna, and S. Sundaresan, *The role of contact stresses and wall friction on fluidization.* Chemical Engineering Science, 2002. **57**: p. 5123.

Chapter 9 Summary

The effects of cohesion have been investigated in both granular and gas-solid flows via discrete-particle simulations. The capability of the square-well model to capture the effects of mild cohesion between particles has been assessed. The square-well model is a candidate for incorporating cohesion into continuum models since cohesion is treated as impulsive events that that do not violate the assumption of binary, instantaneous contacts inherent in kinetic-theory models. The key conclusions and implications of both studies are summarized below.

9.1 Summary of Results

9.1.1 Cohesive Granular Flows

Simple, two-particle simulations show that an analytical expression for an effective coefficient of restitution (that incorporates the effects of cohesion *and* inelastic collisions) is only accurate within the limit for which it was derived. More specifically, the analytical expression accurately describes the effects of the square-well model only as the width of the cohesive well approaches the particle radius. However, as the well width is increased, the coefficient of restitution obtained from the analytical expression diverges from that determined via simulation.

The implementation of the square-well model into many-particle systems undergoing simple shear flow indicates that two drastically different flow regimes exist. At relatively high levels of cohesion, large agglomerates form that incorporate most of the particles in the simulation domain. At moderate levels of cohesion, the particles form mostly two- and three-particle agglomerates. This abrupt change in the

flow regime is reminiscent of the marked change in gas-solid fluidization behavior observed between Geldart Type A and Type C particles [1]. Furthermore, for systems with moderate levels of cohesion, the addition of cohesion has little influence on the stress obtained in simulations at low solids fractions (kinetic regime). However, at higher solids fractions (collisional regime), the addition of cohesion results in a decrease in the magnitude of all components of the stress tensor.

The behaviors predicted by the square-well model are in qualitative agreement with those expected for cohesive granular systems. As the next step in the assessment of the square-well potential, the cohesion model was incorporated into a simulation of gas-solid flow and compared with the results of a more elaborate cohesion model.

9.1.2 Cohesive Gas-Solid Flows

Cohesive forces were incorporated into discrete-particle models for gas-solid fluidized beds using both the square-well model and the Hamaker model for van der Waals forces. This task was accomplished within the framework of the MFIX code developed at DOE NETL (www.mfix.org). Both the square-well and Hamaker models capture the transition from Geldart Type A to Geldart Type C fluidization behavior. In both models, plugging and channeling is observed at relatively high levels of cohesion. However, the nature of the plugs and channels is different within the two models. Within the square-well model, rigid plugs rise in the bed as a single mass, and within the Hamaker model, plugs are more likely to break apart into multi-particle agglomerates. Simulation results from both models consistently display an increase in the minimum fluidization velocities ($U_{mf,in}$, $U_{mf,th}$, and $U_{mf,df}$) as the level

of cohesion is increased. This trend is consistent with a general increase in minimum fluidization velocity that has been observed experimentally [2-4]. Although most experimental efforts do not provide the detail necessary for determining which of the three critical velocities defined here is being measured.

A mapping between the two cohesion models was developed using the two-particle escape velocity for particles undergoing head-on (normal) collisions. Simulations with parameters that produced equivalent two-particle escape velocities were implemented to test the mapping effectiveness. Simulation results were compared via simulation snapshots, animations, and measurements of the mixing index, fluidization velocity, and average particle movement. This analysis reveals that the escape velocity provides a suitable common ground between the two cohesion models. The importance of this mapping lies in the ability to convert Hamaker constants, which have been measured for many materials, into the square-well depth, for which there is no experimental data. The effects of the length scales in both cohesion models were also investigated and found to have a minimal impact on the influence of cohesion in many-particle simulations.

The square-well model and the Hamaker model were also used to study the phenomenon of pressure overshoot, which has been documented experimentally [5-7]. Pressure overshoot occurs during the fluidization cycle when pressure drop exceeds the weight of the particles in the bed divided by the cross-sectional area of the bed. During a simulation of the fluidization cycle (after a defluidization cycle), the net force imposed on the particles by several interactions was collected. Also, specific interactions (e.g., cohesive particle-particle, cohesive particle-sidewall, cohesive

particle-distributor plate) were systematically removed from the simulation in order to assess their impact on the overall system. Simulations using both models are able to predict the pressure overshoot. Furthermore, the simulations indicate that pressure overshoot can be traced predominantly to cohesive forces. This finding adds a new level of understanding to a fluidization phenomenon that previously been attributed vaguely to the combined effects of friction and cohesion. Cohesive interactions with the sidewalls and distributor plate also had a less significant effect on the pressure overshoot, depending on the model. In simulations using the square-well model, cohesive interactions between the particles and the distributor were more significant than interactions with the sidewalls, while in simulations using the Hamaker model cohesive interactions with the sidewalls had slightly more influence than cohesive interactions between particles and the distributor plate. Simulations employing the Hamaker model also predict an increase in the pressure overshoot as the bed width is decreased, while the square-well model simulations do not. Previous experimental results found that the pressure overshoot increases as the bed width is decreased [5-8]. These results reaffirm that the Hamaker model is a more complete description of cohesive forces in particulate flow.

While these results illustrate some drawbacks of the square-well model, it has still been shown to be a useful tool in many situations. As mentioned previously, the square-well model successfully predicts the correct trends in the minimum fluidization velocity and provides an adequate depiction of the transition from Geldart Type A behavior to Geldart Type C behavior. Furthermore, the impulsive nature of

the square-well model makes it applicable to kinetic theory, while the Hamaker model is not.

These results provide support for the square-well potential as an effective means of incorporating cohesion into continuum models, which are needed for application to industrial-size systems (since the number of particles in such systems is too large to handle via a discrete-particle simulation). Also, these results illustrate the potential of the Eulerian-Lagrangian method as a tool for obtaining insight into experimental systems. However, this method does have its limitations, one of which is discussed in the next section.

9.2 Limitations of Eulerian-Lagrangian Method

Despite the benefits offered by Eulerian-Lagrangian simulations in the study of fluidized systems, this method is not expected to be applicable to situations involving the fluidization of highly cohesive particles (Type C). In particular, agglomerate fluidization of Type C particles is a fluidized-bed phenomenon that pushes the limits of the Eulerian-Lagrangian method.

Typically, high levels of cohesion prevent Type C particles from fluidizing in a conventional manner. In some cases, however, low-density Type C particles combine to form agglomerates that are larger and less dense than the primary particles. These agglomerates are capable of fluidization at a gas velocity above the minimum fluidization velocity for the primary particles [9-14]. These agglomerates consist of several hundred particles, with substantially different fluidization characteristics compared to those of the primary particles.

The ability of the Eulerian-Lagrangian method to simulate these systems is hindered by the spatial resolution associated with solving the fluid-phase balances. The closely-packed nature of agglomerates causes differences in the fluid forces imposed on particles at the surface of the agglomerate relative to particles inside the agglomerate. In the Eulerian-Lagrangian approach, however, all particles in a given computational cell experience the *same* fluid velocity. The computational cell size must be large enough to include approximately 20 particles in order to calculate statistically representative local, solid-phase properties (i.e., average solid velocity, void fraction). With computational cells this large, a single cell is expected to contain a significant portion of an agglomerate. Because all particles within the cell are exposed to the same fluid velocity, particles on the surface of the agglomerate experience the same fluid drag force as those in the agglomerate interior. However, the drag on interior particles *should* be substantially less than the drag on particles at the surface of the agglomerate due to the reduced gas velocity in the agglomerate interior. Hence, the limiting spatial resolution of the fluid phase solution hinders the ability of the Eulerian-Lagrangian method to effectively predict the behavior of agglomerating fluidized beds.

9.3 Recommendations for Future Work

Building on the results presented here, additional phenomena could be studied via minor modifications to the existing cohesive Eulerian-Lagrangian simulation. A liquid-bridging model can be incorporated into the existing cohesion models to study the effects of liquid-bridges [15]. Vibrating sidewalls can also be added to study

mechanical flow initiation [16-20]. Gravitational forces can be enhanced to simulate centrifugal fluidized beds [21].

Another clear direction for future work is the improvement of continuum models for multi-phase flow. The primary motivation for using a discrete-particle model in this effort is the ease in which cohesion can be applied to discrete particles. However, as described in Chapter 1, the impulsive nature of the square-well model facilitates the incorporation of cohesion into continuum models. This work has shown that the square-well model provides an adequate description of cohesive interactions particulate systems. A logical next step would be to incorporate the square-well model to a continuum (kinetic-theory) model. Although a continuum model may be limited by the spatial resolution needed to study agglomerating systems, such a model would be useful in describing systems with mild cohesion (e.g., Type A particles).

A possible means of studying agglomerating systems would be the incorporation of these cohesion models in direct numerical simulations (DNS), which were alluded to in Chapter 5. These models currently would not be able to simulate full fluidized bed systems due to computational limitations, however the simulation of smaller systems (~10 particles) could provide relevant insight into nature of gas flow around and through mutli-particle agglomerates. A simulation such as this would not be constrained by the limitations of a computational grid size and could be used to test the effectiveness of existing models [11-13, 22] for agglomerate size.

9.4 References

1. D. Geldart, Types of Gas Fluidization, *Powder Technology* 7 (1973) 285-292.
2. P. C. Wright and J. A. Raper, Role of liquid bridge forces in cohesive fluidization, *Transactions of the Institution of Chemical Engineers* 76 (1998) 753-760.
3. P. C. Wright and J. A. Raper, Examination of dispersed liquid-phase three-phase fluidized beds: Part 1 Non-porous, uniform particle systems, *Powder Technology* 97 (1998) 208.
4. M. L. Passos and A. S. Mujumdar, Effect of cohesive forces on fluidized and spouted beds of wet particles, *Powder Technology* 110 (2000) 222.
5. S. C. Tsinontides and R. Jackson, The mechanics of gas fluidized beds with an interval of stable fluidization, *Journal of Fluid Mechanics* 255 (1993) 237.
6. P. N. Loezos, P. Costamagna, and S. Sundaresan, The role of contact stresses and wall friction on fluidization, *Chemical Engineering Science* 57 (2002) 5123.
7. A. Srivastava and S. Sundaresan, Role of wall friction in fluidization and standpipe flow, *Powder Technology* 124 (2002) 45.
8. R. Jackson, The nature and role of effective stress in fluidized systems, in Fluidization IX, L. -S. Fan and T M Knowlton, Editors, 1998, Engineering Foundation Publication: New York. 1.
9. J. Chaouki, F. Larachi, and M. P. Dudukovic, Noninvasive Tomographic and Velocimetric Monitoring of Multiphase Flows, *Industrial and Chemistry Research* 36 (11) (1997) 4476.
10. C. Lauga, J. Chaouki, D. Klvana, and C. Chavarie, Improvement of fluidisability of Ni/SiO2 aerogels by reducing interparticle forces, *Powder Technology* 65 (1991) 461.
11. Y. Iwadate and M. Horio, Prediction of agglomerate sizes in bubbling fluidized beds of group C powders, *Powder Technology* 100 (1998) 223.
12. S. Morooka, K. Kusakabe, A. Kobata, and Y. Kato, Fluidization state of ultrafine powders, *Journal of Chemical Engineering of Japan* 21 (1) (1988) 41.
13. T. Zhou and L. Hongzhong, Estimation of agglomerate size for cohesive particles during fluidization, *Powder Technology* 101 (1999) 57-62.
14. T. Zhou and L. Hongzhong, Effects of adding different size particles on fluidization of cohesive particles, *Powder Technology* 102 (1999) 215.
15. T. Mikami, H. Kamiya, and M. Horio, Numerical simulation of cohesive powder behavior in a fluidized bed, *Chemical Engineering Science* 53 (10) (1998) 1927.
16. J. M. Valverde, Castellanos, A., Quintanilla, M.A.S., Effect of vibration on the stability of a gas-fluidized bed of fine powder, *Physical Review E* 64 (2001) 021302.
17. Y. Tatemoto, Y. Mawatari, T. Yasukuwa, and K. Noda, Numerical simulation of particle motion in vibrated bed, *Chemical Engineering Science* 59 (2004) 437.
18. K. Noda, Y. Mawatari, and S. Uchida, Flow patterns of fine particles in a vibrated bed under atmospheric or reduced pressure, *Powder Technology* 99 (1998) 11.
19. Y. Mawatari, Kiode, T., Tatemoto, Y., Uchida, S., Noda, K., Effect of particle diameter on fluidization under vibration, *Powder Technology* 123 (2002) 69.
20. E. Marring, A. C. Hoffman, and L. P. B. M. Janssen, The Effect of Vibration on the Fluidization Behaviour of Some Cohesive Powders, *Powder Technology* 79 (1994) 1-10.
21. G.-H. Qian, I. Bagyi, I. W. Burdick, R. Pfeffer, H. Shaw, and J. G. Stevens, Gas-solid fluidization in a centrifugal field, *AIChE Journal* 47 (5) (2001) 1022.
22. J. Chaouki, C. Chavarie, D. Klvana, and G. Pajonk, Effect of interparticle forces on the hydrodynamic behavior of fluidized aerogels, *Powder Technology* 43 (1985) 117.

Bibliography

M. P. Allen and D. J. Tildesley, Computer Simulation of Liquids, Oxford University Press, Oxford,1987.

T. B. Anderson and R. Jackson, A fluid mechanical description of fluidized beds, *Industrial and Engineering Fundamentals* 6 (1967) 527.

E. Barthel and G. Haiat, Approximate model for the adhesive contact of viscoelastic spheres, *Langmuir* 18 (2002) 9362.

J. Baxter, H. Abou-Chakra, U. Tuzun, and B. Lamptey, A DEM simulation and experimental strategy for solving fine powder flow problems, *Chemical Engineering Research and Design* 78 (2000) 1019.

F. P. Bowden and D. Tabor, Friction and lubrication, Wiley, London, 1956.

D. S. Boyalakuntla, "Simulation of Granular and Gas-Solid Flows Using Discrete Element Method", PhD dissertation, Carnegie Mellon University, 2003.

J. Bridgwater, Mixing and segregation mechanisms in particle flow, in Granular Matter: An interdisciplinary approach, A Mehta, Editor, 1994, Springer-Verlag: New York. 160.

J. Bridgwater, Particle Technology, *Chemical Engineering Science* 50 (24) (1995) 4081.

C. Campbell, Rapid Granular Flows, *Annual Review of Fluid Mechanics* 22 (1990) 57.

C. S. Campbell, "Shear flows of granular materials", PhD dissertation, Calfornia Institute of Technology, 1982.

C. S. Campbell, The Stress Tensor for Simple Shear Flows of Granular Material, *Journal of Fluid Mechanics* 203 (1989) 449.

C. S. Campbell and C. E. Brennen, Computer simulation of granular shear-flows, *Journal of Fluid Mechanics* 151 (1985) 167.

J. W. Carson, Equipment, modeling and testing - Bulk solids handling, *Chemical Engineering* 109 (8) (2002) 98.

J. Chaouki, C. Chavarie, D. Klvana, and G. Pajonk, Effect of interparticle forces on the hydrodynamic behavior of fluidized aerogels, *Powder Technology* 43 (1985) 117.

J. Chaouki, F. Larachi, and M. P. Dudukovic, Noninvasive Tomographic and Velocimetric Monitoring of Multiphase Flows, *Industrial and Chemistry Research* 36 (11) (1997) 4476.

R. Chirone and L. Massimilla, Sound-assisted aeration of beds of cohesive solids, *Chemical Engineering Science* 49 (8) (1994) 1185.

R. Chirone, L. Massimilla, and S. Russo, Bubble-free fluidization of a cohesive powder in an acoustic field, *Chemical Engineering Science* 48 (1) (1993) 41.

P. W. Cleary and M. L. Sawley, DEM simulation of industrial granular flows: 3D case studies and the effect of particle shape on hopper discharge, *Applied Mathematical Modeling* 26 (2002) 89.

R. Clelland and C. M. Hrenya, Simulation of a binary-sized mixture of inelastic grains in rapid shear flow, *Physical Review E* 65 (2002)

P. A. Cundall, A computer model for rock-mass behavior using interactive graphics for input and output of geometrical data, *US Army Corps of Engineers (Missouri River Div) Tech. Rep. MRD-2074* (1974)

P. A. Cundall and O. D. Strack, A discrete numerical model for granular assemblies, *Geotechnique* 29 (1) (1979) 47-65.

J. M. Dalla Valle, Micromeritics, Pitman, London, 1948.

B. J. Ennis, J. Green, and R. Davies, The legacy of neglect in the U.S., *Chemical Engineering Progress* April (1994) 32.

H. Enwald, E. Peirano, and A.-E. Almstedt, Eulerian two-phase flow theory applied to fluidization, *International Journal of Multiphase Flow* 22 (Suppl.) (1996) 21.

L.-S. Fan, Gas-liquid-solid fluidization engineering, Butterworths, Boston, 1989.

R. J. Farruato and C. H. Bartholomew, Fundamentals of industrial catalytic processes, Blackie Academic and Professional, London, 1997.

S. F. Foerster, M. Y. Louge, H. Chang, and K. Allia, Measurements of the collision properties of small spheres, *Phys. Fluids* 6 (3) (1994) 1108.

A. J. Forsyth, S. Hutton, and M. J. Rhodes, Effect of cohesive interparticle force on the flow characteristics of granular material, *Powder Technology* 126 (2002) 150.

J. Garside and M. R. Al-Dibouni, Velocity-voidage relationships for fluidization and sedimentation in solid-liquid systems, *Ind. Eng. Chem., Process Des. Dev.* 16 (2) (1977) 206.

C. J. Geankopolis, Transport processes and unit operations, Allyn and Bacon, Boston, 1983.

D. Geldart, Types of Gas Fluidization, *Powder Technology* 7 (1973) 285-292.

D. Gera, M. Gautam, Y. Tsuji, T. Kawaguchi, and Y. Tanaka, Computer simulation of bubbles in large-particle fluidized beds, *Powder Technology* 98 (1998) 38.

D. Gidaspow and L. Huilin, Equation of state and radial distribution functions of FCC particles in a CFB, *AIChE Journal* 44 (2) (1998) 279.

I. Goldhirsch, Rapid granular flows, *Annual Review of Fluid Mechanics* 35 (2003) 267.

W. Goldsmith, Impact: the theory of physical behavior of colliding solids, E. Arnold, London, 1960.

J. R. Grace and F. Taghipour, Verification and validation of CFD models and dynamic similarity for fluidized beds, *Powder Technology* 139 (2004) 99.

A. K. Gupta, D. G. Lilley, and N. Syred, Swirl Flows, Abacus Press, Tunbridge Wells, 1984.

H. C. Hamaker, The London-Van der Waals attraction between spherical particles, *Physica* 4 (10) (1937) 1058-1072.

E. Helland, R. Occelli, and L. Tadrist, Numerical study of cluster formation in a gas-particle circulating fluidized bed, *Powder Technology* 110 (2000) 210.

C. A. Herrera and E. K. Levy, Bubbling characteristics of sound-assisted fluidized beds, *Powder Technology* 119 (2001) 229.

C. A. Herrera, E. K. Levy, and J. Ochs, Characteristics of acoustic standing waves in fluidized beds, *AIChE Journal* 48 (2) (2002) 503.

B. P. B. Hoomans, J. A. M. Kuipers, W. J. Briels, and W. P. M. V. Swaaij, Discrete particle simulation of bubble and slug formation in a two-dimensional gas-fluidised bed: a hard-sphere approach, *Chemical Engineering Science* 51 (1) (1996) 99.

B. P. B. Hoomans, J. A. M. Kuipers, M. A. M. Salleh, M. Stein, and J. P. K. Seville, Experimental validation of granular dynamics simulations of gas-fluidised

beds with homogenous in-flow conditions using positron emission particle tracking, *Powder Technology* 116 (2001) 166.

B. P. B. Hoomans, J. A. M. Kuipers, and W. P. M. v. Swaaij, Granular dynamics simulation of segregation phenomena in bubbling gas-fluidized beds, *Powder Technology* 109 (2000) 41.

M. A. Hopkins and M. Y. Louge, Inelastic microstructure in rapid granular flows of smooth disks, *Phys. Fluids A* 3 (1) (1991) 47-57.

J. Israelachvili, Intermolecular and Surface Forces, Academic Press London, London, 1991.

Y. Iwadate and M. Horio, Prediction of agglomerate sizes in bubbling fluidized beds of group C powders, *Powder Technology* 100 (1998) 223.

R. Jackson, The nature and role of effective stress in fluidized systems, in Fluidization IX, L. -S. Fan and T M Knowlton, Editors, 1998, Engineering Foundation Publication: New York. 1.

K. L. Johnson, K. Kendall, and A. D. Roberts, Surface Energy and the contact of elastic solids, *Proceedings of the Royal Society of London A* 324 (1971) 301.

T. Kawaguchi, T. Tanaka, and Y. Tsuji, Numerical simulation of two-dimensional fluidized beds using the discrete element method (comparison between two- and three-dimensional models), *Powder Technology* 96 (1998) 129.

F. J. Keller, W. E. Gettys, and M. J. Skove, Physics, McGraw-Hill, 1993.

H. Kim and H. Arastoopour, Extension of kinetic theory to cohesive particle flow, *Powder Technology* 122 (2002) 83-94.

H. King, R. White, I. Maxwell, and N. Menon, Inelastic impact of a sphere on a massive plane: nonmonotonic velocity-dependence of the restitution coefficient, (not published)

T. M. Knowlton, J. W. Carson, G. E. Klinzing, and W.-C. Yang, The importance of storage, transfer and collection, *Chemical Engineering Progress* 90 (April) (1994) 44.

T. Kobayashi, T. Mukai, T. Kawaguchi, T. Tanaka, and Y. Tsuji, DEM analysis of flow patterns of Geldart's group A particles in fluidized bed, *World Congress on Particle Technology 4, Sydney, Australia* (2003)

H. Krupp, *Advances in Colloid Interface Science* 1 (2) (1967)

D. Kunii and O. Levenspiel, Fluidization Engineering, Butterworth-Heinemann, Boston, 1991.

K. Kuwagi, T. Mikami, and M. Horio, Numerical simulation of metallic solid bridging particles in a fluidized bed at high temperature, *Powder Technology* 109 (2000) 27.

L. Labous, A. D. Dosato, and R. N. Dave, Measurements of collisional properties of spheres using high-speed video analysis, *Physical Review E* 56 (5) (1997) 5717.

P. A. Langston, U. Tuzun, and D. M. Heyes, Discrete element simulation of granular flow in 2D and 3D hoppers: dependence of discharge rate and wall stress on particle interactions, *Chemical Engineering Science* 50 (6) (1995) 967.

C. Lauga, J. Chaouki, D. Klvana, and C. Chavarie, Improvement of fluidisability of Ni/SiO2 aerogels by reducing interparticle forces, *Powder Technology* 65 (1991) 461.

A. W. Lees and S. F. Edwards, The computer study of transport processes under extreme conditions, *Journal of Physics C: Solid State Physics* 5 (1972) 1921.

E. K. Levy, I. Shnitzer, T. Masaki, and J. Salmento, Effect of an acoustic field on bubbling in a gas fluidized bed, *Powder Technology* 90 (1997) 53.

H. Li, McCarthy, J. J., Controlling Cohesive Particle Mixing and Segregation, *Physical Review Letters* 90 (18) (2003) 184301.

J. Li, Kuipers, J.A.M., Effect of pressure on gas-solid flow behavior in dense gas-fluidized beds: a discrete particle simlation study, *Powder Technology* 127 (2002) 173.

G. Lian, C. Thornton, and M. J. Adams, A theoretical study of the liquid bridge forces between two rigid spherical bodies, *Journal of Colloid and Interface Science* 161 (1993) 131.

E. M. Lifshitz, The theory of molecular attractive forces between solids, *Journal of Experimental and Theoretical Physics* 2 (1) (1956) 73.

S. Limtrakul, A. Chalermwattanatai, K. Unggerawirote, Y. Tsuji, T. Kawaguchi, and W. Tanthapanichakoon, Discrete particle simulations of solids motion in a gas-solid fluidized bed, *Chemical Engineering Science* 58 (2003) 915.

P. N. Loezos, P. Costamagna, and S. Sundaresan, The role of contact stresses and wall friction on fluidization, *Chemical Engineering Science* 57 (2002) 5123.

F. London, *Z. Phys.* 63 (1930) 245.

C. K. K. Lun, S. B. Savage, D. J. Jeffrey, and N. Chepurnity, Kinetic theories for granular flow: Inelastic particles in Couette flow and slightly inelastic particles in a general flow field, *Journal of Fluid Mechanics* 140 (223) (1984)

A. Margolin, R. Rosentsveig, A. Albu-Yaron, R. Popovitz-Biro, and R. Tenne, Study of growth mechanism of WS2 nanotubes produced by a fluidized bed reactor, *Journal of Materials Chemistry* 14 (4) (2004) 617.

E. Marring, A. C. Hoffman, and L. P. B. M. Janssen, The Effect of Vibration on the Fluidization Behaviour of Some Cohesive Powders, *Powder Technology* 79 (1994) 1-10.

S. Matsuda, H. Hatano, and A. Tsutsumi, Ultrafine particle fluidization and its application to photocatalytic NOx treatment, *Chemical engineering Journal* 82 (2001) 183.

H. G. Matuttis and A. Schinner, Particle simulation of cohesive granular material, *International Journal of Modern Physics* 12 (7) (2001) 1011.

Y. Mawatari, T. Kiode, Y. Tatemoto, S. Uchida, and K. Noda, Effect of particle diameter on fluidization under vibration, *Powder Technology* 123 (2002) 69.

D. N. Mazzone, G. I. Tardos, and R. Pfeffer, The effect of gravity on the shape and strength of a liquid bridge between two spheres, *Journal of Colloid and Interface Science* 113 (2) (1986) 544.

J. J. McCarthy, Micro-modeling of cohesive mixing processes, *Powder Technology* 138 (2003) 63.

J. J. McCarthy, D. V. Khakhar, and J. M. Ottino, Computational studies of granular mixing, *Powder Technology* 109 (2000) 72.

J. J. McCarthy and J. M. Ottino, A computational study of granular mixing: the effect of particle cohesion, *AIChE meeting proceedings* (1988)

J. J. McCarthy and J. M. Ottino, Particle dynamics: a hybrid technique applied to granular mixing, *Powder Technology* 97 (1998) 91.

T. McKeen and T. Pugsley, Simulation and experimental validation of a freely bubbling bed of FCC catalyst, *Powder Technology* 129 (2003) 139.

L. J. McLaughlin and M. J. Rhodes, Prediction of fluidized bed behaviour in the presence of liquid bridges, *Powder Technology* 114 (2001) 213.

V. P. Mehrotra and V. S. Sastry, Pendular bond strength between unequal-sized spherical particles, *Powder Technology* 25 (1980) 203.

R. Mei, H. Shang, O. Walton, and J. Klausner, Concentration non-uniformity in simple shear flow of cohesive powders, *Powder Technology* 112 (2000) 102.

T. Mikami, H. Kamiya, and M. Horio, Numerical simulation of cohesive powder behavior in a fluidized bed, *Chemical Engineering Science* 53 (10) (1998) 1927.

O. Molerus, Interpretation of Geldart's type A, B, C and D powders by taking into account interparticle cohesion forces, *Powder Technology* 33 (1982) 81.

S. Morooka, K. Kusakabe, A. Kobata, and Y. Kato, Fluidization state of ultrafine powders, *Journal of Chemical Engineering of Japan* 21 (1) (1988) 41.

P. Mort,Tutorial on processing, handling and characterization of powder agglomerates,Indianapolis,2002.

Y. Muguruma, T. Tanaka, and Y. Tsuji, Numerical simulation of particulate flow with liquid bridge between particles (simulation of centrifugal tumbling granulator), *Powder Technology* 109 (2000) 49.

S. M. P. Mutsers and K. Rietema, The effect of interparticle forces on the expansion of a homogeneous gas-fluidized bed, *Powder Technology* 18 (1977) 239.

F. J. Muzzio, T. Shinbrot, and B. J. Glasser, Powder technology in the pharmaceutical industry: the need to catch up fast, *Powder Technology* 124 (1-2) (2002) 1.

S. T. Nase, W. L. Vargas, A. A. Abatan, and J. J. McCarhy, Discrete characterization tools for cohesive granular material, *Powder Technology* 116 (2001) 214-223.

K. Noda, Y. Mawatari, and S. Uchida, Flow patterns of fine particles in a vibrated bed under atmospheric or reduced pressure, *Powder Technology* 99 (1998) 11.

J. M. Ottino and D. V. Khakhar, Mixing and segregation of granular materials, *Annual Review of Fluid Mechanics* 32 (2000) 55.

J. Ouyang and J. Li, Particle-motion-resolved discrete model for simulating gas-solid fluidization, *Chemical Engineering Science* 54 (1999) 2077.

M. L. Passos and A. S. Mujumdar, Effect of cohesive forces on fluidized and spouted beds of wet particles, *Powder Technology* 110 (2000) 222.

J. M. Prausnitz, R. N. Lichtenthaler, and E. G. d. Azevedo, Molecular Thermodynamics of Fluid-Phase Equilibria, 3rd ed., Prentic Hall, Upper Saddle River, New Jersey, 1999.

G.-H. Qian, I. Bagyi, I. W. Burdick, R. Pfeffer, H. Shaw, and J. G. Stevens, Gas-solid fluidization in a centrifugal field, *AIChE Journal* 47 (5) (2001) 1022.

M. L. Rader, Worldwide refining, *Oil and Gas Journal* (December 23) (1996) 52.

A. D. Renzo and F. P. D. Maio, Comparison of contact-force models for simulation of collisions in DEM-based granular flow codes, *Chemical Engineering Science* 59 (2004) 525.

M. Rhodes, Introduction to Particle Technology, John Wiley and Sons Ltd., West Sussex, England, 1998.

M. Rhodes, Fluidization of particles by fluids, http://www.erpt.org/012Q/rhod-04.htm (2001).

M. J. Rhodes and X. S. Wang, The role of interparticle force in determining Geldart group behavior: a DEM study, *2000 AIChE Annual Meeting* (2000).

M. J. Rhodes, X. S. Wang, M. Nguyen, P. Stewart, and K Liffman, Onset of cohesive behavior in gas fluidized beds: a numerical study using DEM simulation, *Chemical Engineering Science* 56 (2001) 4433-4438.

M. J. Rhodes, X. S. Wang, M. Nguyen, P. Stewart, and K. Liffman, Study of mixing in gas-fluidized bed using a DEM model, *Chemical Engineering Science* 56 (2001) 2859.

M. J. Rhodes, X. S. Wang, M. Nguyen, P. Stewart, and K. Liffman, Use of discrete element method simulation in studying fluidization characteristics: influence of interparticle force, *Chemical Engineering Science* 56 (2001) 69-76.

A. W. Roberts, Particle technology -- Reflections and horizons: An engineering perspective, *Transactions of the Institution of Chemical Engineers* 76 (October) (1998) 775.

P. Russo, R. Chirone, L. Massimilla, and S. Russo, The influence of the frequency of acoustic waves on sound-assisted fluidization of beds of fine particles, *Powder Technology* 82 (1995) 219-230.

R. Sadeghbeigi, Fluid catalytic cracking handbook, Gulf Publishing, Houston, Texas, 2000.

J. P. K. Seville, Processing of Particulate Solids, Blackie Academic and Professional, London, 1997.

J. P. K. Seville and R. Clift, The effect of thin liquid layers on fluidization characteristics, *Powder Technology* 37 (1984) 117.

J. P. K. Seville, C. D. Willet, and P. C. Knight, Interparticle forces in fluidisation: a review, *Powder Technology* 113 (2000) 261-268.

T. Shinbrot, D. Khakhar, J. J. McCarthy, and J. Ottino, A simple model for granular convection, *Physical Review Letters* 79 (5) (1997) 829.

J. L. Sinclair, Hydrodynamic modeling, in Circulating Fluidized Beds, J R Grace, A A Auidan, and T M Knowlton, Editors, 1997, Chapman and Hall: Great Britain.

J. L. Sinclair and R. Jackson, Gas-particle flow in a vertical pipe with particle-particle interactions, *AIChE Journal* 35 (9) (1989) 1473.

A. Srivastava and S. Sundaresan, Role of wall friction in fluidization and standpipe flow, *Powder Technology* 124 (2002) 45.

Y. Tatemoto, Y. Mawatari, T. Yasukuwa, and K. Noda, Numerical simulation of particle motion in vibrated bed, *Chemical Engineering Science* 59 (2004) 437.

P. Tegzes, R. Albert, M. Paskan, A.-L. Barabasi, T. Vicsek, and P. Schiffer, Liquid-induced transitions in granular media, *Physical Review E* 50 (5) (1999) 5823-5826.

P. Tegzes, T. Vicsek, and P. Schiffer, Avalanche dynamics in wet granular materials, *Physical Review Letters* 89 (9) (2002) 094301.

P. Tegzes, T. Vicsek, and P. Schiffer, Development of correlations in the dynamics of wet granular avalanches, *Physical Review E* 67 (5) (2003) 051303.

S. C. Tsinontides and R. Jackson, The mechanics of gas fluidized beds with an interval of stable fluidization, *Journal of Fluid Mechanics* 255 (1993) 237.

Y. Tsuji, T. Kawaguchi, and T. Tanaka, Discrete particle simulation of two-dimensional fluidized bed, *Powder Technology* 77 (1993) 79.

J. M. Valverde, A. Castellanos, and M. A. S. Quintanilla, Effect of vibration on the stability of a gas-fluidized bed of fine powder, *Physical Review E* 64 (2001) 021302.

J. Visser, On Hamaker constants: A comparison between Hamaker constants and Lifshitz-van der Waals constants, *Advances in Colloid Interface Science* 3 (1972) 331.

J. Visser, An invited review: van der waals and other cohesive forces affecting powder fluidization, *Powder Technology* 58 (1989) 1-10.

B. G. M. v. Wachem and A. E. Almstedt, Methods for multiphase computational fluid dynamics, *Chemical engineering Journal* 96 (2003) 81.

B. G. M. v. Wachem, J. v. d. Schaaf, J. C. Schouten, R. Krishna, and C. M. v. d. Bleek, Experimental validation of Lagrangian-Eulerian simulations of fluidized beds, *Powder Technology* 116 (2001) 155-165.

O. R. Walton, Particle-dynamics calculations of shear flow, in Mechanics of Granular Materials: New Models and Constitutive Relations, J T Jenkins and M Satake, Editors, 1983, Elsevier Science Publications B.V.: Amsterdam.

O. R. Walton, Application of molecular dynamics to macroscopic particles, *International Journal of Engineering Science* 22 (8-10) (1984) 1097-1107.

O. R. Walton and R. L. Braun, Viscosity, granular-temperature, and stress calculations for shearing assemblies of inelastic, frictional disks, *Journal of Rheology* 30 (5) (1986) 949-980.

X. S. Wang and M. J. Rhodes, Mechanistic study of defluidization by numerical simulation, *Chemical Engineering Science* 59 (2004) 215.

J. R. Wank, S. M. George, and A. W. Weimer, Vibro-fluidization of fine boron nitride powder at low pressure, *Powder Technology* 121 (2001) 195.

P. C. Wright and J. A. Raper, Examination of dispersed liquid-phase three-phase fluidized beds: Part 1 Non-porous, uniform particle systems, *Powder Technology* 97 (1998) 208.

P. C. Wright and J. A. Raper, Role of liquid bridge forces in cohesive fluidization, *Transactions of the Institution of Chemical Engineers* 76 (1998) 753.

C.-Y. Wu, L. Dihoru, and A. C. F. Cocks, The flow of powder into simple and stepped dies, *Powder Technology* 134 (24) (2003) 24.

S. Y. Wu and J. Baeyens, Segregation by size difference in gas fluidized beds, *Powder Technology* 98 (1998) 139.

B. H. Xu and A. B. Yu, Numerical simulation of the gas-solid flow in a fluidized bed by combining discrete particle method with computational fluid dynamics, *Chemical Engineering Science* 52 (16) (1997) 2785-2809.

B. H. Xu, A. B. Yu, S. J. Chew, and P. Zulli, Numerical simulation of gas-solid flow in a bed with lateral gas blasting, *Powder Technology* 109 (2000) 13.

B. H. Xu, Y. C. Zhou, A. B. Yu, and P. Zulli, Force structures in gas fluidized beds of fine powders, *World Congress on Particle Technology 4, Sydney, Australia* (2002)

S. C. Yang and S. S. Hsiau, The simulation of powders with liquid bridges in a 2D vibrated bed, *Chemical Engineering Science* 56 (2001) 6837.

M. Ye, M. A. v. d. Hoef, and J. A. M. Kuipers, A numerical study of fluidization behavior of Geldart A particles using a discrete particle model, *Powder Technology* 139 (2004) 129.

K. Z. Y. Yen and T. K. Chaki, A dynamic simulation of particle rearrangement in powder packings with realistic interactions, *Journal of Applied Physics* 71 (7) (1992) 3164-3173.

S. Yuu, T. Umekage, and Y. Johno, Numerical simulation of air and particle motions in bubbling fluidized bed of small particles, *Powder Technology* 110 (2000) 158.

H. Zhou, G. Flamant, D. Gauthier, and Y. Flitiris, Simulation of coal combustion in a bubbling fluidized bed by distinct element method, *Chemical Engineering Research and Design* 81 (A9) (2003) 1144.

T. Zhou and L. Hongzhong, Effects of adding different size particles on fluidization of cohesive particles, *Powder Technology* 102 (1999) 215.

T. Zhou and L. Hongzhong, Estimation of agglomerate size for cohesive particles during fluidization, *Powder Technology* 101 (1999) 57-62.

Nomenclature

$\vec{a}_i$	Acceleration of ith particle (m s^{-2})
$a_{x,i}$	x-component of acceleration of ith particle (m s^{-2})
$a_{y,i}$	y-component of acceleration of ith particle (m s^{-2})
A	Hamaker constant (N m)
A_b	Cross-sectional area of fluidized bed (m^2)
A_{jet}	Cross-sectional area of inlet jet (m^2)
A_{LE}	Area of Lees-Edwards periodic domain in granular flow model (m^2)
B_o	Constant
C_o	Constant
d_p	Particle diameter (m)
D	Depth of cohesive square well (J)
D^*	Dimensionless well depth
D_{bed}	Fluidized bed width as used in model by Jackson (m)
e	Coefficient of restitution
$e_{eff,r_{outer}=r_{inner}}$	Effective coefficient of restitution derived for ideal case of $r_{outer}=r_{inner}$
E	Elastic (Young's) Modulus (N m^{-2})
f	Sound frequency (s^{-1})
F_c	Magnitude of cohesive force between two particles during soft-sphere interactions (N)
$\vec{F}_{coh,i}$	Sum of all cohesive forces on i^{th} particle (N)

$\vec{F}_{coll,i}$ Sum of all collisional forces on i^{th} particle (N)

$\vec{F}_{coll,ij}$ Collisional force between i^{th} and j^{th} particle (N)

$\vec{F}_{d,i}$ Drag force on force on i^{th} particle (N)

$\vec{F}_{f,i}$ Sum of all fluid forces on i^{th} particle (N)

$\vec{F}_{g,i}$ Gravitational force on i^{th} particle (N)

F_{gs} Drag coefficient (kg m^{-3} s^{-1})

$\vec{F}_{i}$ Sum of all forces on i^{th} particle (N)

$\vec{F}_{n,Hz}$ Repulsive force from Hertzian model (N)

$F_{n,ij}$ normal collision force between i^{th} and j^{th} particles (N)

$\vec{F}_{p,i}$ Pressure force on i^{th} particle (N)

$F_{t,ij}$ tangential collision force between i^{th} and j^{th} particles (N)

F_{vdW} van der Waals cohesive interparticle force (N)

$F_{vdW,wall}$ van der Waals cohesive particle-wall force (N)

$F_{x,i}$ x-component of net force on i^{th} particle (N)

$F_{y,i}$ y-component of net force on i^{th} particle (N)

h Height of fluidized bed (m)

$\langle h_1 \rangle$ Average height of particles in top half of bed for calculation of mixing index (m)

$\langle h_2 \rangle$ Average height of particles in bottom half of bed for calculation of mixing index (m)

H Surface-to-surface separation distance for Hamaker model (m)

H_{cut} Cutoff distance for Hamaker van der Waals model (m)

H_1 Initial separation distance for potential energy calculation (m)

H_2 Final separation distance for potential energy calculation (m)

$\vec{i}$ Unit vector pointing in x-direction

$\vec{I}_{gs}$ Momentum transfer between gas and solid phase (kg m^{-2} s^{-2})

$\vec{j}$ Unit vector pointing in y-direction

J_* Momentum impulse transferred during inelastic collision or cohesive interaction (kg m s^{-1})

J_{in} Momentum impulse transferred during inelastic collision (kg m s^{-1})

$J_{coh,app}$ Momentum impulse transferred during approaching-cohesive interaction (kg m s^{-1})

$J_{coh,esc}$ Momentum impulse transferred during escaping-cohesive interaction (kg m s^{-1})

$J_{coh,cap}$ Momentum impulse transferred during capture-cohesive interaction (kg m s^{-1})

$\vec{k}_{ij}$ normal unit vector (granular flow equations)

$\vec{k}_{ij,1}$ normal unit vector at point of instance of approaching cohesive interaction

$\vec{k}_{ij,2}$ normal unit vector at instance of physical contact

$\vec{k}_{ij,3}$ normal unit vector at instance of departing cohesive interaction

$\vec{k}_{n,ij}$ normal unit vector between centers of ith and j^{th} particles

$\vec{k}_{t,ij}$	Tanget unit vector between surfaces of colliding i^{th} and j^{th} particles
K_n	normal spring constant for particle-particle contacts (stiffness) (N m^{-1})
K_{n-wall}	normal spring constant for particle-wall contacts (stiffness) (N m^{-1})
$k_{n,hz}$	Hertzian force constant (N*$m^{-3/2}$)
K_t	tangential spring constant for particle-particle contacts (N m^{-1})
K_{t-wall}	tangential spring constant for particle-wall contacts (N m^{-1})
L	width of periodic domain in granular flow simulation (m)
Δl_{avg}	average particle movement (m)
Δl_i	distance moved by i^{th} particle over a specified time interval (m)
m	particle mass (kg)
m_{max}	Number of computational cells in the x-direction
n	total particles in fluidized bed simulation
$n_{agg,k}$	Number of agglomerates at k^{th} snapshot
$n_{col,i}$	Number of particles in contact with the ith particle at a given time step
n_{esc}	Number of escaping cohesive interactions
n_{ij}	Number of particles in cell i, j
n_{jets}	Number of inlet jets
n_{max}	Number of computational cells in the y-direction
$n_{s,agg}$	Number of snapshots used in calculating averaged agglomerate properties
n_1	Total particles in family 1 for calculating mixing index

n_2	Total particles in family 2 for calculating mixing index
N	Total particles in granular flow simulation
p	Pressure generated by sound wave (Pa)
p_{ref}	Reference pressure for calculation of SPL (20 μPa)
$\overline{P}$	Average number of particles per agglomerate
ΔP	Pressure drop across fluidized bed (Pa)
ΔP^*	Pressure drop divided by theoretical weight per unit area
$\vec{\nabla} P$	Gradient in fluidized bed pressure (Pa/m)
$P_{i,k}$	Number of particles in the ith agglomerate at k^{th} snapshot
ΔP_{over}	Pressure overshoot (Pa)
r_{inner}	Physical particle radius (m)
Δr_i	movement of ith particle over a given time span (m)
r_{outer}	width of square well (m)
R	Center-to-center separation distance between two particles (m)
s	Strain (m^2)
s_{lat}	Laterial strain
s_{long}	Longitudinal strain
$\overline{\overline{S}}_g$	Gas-phase stress tensor ($N\ m^{-2}$)
$\overline{\overline{S}}_s$	Solid-phase stress tensor ($N\ m^{-2}$)
t_c	Collision duration for soft-sphere interaction (s)
Δt	Time interval used to calculate collisional stress (s)

t_{agg} Time at which a given particle is captured by its first agglomerate partner (s)

Δt_{agg} Agglomerate duration (s)

$\Delta \bar{t}_{agg}$ Averaged agglomerate duration (s)

$\Delta t_{agg,i}$ Agglomerate duration of ith escaped particle (s)

Δt_{cr} critical time step based on given spring constant (s)

Δt_{dc} Data collection interval for stress calculation in granular flow simulation (s)

t_{esc} Time at which a given particle escapes from its last agglomerate partner (s)

Δt_f Time step for gas phase (s)

Δt_k Collision time at k^{th} snapshot (used in averaging agglomerate properties) (s)

t_m Time at maximum particle overlap in soft-sphere interaction (s)

Δt_s Time step for particle phase (s)

T Granular Temperature (m s^{-1})^2

T^* Dimensionless Granular Temperature

U_s Superficial gas velocity in fluidized bed (m/s)

U_s^* Normalized superficial gas velocity ($U_s / (U_{mf,th,non-cohesive})$)

$U_{mf,df}$ Defluidization velocity (m/s)

$U^*_{mf,dr}$ Defluidization velocity normalized by defluidization velocity for non-cohesive case

$U_{mf,in}$ Incipient fluidization velocity (m/s)

$U^*_{mf,in}$ Incipient fluidization velocity normalized by incipient fluidization velocity for non-cohesive case

$U_{mf,th}$ Theoretical minimum fluidization velocity (m/s)

$U^*_{mf,in}$ Theoretical minimum fluidization velocity normalized by theoretical minimum fluidization velocity for non-cohesive case

$\forall$ Volume of particle (m^3)

$\forall_i$ Volume of the ith particle (m^3)

$\vec{v}_{g,mn}$ Gas velocity in computational cell m, n ($m\ s^{-1}$)

$\vec{v}_i$ Velocity of ith particle ($m\ s^{-1}$)

$\vec{v}_{ij}$ relative velocity between i^{th} and j^{th} particle ($m\ s^{-1}$)

$\vec{v}_{ij,a}$ relative velocity before approaching cohesive interaction ($m\ s^{-1}$)

$\vec{v}_{ij,b}$ relative velocity before inelastic collision ($m\ s^{-1}$)

$\vec{v}_{ij,c}$ relative velocity after inelastic collision ($m\ s^{-1}$)

$\vec{v}_{ij,d}$ relative velocity after departing cohesive interaction ($m\ s^{-1}$)

$v_{ij,esc}$ Minimum normal, relative velocity needed to escape cohesive forces ($m\ s^{-1}$)

$\vec{v}_{i,post}$ Velocity of ith particle after hard-sphere collision ($m\ s^{-1}$)

$\vec{v}_{i,pre}$ Velocity of ith particle before hard-sphere collision (m s^{-1})

$\vec{v}_{n,ij}$ Normal component of relative velocity between i^{th} and j^{th} particle(m s^{-1})

v_o Initial relative velocity between two contacting particles (m/s)

$\vec{v}_s$ Locally-averaged solids velocity (m s^{-1})

$\vec{v}_{s,mn}$ Average solid velocity in cell m, n (m s^{-1})

$\vec{v}_{t,ij}$ tangential relative velocity (slip velocity) (m s^{-1})

$v_{x,i}$ Velocity of ith particle in the *x*-direction (m s^{-1})

$v'_{x,i}$ Random component of velocity of ith particle in the *x*-direction (m s^{-1})

$\bar{v}_{x,i}$ Bulk-flow component of velocity of ith particle in the *x*-direction (m s^{-1})

$v_{y,i}$ Velocity of ith particle in the *y*-direction (m s^{-1})

$v'_{y,i}$ Random component of velocity of ith particle in the *y*-direction (m s^{-1})

$\bar{v}_{y,i}$ Bulk-flow component of velocity of ith particle in the *y*-direction (m s^{-1})

$v_{y,i}$ y-component of velocity of ith particle (m s^{-1})

Δv_x Relative velocity between two particles in *x*-direction (m)

Δv_y Relative velocity between two particle in *y*-direction (m)

V_{mn} Volume of grid cell *m*, *n* (m^3)

V_{jet} Specified y-component of gas velocity at inlet jet (cm/s)

V_t Terminal Velocity (m s^{-1})

W Weight of particles in fluidized bed (N)

W_{th} Theoretical Weight of particle bed (excluding particles below lowest pressure node) (N)

x_i x location of ith particle (m)

Δx Displacement of particle centers in x-direction (m)

Δx_i movement of the ith particle in a given time step in the x-direction (m)

x_{max} Width of fluidized bed (m)

y_i y location of ith particle (m)

Δy Displacement of particle centers in y-direction (m)

Δy_i movement of the ith particle in a given time step in the y-direction (m)

y_{max} Height of fluidized bed (m)

δ Particle offset in two-particle simulations (m)

$\delta_{n,ij}$ Normal overlap between the ith and j^{th} particles (m)

$\delta_{n,max}$ Maximum normal overlap during soft-sphere collision (m)

$\delta_{t,ij}$ tangential overlap (m)

ε_g Locally-averaged void fraction

ε_s Locally-averaged solids volume fraction

$\varepsilon_{s,mn}$ Solids volume fraction in cell m, n

$\varepsilon_{g,2D}$ 2-dimensional void fraction based on discs in a plane

$\varepsilon_{g,3D}$ 3-dimensional void fraction obtained from correction equation

ϕ Solids area fraction in granular flow simulation

Φ Potential energy from cohesion forces (J)

Φ_{vdW} Potential energy due to attractive van der Waals forces (J)

γ Shear rate in granular flow simulation (s^{-1})

η_n normal damping coefficient for particle-particle contacts(N s m^{-1})

η_{n-wall} normal damping coefficient for particle-wall contacts(N s m^{-1})

η_t tangential damping coefficient for particle-particle contacts (N s m^{-1})

η_{t-wall} tangential damping coefficient for particle-wall contacts (N s m^{-1})

μ friction coefficient for particle-particle contacts

μ_g gas viscosity (kg s^{-1} m^{-1})

μ_{wall} friction coefficient for particle-wall contacts

ρ_g gas density (kg m^{-3})

ρ_s particle density (kg m^{-3})

σ Stress (within a solid body) (N m^{-2})

τ_{ij} *ij*-component of total stress (collisional + kinetic) (m s^{-2})

τ^*_{ij} *ij*-component of total stress (m s^{-2})

$\tau_{ij(col)}$ *ij*-component of collisional stress (m s^{-2})

$\tau_{ij(kin)}$ *ij*-component of kinetic stress (m s^{-2})

$\tau^*_{ij,app}$ portion of *ij*-component of collisional stress coming from approaching-cohesive interactions (dimensionless)

$\tau^*_{ij,esc}$ portion of *ij*-component of collisional stress coming from escaping-cohesive interactions (dimensionless)

$\tau^*_{ij,cap}$ portion of *ij*-component of collisional stress coming from capture-cohesive interactions (dimensionless)

$\tau^*_{ij,inl}$ portion of *ij*-component of collisional stress coming from inelastic collisions (dimensionless)

υ Poisson's ratio

ω_i rotation rate of ith particle (radians s^{-1})

Appendix A. Derivation of Effective Coefficient of Restitution

When considering a binary, instantaneous collision between two inelastic, smooth discs, with positions $(x_i, y_i), (x_j, y_j)$ and velocities (v_{xi}, v_{yi}), (v_{xj}, v_{yj}), the following quantities define the relative positions and velocities of the two particles:

$$\Delta x = x_j - x_i \qquad \text{(A1)}$$

$$\Delta y = y_j - y_i \qquad \text{(A2)}$$

$$\Delta v_x = v_{xi} - v_{xj} \qquad \text{(A3)}$$

$$\Delta v_y = v_{yi} - v_{yj} \qquad \text{(A4)}$$

$$R = \sqrt{(\Delta x)^2 + (\Delta y)^2} \qquad \text{(A5)}$$

$$\vec{v}_{ij} = \Delta v_x \vec{i} + \Delta v_y \vec{j} \qquad \text{(A6)}$$

The unit normal vector that points from the center of particle i to the center of particle j is given by:

$$\vec{k}_{ij} = \frac{\Delta x}{R}\vec{i} + \frac{\Delta y}{R}\vec{j} \qquad \text{(A7)}$$

Cohesive interactions are implemented when the particle separation distance is twice the width of the square well ($R = 2r_{outer}$) and all inelastic collisions are implemented when particles are in physical contact ($R = 2r_{inner}$). Because the relative position of the particles changes as they move between these two states, the unit normal vector also changes ($\vec{k}_{ij} = \vec{k}_{ij,1}$ at approaching cohesive interactions, $\vec{k}_{ij} = \vec{k}_{ij,2}$ at inelastic

collisions, $\vec{k}_{ij} = \vec{k}_{ij,3}$ at departing cohesive interactions). If, however, the distance between the outer radius and inner radius is considered small ($r_{outer} \sim r_{inner}$) then the relative position is essentially unchanged throughout the entire sequence ($\vec{k}_{ij,1} = \vec{k}_{ij,2} = \vec{k}_{ij,3}$). Once this simplification is made, it is possible to combine the expressions for all three types of interactions (equations 3.3, 3.6 and 3.8) and derive an expression for the effective coefficient of restitution over the entire collision sequence.

First, consider the change in the normal, relative velocity that occurs during an escaping-cohesive interaction (equation 3.8):

$$\vec{k}_{ij,3} \cdot \vec{v}_{ij,d} = -\sqrt{\left(\vec{k}_{ij,3} \cdot \vec{v}_{ij,c}\right)^2 - \frac{4D}{m}} \qquad \text{(A8)}$$

Because the normal, relative velocity is unchanged during the interaction sequence, equation A8 can be combined with equation 3.3 to obtain the relative velocity after escape in terms of the relative velocity before the inelastic collision:

$$\vec{k}_{ij,3} \cdot \vec{v}_{ij,d} = -\sqrt{\left(-e\vec{k}_{ij,2} \cdot \vec{v}_{ij,b}\right)^2 - \frac{4D}{m}} \qquad \text{(A9)}$$

Equation 3.6 is then be combined with equation A9 to give the relative normal velocity after escape in terms of the relative velocity before the approaching-cohesive interaction:

$$\vec{k}_{ij,3} \cdot \vec{v}_{ij,d} = -\sqrt{\left(-e\sqrt{\frac{4D}{m} + \left(\vec{k}_{ij,1} \cdot \vec{v}_{ij,a}\right)^2}\right)^2 - \frac{4D}{m}} \qquad \text{(A10)}$$

This expression is then rearranged into the equivalent expression:

$$\vec{k}_{ij,3} \cdot \vec{v}_{ij,d} = -\sqrt{e^2\left(\frac{4D}{m} + \left(\vec{k}_{ij,1} \cdot \vec{v}_{ij,a}\right)^2\right) - \frac{4D}{m}} \quad \text{(A11)}$$

$$\vec{k}_{ij,3} \cdot \vec{v}_{ij,d} = -\sqrt{e^2\left(\vec{k}_{ij,1} \cdot \vec{v}_{ij,a}\right)^2 + \frac{4D}{m}\left(e^2 - 1\right)} \quad \text{(A12)}$$

$$\vec{k}_{ij,3} \cdot \vec{v}_{ij,d} = -\left(\vec{k}_{ij,1} \cdot \vec{v}_{ij,a}\right)\sqrt{e^2 + \frac{\frac{4D}{m}\left(e^2 - 1\right)}{\left(\vec{k}_{ij,1} \cdot \vec{v}_{ij,a}\right)^2}} \quad \text{(A13)}$$

This yields the final expression for the effective coefficient of restitution:

$$e_{eff,r_{outer}=r_{nneri}} = -\frac{\vec{\boldsymbol{k}}_{ij,3} \cdot \vec{\boldsymbol{v}}_{ij,d}}{\vec{\boldsymbol{k}}_{ij,1} \cdot \vec{\boldsymbol{v}}_{ij,a}} = \sqrt{e^2 + \frac{\frac{4D}{m}\left(e^2 - 1\right)}{\left(\vec{\boldsymbol{k}}_{ij,1} \cdot \vec{\boldsymbol{v}}_{ij,a}\right)^2}} \quad \text{(A14)}$$

$$e_{eff,r_{outer}=r_{inner}} = \sqrt{e^2 + \frac{4\left(e^2 - 1\right)D}{m\left(\vec{k}_{ij,1} \cdot \vec{v}_{ij,a}\right)^2}} \quad \text{(A15)}$$

Appendix B. Equations of Motion for Two-Particle Linear Spring-and-Dashpot Interaction

According to the linear-spring and dashpot contact model, the equation of motion in the normal relative direction between two contacting spheres is given by:

$$\frac{m}{2}\frac{\partial^2\left(\delta_{n,ij}\right)}{\partial t^2}+K_n\delta_{n,ij}+\eta_n\frac{\partial\left(\delta_{n,ij}\right)}{\partial t}=0 \qquad \text{(B1)}$$

where m is the individual particle mass, $\delta_{n,ij}$ is the normal overlap between both particles, t is time, K_n is the normal spring constant and η_n is the normal damping coefficient. This equation is also the equation of motion for a damped harmonic oscillator. Assuming that the normal component of the initial relative velocity (v_o) is known, equation B1 can be solved to yield the following expression for the normal overlap as a function of time:

$$\delta_{n,ij}=\frac{v_o}{q}sin(qt)exp(-\alpha\omega_o t) \qquad \text{(B2)}$$

where the intermediate constants are defined as:

$$\omega_o=\sqrt{2K_n/m} \qquad \text{(B3)}$$

$$\alpha=\frac{\eta_n}{\sqrt{2mK_n}} \qquad \text{(B4)}$$

$$q=\omega_o\sqrt{1-\alpha^2} \qquad \text{(B5)}$$

The relative velocity between the particles is then given by:

$$\frac{\partial\delta_{n,ij}}{\partial t}=\frac{v_o}{q}exp(-\alpha\omega_o t)\{q\,cos(qt)-\alpha\omega_o\,sin(qt)\} \qquad \text{(B6)}$$

The time at maximum overlap can be determined by setting equation B6 equal to zero to find the time at which the relative velocity reverses and the particles begin to rebound (t_m):

$$t_m = \frac{1}{q} tan^{-1}\left(\frac{q}{\alpha\omega_o}\right) \tag{B7}$$

This expression can be used with equation B2 to determine the maximum overlap during a given collision ($\delta_{n,max}$):

$$\delta_{n,max} = \frac{v_o}{q} sin\left[tan^{-1}\left(\frac{q}{\alpha\omega_o}\right)\right] exp\left[\frac{-\alpha\omega_o}{q} tan^{-1}\left(\frac{q}{\alpha\omega_o}\right)\right] \tag{B8}$$

The overall duration (t_c) of the collision can be determined by setting equation B2 equal to zero.

$$t_c = \frac{\pi}{q} \tag{B9}$$

Inserting this expression into equation B6 yields an expression for the normal component of the rebound relative velocity.

$$\left.\frac{\partial\delta_{n,ij}}{\partial t}\right|_{t=t_c} = -v_o\, exp\left(\frac{-\alpha\omega_o\pi}{q}\right) \tag{B10}$$

Because the coefficient of restitution is the negative ratio of the rebound relative normal velocity to the incident relative normal velocity expression for the coefficient of restitution (e) can be extracted from equation B8 as follows:

$$e = exp\left[\frac{-\alpha\omega_o\pi}{q}\right] \tag{B11}$$

Equation B11 can then be expanded into the following form by combining it with equations B3, B4 and B5:

$$e = exp\left[\frac{\eta_n}{m\sqrt{\frac{2K_n}{m} - \frac{\eta^2}{m^2}}}\right] \qquad \text{(B12)}$$

Appendix C. Equations of Motion for Two-Particle Spring-and-Dashpot Interaction with Constant Cohesive Forces

The Hamaker model for van der Waals forces incorporates a cohesive force that increases in magnitude as the separation distance between two interacting particles decreases. In order to account for surface asperities and avoid a singularity at zero separation distance, the cohesive force is kept at a constant value for all separation distances below a critical separation distance. During particle contact, this constant cohesive force continues to be implemented, thereby altering the dynamics of the soft-sphere interaction. Hence, equations derived in Appendix B are not valid for the cohesive case.

The equation of motion in the normal direction between two contacting spheres that include a constant cohesive force is given by:

$$\frac{m}{2}\frac{\partial^2\left(\delta_{n,ij}\right)}{\partial t^2}+K_n\delta_{n,ij}+\eta_n\frac{\partial\left(\delta_{n,ij}\right)}{\partial t}+F_c=0 \qquad \text{(C1)}$$

where m is the mass of the particles, $\delta_{n,ij}$ is the normal overlap between the particles, t is time, K_n is the normal spring constant, η_n is the normal damping coefficient and F_c is a constant attractive force between the two particles. Assuming that the normal component of the initial relative normal velocity (v_o) is known, equation C1 can be solved to yield the following expression for the normal overlap as a function of time:

$$\delta_{n,ij}=B_o\,exp\left(-\alpha\omega_o t\right)sin\left(qt\right)+C_o\,exp\left(-\alpha\omega_o t\right)cos(\,qt\,)-\frac{F_c}{K_n} \qquad \text{(C2)}$$

where the intermediate constants are defined as:

$$\omega_o = \sqrt{2K_n / m} \tag{C3}$$

$$\alpha = \frac{\eta_n}{\sqrt{2mK_n}} \tag{C4}$$

$$q = \omega_o \sqrt{1-\alpha^2} \tag{C5}$$

To solve for the additional constants, B_o and C_o, the following initial conditions are applied:

$$\delta_{n,ij}\Big|_{t=0} = 0 \tag{C6}$$

$$\frac{\partial \delta_{n,ij}}{\partial t}\Bigg|_{t=o} = v_o \tag{C7}$$

Applying these initial conditions, the constants are determined to be:

$$B_o = \frac{v_o - \frac{F_c}{K_n}\alpha\omega_o}{q} \tag{C8}$$

$$C_o = \frac{F_c}{K_n} \tag{C9}$$

The normal relative velocity between the two particles as a function of time is found by taking the first derivative of equation C2:

$$\frac{\partial \delta_{n,ij}}{\partial t} = cos(qt)exp(-\alpha\omega_o t)[B_o q - C_o \alpha\omega_o] + sin(qt)exp(-\alpha\omega_o t)[-B_o \alpha\omega_o - C_o q] \tag{C10}$$

In order to derive an expression for the maximum overlap in an such an interaction, equation C10 would have to be set equal to zero and solved for the elapsed time at maximum overlap. The maximum overlap is then determined by plugging this time into the right hand side of equation C2.

Appendix D. Square Well Model: Derivation of Expression for Head-On Collision

For the square-well potential, during an interaction between the ith and j^{th} particles, the criterion for agglomerate formation is defined in Section 3.1.2 as follows:

$$\left(\vec{k}_{ij,3} \cdot \vec{v}_{ij,c}\right)^2 - \frac{4D}{m} \leq 0 \qquad \text{(D1)}$$

where $\vec{k}_{ij,3}$ normal unit vector pointing from the center of the ith particle to the center of the jth particle at the instance of a departing cohesive interaction; $\vec{v}_{ij,c}$ is the relative velocity between the ith particle and the jth particle after experiencing an inelastic collision; D is the cohesive well depth and m is the particle mass. This equation can be rearranged to obtain an expression for the minimum relative normal *departing* velocity ($\vec{k}_{ij,3} \cdot \vec{v}_{ij,c}$) escape agglomeration:

$$\vec{k}_{ij,3} \cdot \vec{v}_{ij,c} = -\sqrt{\frac{4D}{m}} \qquad \text{(D2)}$$

In this derivation, it is assumed that the particles are undergoing a head-on normal, collision.. This assumption implies that the unit vector connecting particle centers does not change over the entire interaction sequence ($\vec{k}_{ij} = \vec{k}_{ij,1}$ at approaching cohesive interactions, $\vec{k}_{ij} = \vec{k}_{ij,2}$ at inelastic collisions, $\vec{k}_{ij} = \vec{k}_{ij,3}$ at departing cohesive interactions).

$$\vec{k}_{ij,1} = \vec{k}_{ij,2} = \vec{k}_{ij,3} \qquad \text{(D3)}$$

The pre-collisional (inelastic collision) velocity ($\vec{k}_{ij,2} \cdot \vec{v}_{ij,b}$) is given in terms of the coefficient of restitution:

$$\vec{k}_{ij,2} \cdot \vec{v}_{ij,c} = -e\left(\vec{k}_{ij,2} \cdot \vec{v}_{ij,b}\right) \qquad \text{(D4)} \quad (3.3)$$

with the assumption that the collision is head on

$$\vec{k}_{ij,3} = \vec{k}_{ij,2} \qquad \text{(D5)}$$

equations D2 and D4 can be combined to develop an expression for the cutoff pre-collisional relative velocity

$$\vec{k}_{ij,2} \cdot \vec{v}_{ij,b} = \frac{1}{e}\sqrt{\frac{4D}{m}} \qquad \text{(D6)}$$

From Chapter 3, the energy balance over the initial approaching cohesive interaction is given as follows:

$$\vec{k}_{ij,1} \cdot \vec{v}_{ij,b} = \sqrt{\frac{4D}{m} + \left(\vec{k}_{ij,1} \cdot \vec{v}_{ij,a}\right)^2} \qquad \text{(D7)} \quad (3.6)$$

Again invoking the assumption of a head-on collision, the following simplification can be made:

$$\vec{k}_{ij,2} = \vec{k}_{ij,1} \qquad \text{(D8)}$$

With this simplification, equations D6 and D7 can be combined to obtain the minimum approaching relative velocity needed for escape:

$$\vec{k}_{ij,1} \cdot \vec{v}_{ij,a} = \frac{1}{e^2}\frac{4D}{m} - \frac{4D}{m} \qquad \text{(D9)}$$

The result is an expression for the minimum approaching relative velocity needed to achieve the minimum escaping velocity (assuming a normal collision):

$$v_{ij,esc} = \sqrt{\frac{4D}{m}\left(\frac{1}{e^2} - 1\right)} \qquad \text{(D10)}$$

This expression can then be rearranged to provide the well depth required to achieve the desired escape velocity for a given coefficient of restitution.

$$D = \frac{m\left(v_{ij,esc}\right)^2}{4\left(\frac{1}{e^2} - 1\right)} \tag{D11}$$

APPENDIX E. Sensitivity Analysis of Fluidized Bed Simulation Parameters

This appendix presents a sensitivity analysis to many of the relevant parameters in the Eulerian-Lagrangian fluidized bed simulation. The default parameter set for all of these simulations is presented in Figure 6.2, however each plot presents data with one of these parameters changed slightly. All plots present data from a fluidization cycle in which the superficial gas velocity was increased linearly from 0 to 65.0 cm/s over a 0.5 second interval. The gas velocity was then increased from 65.0 cm/s to 87.87 cm/s in 20 equally-spaced increments that each lasted 0.5 seconds leading to an overall simulation time of 10.5 seconds.

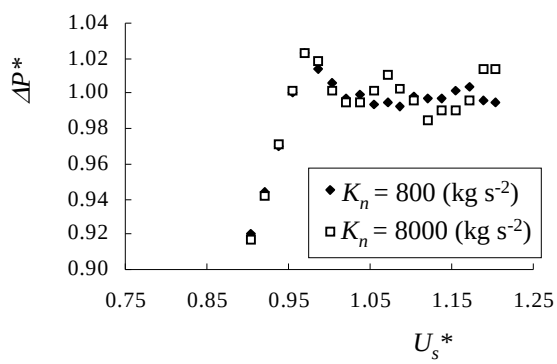

Fig. E-1. *Sensitivity of normalized fluidization curve to normal spring constant (K_n).*

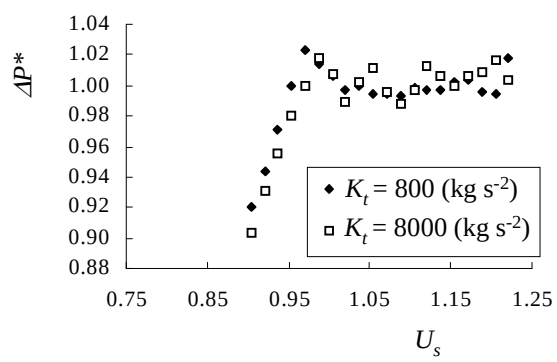

Fig. E-2. *Sensitivity of normalized fluidization curve to tangential spring constant (K_t).*

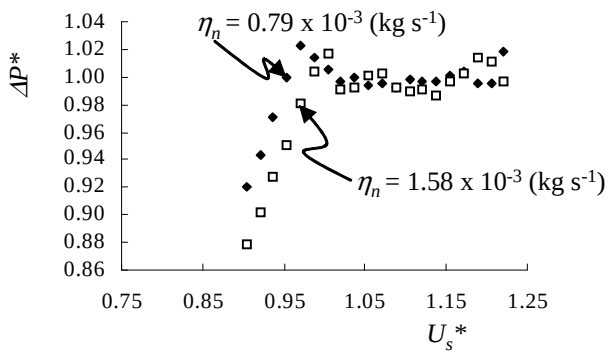

Fig. E-3. *Sensitivity of normalized fluidization curve to normal damping coefficient (η_n).*

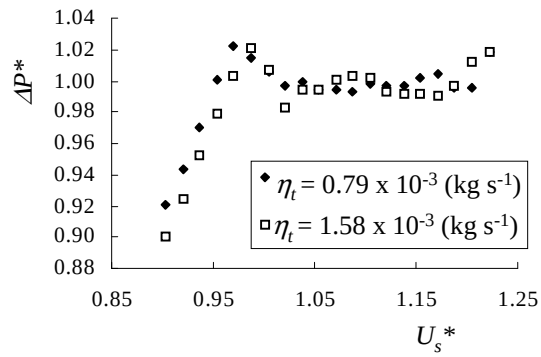

Fig. E-4. *Sensitivity of normalized fluidization curve to tangential damping coefficient (η_t).*

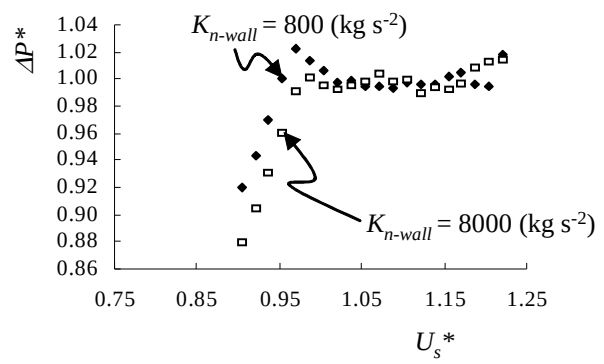

Fig. E-5. *Sensitivity of normalized fluidization curve to wall normal spring constant ($K_{n\text{-}wall}$).*

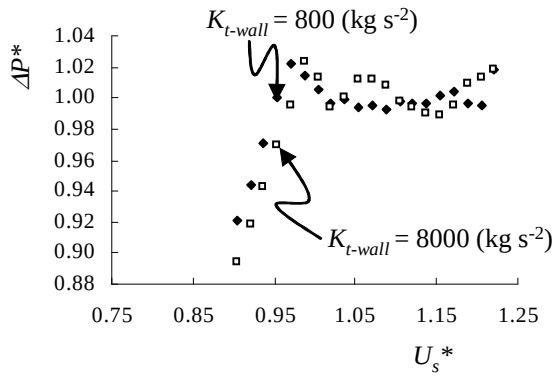

Fig. E-6. *Sensitivity of normalized fluidization curve to wall tangential spring constant ($K_{t\text{-}wall}$).*

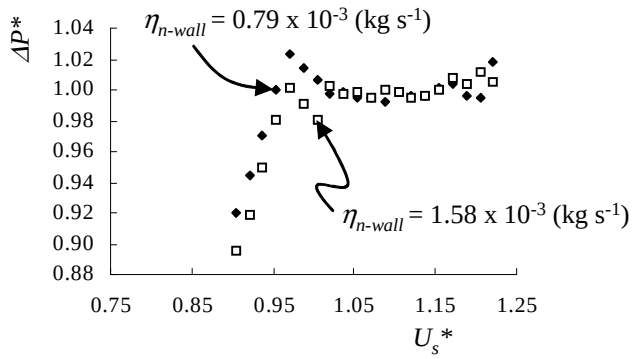

Fig. E-7. *Sensitivity of normalized fluidization curve to wall normal damping coefficient ($\eta_{n\text{-}wall}$).*

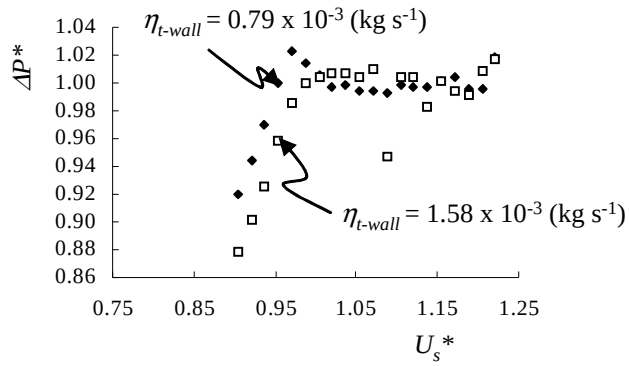

Fig. E-8. *Sensitivity of normalized fluidization curve to wall tangential damping coefficient ($\eta_{t\text{-}wall}$).*

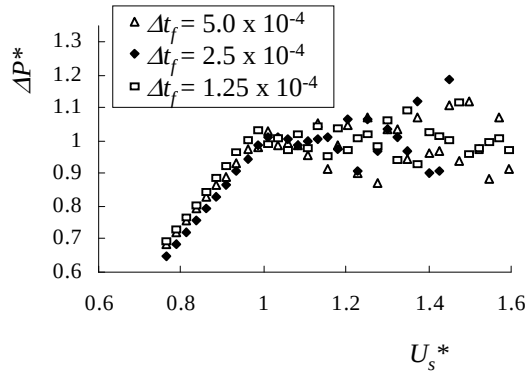

Fig. E-9. *Sensitivity of normalized fluidization curve to fluid time step (Δt_f).*

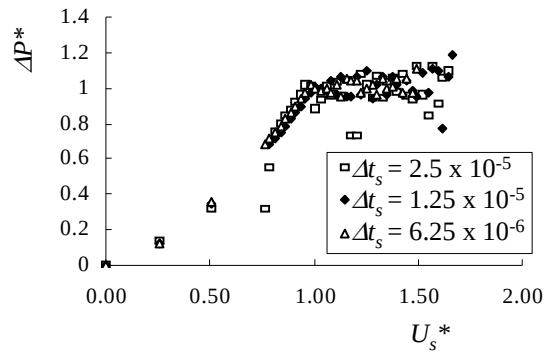

Fig. E-10. *Sensitivity of normalized fluidization curve to solid-phase time step (Δt_s).*

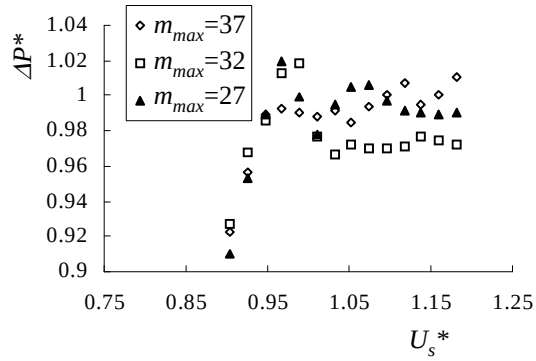

Fig. E-11. *Sensitivity of normalized fluidization curve to number of computational cells in x-direction (m_{max}).*

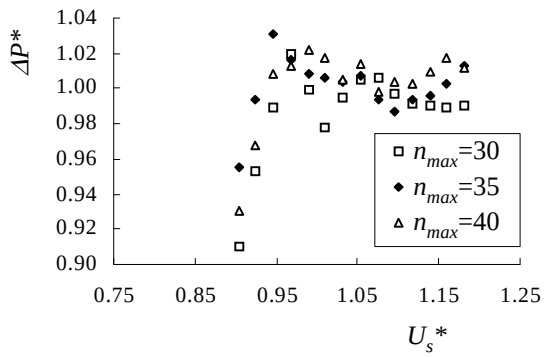

Fig. E-12. *Sensitivity of normalized fluidization curve to number of computational cells in y-direction (n_{max}).*

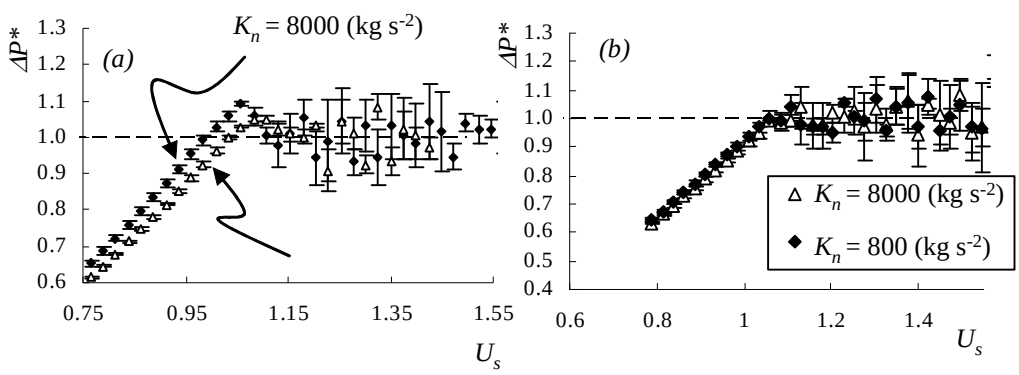

Fig. E-13. *Sensitivity of normalized (a) fluidization curve and (b) defluidization curve to the normal spring constant, using square-well model ($D=5x10^{-4}$).*

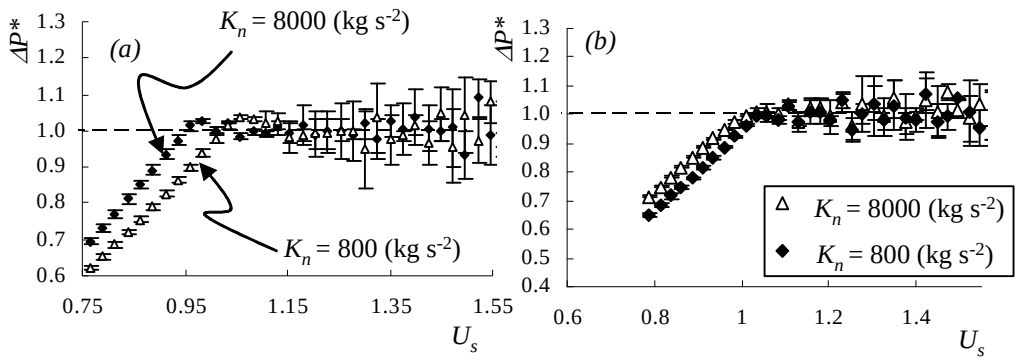

Fig. E-14. *Sensitivity of normalized (a) fluidization curve and (b) defluidization curve to the normal spring constant, using Hamaker model (A=7.49x10^{-12}).*